# Neutral Dynamics in a Helicon Plasma

by

Jonathan Green

A dissertation submitted in partial fulfillment of

the requirements for the degree of

Doctor of Philosophy

(Nuclear Engineering and Engineering Physics)

at the

University of Wisconsin–Madison

2019

Date of final oral examination: May 8, 2019

The dissertation is approved by the following members of the Final Oral Committee:

Oliver Schmitz, Professor, Engineering Physics
Chris C. Hegna, Professor, Engineering Physics
Carl R. Sovinec, Professor, Engineering Physics
Amy E. Wendt, Professor, Electrical Engineering
Cary B. Forest, Professor, Physics

# ABSTRACT

Helicon plasmas are high density, low temperature plasmas with applications in particle accelerators [1], space thrusters [2], and current drive in tokamaks [3]. While efficient ion production is often the chief interest in helicon plasmas, no theory explaining the mechanism behind the high ionization efficiency has been demonstrated through consistent measurement. Particle balance, power balance, and radio frequency (RF) wave coupling all play a role in determining the ionization rate and source distribution. In this work, significant upgrades and diagnostic improvements on the MARIA helicon device in the 3D Plasma Surface Interaction laboratory are presented. Laser induced fluorescence (LIF) measurements are calibrated against an RF compensated Langmuir probe to produce particle flux measurements at several magnetic field strengths and axial positions. Under the assumption that parallel transport is dominant, one dimensional mass and momentum conservation arguments are used to measure the distribution and magnetic field strength scaling of an ionization source in the range of $8 \times 10^{20}$ $\mathrm{m}^{-3}\mathrm{s}^{-1}$. Axial and radial LIF measurements of neutral argon reveal a region of high recycling near an on axis boundary plate, and a 90% depletion of neutral particles near the helicon antenna. Measurements of radial ion losses and neutral source terms are also measured and presented. By identifying both particle sources and sinks, an understanding of the circular refueling process by recycling neutrals begins to form. Additionally a new collisional radiative model developed in collaboration with Auburn University is presented. Comparisons between solutions to the collisional radiative model and experimental results provided valuable insight into the behavior of atomic population processes occurring in MARIA plasmas. Additionally, the collisional radiative model is used in concert with

line ratio spectroscopy to establish a new passive diagnostic for neutral dominated argon plasmas. Agreement with Langmuir probe electron temperature measurements is currently achievable, but additional work is needed to improve the extraction of electron density.

# ACKNOWLEDGMENTS

This work would not have been possible without the support and collaboration of many people along the way. My advisor Dr. Oliver Schmitz gave me the room and encouragement I needed to investigate the topics I found most interesting and was always available to help me find the path forward when I got stuck. Oliver's extensive knowledge and eagerness to try new things made him a pleasure to learn from both in the lab and in life.

I would like to thank Dr. Greg Severn for introducing me to the topic of laser induced fluorescence and experimental atomic physics. Greg's knowledge and enthusiasm of laser based diagnostics kindled my own passion for spectroscopy. I also owe Greg for helping me recognize my own accomplishments and suggesting I publish them. Dr. Stuart Loch and Dr. Ivan Arnold are a wealth of knowledge on atomic physics, and much of this work simply wouldn't have happened without them. Their generosity in providing their new neutral argon atomic dataset and for teaching me the ways of ADAS and collisional radiative calculations cannot be overstated. The hours spent discussing atomic physics with them has been insightful and enjoyable. I am also grateful to my committee for taking the time to go through this process with me.

I would like to thank my parents for giving me the confidence to approach any problem and work my way through it, no matter how hard it may seem at the time. Their love, support, and encouragement of my curiosity has helped shape my path in life since day one. Of course, none of this would have been nearly as fun without my incredible wife, Madison. Graduate school has had some crazy ups and downs, but she has been a constant source of happiness through it all.

This work was funded by the National Science Foundation under NSF CAREER award PHY-1455210 and by startup funds of the Engineering Physics Department in the College of Engineering at the University of Wisconsin - Madison.

# TABLE OF CONTENTS

Page

# Chapter 1

# Introduction

High density plasmas that operate with high efficiency are an asset to advancing plasma science and technology. One application for high density plasmas in particular is in the development of plasma wakefield particle accelerators. The Advanced Proton Driven Plasma Wakefield Acceleration Experiement (AWAKE) project at the European Organization for Nuclear Research (CERN) is actively developing a helicon plasma to reach densities of $5 \times 10^{20}$ m$^{-3}$ for use as a lepton accelerator [1, 4]. In this application, a high energy proton bunch is introduced to a high density plasma with a bunch length equal to the wavelength of the electron plasma frequency. This configuration establishes resonant oscillations of the bulk plasma electrons and leads to the popular blow-out regime for acceleration of electrons in a plasma [5, 6, 7]. To achieve acceptable performance against defocusing, the density variation along the beam path must be less than 0.2%. Unfortunately helicon plasmas are known to have density variations much greater than this [8, 9, 10]. However, despite significant work on the equilibrium [11] and ionization dynamics [12], a complete understanding of density evolution mechanics in helicon plasmas remains elusive.

Versatile and efficient plasma sources are also needed to understand the effect plasmas have on the materials they are exposed to in the exploration of fusion energy as a viable grid level power source. For large fusion experiments like tokamaks and stellerators, the divertor or limiter plasmas typically have high electron densities in the range of $1 \times 10^{19}$ - $1 \times 10^{20}$ m$^{-3}$ and electron

temperatures below 100 eV [13, 14]. Plasma material interaction studies on current fusion grade research devices is often limited due to their short pulse lengths, generally less than 10 seconds, or due to difficult diagnostic access. Cost effective laboratory scale plasma devices that can generate such high density low temperature plasmas for hours at a time, thus simulating the conditions of an operating power plant, are essential. With the ability to generate steady state plasmas with densities in the $1 \times 10^{19}$ - $1 \times 10^{20}$ $m^{-3}$ and electron temperatures of 1-5 eV, helicon plasmas are ideally suited for this role. Indeed, even at 700 W of RF power and magnetic field strengths in the range of 700 G, sputtering of pure molybdenum has been observed during this work, and Oak Ridge National Laboratory is utilizing a 200 kW helicon plasma source in their new Material Plasma Exposure Experiment (MPEX) [15]. To better match ion and electron temperatures to divertor relevant regimes the current prototype for MPEX, Proto-MPEX, utilizes ion and electron cyclotron heating [16].

A key piece of information that has so far eluded researchers is a detailed understanding of the particle balance, the sources and sinks of plasma species and their resulting flows, and its impact for efficiently reaching high densities and ionization rates. Finally understanding this mechanism will allow helicon plasmas, and perhaps other plasma sources, to be optimized for research on topics such as plasma wakefield acceleration and plasma material interaction. Investigating such high density low temperature plasmas requires a set of flexible diagnostics need to be developed and optimized for the task.

The topic of plasma diagnostics is rich in the variety of techniques available to measure the parameters of interest. The most commonly measured parameters are the average electron temperature and the electron density. Both quantities can in principle be measured by Langmuir probes but the theory underlying current collection in such probes, especially in high density RF plasmas, is not straight forward [17, 18]. To overcome the shortcomings of probe based measurement,

techniques such as laser scattering off electrons (Thompson scattering), interferometers, and reflectometers have been developed to measure electron temperature and density with greater accuracy. Thompson scattering has the unique ability to measure the electron energy distribution function (EEDF) directly, while interferometers and reflectometers are limited to measuring only the electron density. Unfortunately the improved accuracy of these more advanced techniques comes with significantly increased complexity and monetary cost.

Another technique for diagnosing a plasma that is gaining in popularity compares the measured emission spectrum of the plasma with a synthetic spectrum from a collisional radiative model (CRM) [19, 20, 21, 22, 23]. Similar methods have been used for decades in astrophysics to ascertain the chemical makeup of far away nebulas and stars [24]. The field of spectral analysis is generally split into three categories depending on the rate of collisions between electrons and atoms. At very low densities where electron collisions are infrequent and collisional deexcitation and recombination is negligible, the coronal model balances the atomic excitation process with spontaneous emission. At very high densities, collisions between atoms drive the system into a state of thermal equilibrium and every atomic process is exactly balanced by its inverse process. Somewhere in between, collisions are frequent enough that a wide variety of atomic transitions occur with differing but roughly equal rates. This in-between region is called the collisional-radiative regime, and has been applied with greater accuracy as the quality of atomic models underlying the CRM increases. The real benefit is that if sufficiently accurate data is available, a complete model of the atomic processes occurring in a plasma can be assembled. A popular way of applying such a technique is to compare ratios of plasma emission lines with theoretical line ratios from numerical models. Utilizing line ratios has the benefit of less complicated calibration of the measurement optics, and often a line-ratio pair can be found that varies as a function of a single parameter like electron temperature or density.

All of the 'advanced' techniques described thus far benefit from being non-invasive, i.e. not artificially disturbing the plasma, and usually very accurate. However, all of them suffer from being line integrated measurements. The parameters being measured are then an average along the line of sight through the plasma. A more active, yet still non-invasive, approach to probing a plasma utilizes a laser beam to pump excitation transitions from lower energy to higher energy atomic states in a plasma. By detecting the photons emitted during the subsequent decay from the higher energy atomic state perpendicular to the axis of the laser beam, the spatial resolution can be increased to the small volume of plasma at the intersection of the pump beam and the observation line of sight [25, 26, 27, 28, 29, 30]. This so-called laser induced fluorescence (LIF) technique combines the advantages of being very accurate and non-perturbing with additional capabilities such as high spatial resolution and the ability to measure atomic flow velocities.

The diagnostic goal of this thesis is to develop and apply these more advanced laser induced fluorescence and line ratio spectroscopy techniques to improve our understanding of helicon plasmas. Specifically the laser induced fluorescence provides a unique ability to accurately measure flow velocities in a plasma as slow as 10 m/s or so. The flow velocity is a key ingredient in assessing the flux of ion and neutral species. The ability to measure these particle fluxes allows the source and sink distribution of ions to be probed directly. These are the primary terms of the particle balance which is set up in a plasma and governs the ultimate density that can be achieved.

A new line ratio spectroscopy diagnostic for diagnosing argon plasmas using a state of the art atomic data set for neutral argon from Dr. Loch's group at Auburn University is described in Chapter 3. This new line ratio spectroscopic tool provides new insights into the relative population of neutral argon metastable states that were not previously accessible. In Chapter 4, a method for applying laser induced fluorescence of argon ions to obtain the ionization source distribution in a helicon plasma, for the first time, is presented. Chapter 5 introduces the Magnetized Anisotropic Ion-distribution Apparatus (MARIA) helicon device and describes the implementation of the line

ratio spectroscopy and laser induced fluorescence diagnostics. The results of the LRS and LIF measurements are be compared with Langmuir probe data and their interpretation with regard to the particle and momentum balance in MARIA is presented in Chapter 6. A summary of the work is presented in Chapter 7 along with possible avenues for future research and conclusions.

# Chapter 2

# Background

## 2.1 Helicon Physics

Helicon plasmas are high density, low temperature plasmas generated by a specific type of electromagnetic wave in a uniform magnetic field. As Dr. Chen says, "Helicon waves are basically bounded whistler waves" [31]. A more rigorous definition is provided below, but for the purposes of this research the uniquely high ionization efficiency and operation at magnetic field strengths in the range of 1000 G are also incorporated into the definition. This serves to distinguish the phenomena of interest in this work, i.e. the density and ionization rate, from other effects such as Trivel-Piece Gould modes and excitation above the electron cyclotron frequency that are collectively included in helicon plasma research. The wave structure is that of a right-hand circularly polarized wave, called an 'R-wave'. The dispersion relation for R-waves propagating at an angle to the background magnetic field is given as

$$\frac{c^2k^2}{\omega^2} = 1 - \frac{\omega_p^2/\omega^2}{1 - \omega_c/\omega\cos\theta}, \tag{2.1}$$

where $c$ is the speed of light in vacuum, $k$ is the wave number, $\omega$ is the frequency, $\omega_p$ is the electron plasma frequency, $\omega_c$ is the electron cyclotron frequency, and $\theta$ is the angle between $\mathbf{k}$ and $\mathbf{B}$.

Davies *et al* showed that for high densities and for $\omega \leq \omega_c$ the plane wave dispersion relation is approached [32]:

$$k = \left(k_\perp^2 + k_\parallel^2\right)^{1/2} = \frac{\omega_p^2\omega}{c^2\omega_c k_\parallel} \tag{2.2}$$

where $k_\parallel = k\cos(\theta)$ is the parallel wavenumber, $k_\perp$ is the perpendicular wavenumber, and $\theta$ is the angle with the applied magnetic field.

Davies continued on to solve for the electric fields using Maxwell's equations and the generalized Ohm's Law in cylindrical geometry, neglecting ion motion, pressure gradients, and resistivity. Davies looked for solutions of the form $f(r)\exp[i(\omega t - kz - m\theta)]$ using the integral representation of Bessel functions. Initially a conducting chamber was assumed, such that the axial and azimuthal electric fields were defined to be zero at the chamber wall, $E_z(a) = E_\theta(a) = 0$, where $a$ is the radius of the chamber. By further neglecting displacement currents and electron inertia, Davies arrived at the dispersion relation for cylindrical geometry

$$0 = kmJ_m(k_\perp a) + k_\parallel k_\perp a J'_m(k_\perp a) \tag{2.3}$$

where $a$ is the chamber radius, $J_m$ is the m'th order bessel function of the first kind, and $J'_m$ is its derivative. If $k_\parallel \ll k$ then Equation 2.3 simplifies to

$$0 = kmJ_m(k_\perp a) \tag{2.4}$$

which yields $k_\perp a = 3.83$ for the first zero of the Bessel function with m=1. Incorporating this result into Equation 2.2 gives:

$$\frac{k_\parallel}{e\mu_0}\left(k_\parallel^2 + \left(\frac{3.83}{a}\right)^2\right)^{.5} = \frac{n_e\omega}{B} \tag{2.5}$$

where $e$ is the electron charge, $\mu_0$ is the vacuum permeability, $n_e$ is the electron density, and $B$ is the magnetic field strength. For a given wave number, frequency, and chamber size this establishes a linear relationship between the background magnetic field and the electron density. Equation 2.5 is plotted for various plasma radii in Figure 2.1. The solid black curves in the figure are the plane wave solutions that exist below the electron cyclotron frequency and above the electron plasma frequency. The label 'helicon' is applied to solutions between the ion and electron cyclotron frequencies. Equation 2.5 essentially establishes the $n/B$ scaling that must be satisfied for the helicon

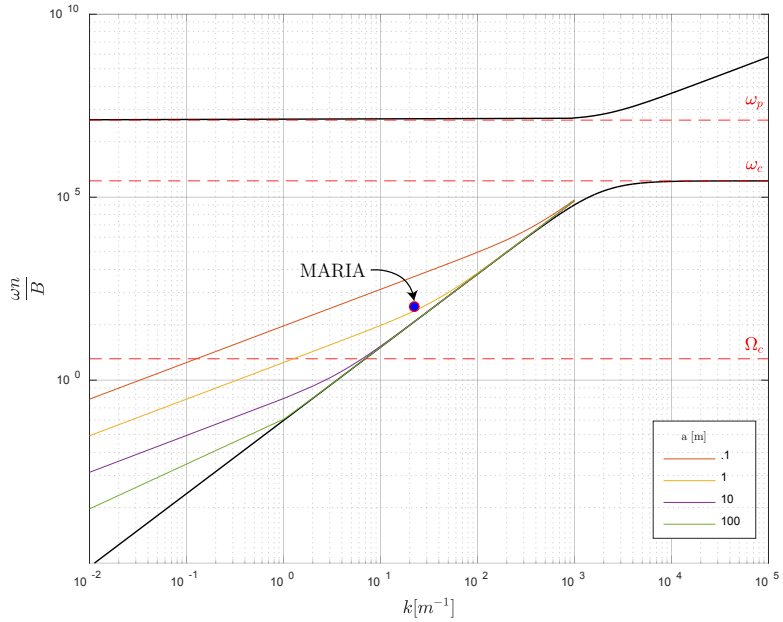


Figure 2.1: The whistler wave exists between the ion cyclotron frequency and the electron cyclotron frequency where the R-wave has a resonance. The R-Wave dispersion relation (for B=.07T,$n = 10^{20}$ m$^{-3}$) is plotted in black. The modified dispersion relation for cylindrical geometry is plotted in color for various plasma radii (a). The operation point of MARIA is shown by the dot.

wave to propagate at fixed wave number, frequency, and chamber radius. It is clear that shorter wavelengths and smaller chambers yield a steeper relationship between density and magnetic field strength. The unique solution for MARIA is indicated in the figure. Even this is a somewhat simplified view as other researchers have indicated that multiple modes can be present in the plasma simultaneously [33]. Specifically Chen has shown that in the case of an insulating chamber with an outer conducting layer a nearly continuous spectrum of wavenumber can propagate [34].

When considering the R-wave dispersion relation, there are actually two possible solutions if one includes the effects of electron mass. One solution corresponds to the so called 'Trivelpiece-Gould' mode while the other corresponds to the helicon mode of interest [32]. The two solutions

are

$$k = \left(k_{\perp}^2 + k_{\parallel}^2\right)^{1/2} = \frac{\omega_p^2 \omega}{c^2 \omega_c k_{\parallel}} \tag{2.6}$$

$$k = \frac{k_{\parallel} \omega_c}{\omega + i\nu} \tag{2.7}$$

where $\nu$ is the electron collision frequency.

Equation 2.6, the helicon mode, is the same as Equation 2.2 and Equation 2.7 is the Trivelpiece-Gould mode. Chen has done extensive research on the Trivelpiece-Gould mode and has shown its wave pattern to be largely dominant at low magnetic field, around 60 G. The mode structure is highly damped and thus deposits its power at the outer radius of the plasma. The helicon mode on the other hand appears to dominate at high magnetic field, above 500 G, with power being deposited on axis. Figure 2.2 shows the radial power deposition profile based on numerical models done by Chen [31]. The low magnetic field dominance of the Trivelpiece-Gould mode is evidenced by the power deposition being distributed at the far outer radius of the plasma for electron densities above $2.5 \times 10^{18}$ m$^{-}3$. The dominance of the Trivelpiece-Gould mode is seen in Figure 2.2 by the steep increase in power deposition at radial positions greater than 40% of the chamber radius at high density. The small increase in power deposition on axis for low density plasmas is due to coupling to the helicon mode. In measuring the axial component of the current density, Blackwell *et al* found that a transition occurs at higher magnetic field strengths and the helicon mode becomes dominant [35]. Numerical work done by a team at Oak Ridge National Laboratory suggests both modes may contribute equally to the power coupling [9]. While the mode structure in terms of magnetic field strengths and current densities have been measured to determine which modes are present, only one set of experimental power absorption measurements has been made by Kramer *et al* [36]. Although strong power absorption was observed on axis, the authors stopped short of claiming the power absorption was solely from the helicon wave.

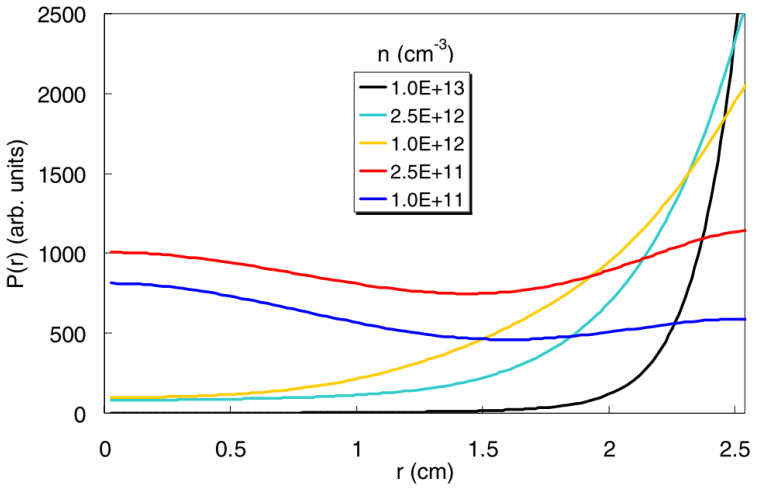


Figure 2.2: Numerical solutions for the power deposition profile for plasmas of various densities and a magnetic field strength of 50G. The figure and calculations were performed by F. F. Chen of UCLA [31]

The linear relationship between $n_e$ and $B$ for the helicon mode is an exciting feature to exploit, but requires a bit of interpretation first. The dispersion relation describes the circumstances under which a specific type of wave will propagate. It does not, by itself, describe any ionization mechanism driven by the wave. It has been empirically found that when the helicon wave propagates in a plasma the electron density increases dramatically. However the exact cause of the increased density, and presumably ionization source rate, is only partially understood. Chen and Hershkowitz have proposed Landau damping is able to accelerate electrons to the phase velocity of the wave which is at the peak of the electron impact ionization cross section [37, 38]. However, further experiments by Blackwell and Chen were unable to detect the presence of a greater population of high energy electrons, thus suggesting that Landau damping is not responsible for the increased ionization source rate [39, 40].

It is tempting to think that one can arbitrarily increase the background magnetic field to produce higher density plasmas, but this viewpoint completely ignores the particle and power balance.

In broad terms, the RF power coupled to the plasma will leave the plasma through heat conduction to the chamber walls or by radiation. Solving a simple zero dimensional (0D) power balance for singly ionized argon based on the work of Lechte *et al* demonstrates the non-linear trade off between electron density and temperature for fixed power input [41]. The solution for typical parameters used in this work, shown in Figure 2.3, shows the decrease in maximum sustainable density with increasing electron temperature due to increased power lost via conduction to the walls. Increasing the RF power input increases the maximum density, but the relationship is not quite linear. The power balance calculation proceeds by equating the total power consumed by radiation, ionization, or conduction to the chamber walls with the input RF power assuming 100% coupling efficiency. The rate coefficients used are identical to those used by Lechte, and are typically total cross sections averaged over a Maxwellian electron energy distribution function. Work done by Goulding *et al* has demonstrated an apparent upper limit to electron density when the electron temperature is very low ( 1.5 eV), in agreement with the simple power balance shown here [42]. The power balance indicates that the vast majority of the power is lost to electron-ion momentum transfer at temperatures below 2 eV or so. Goulding seems to agree with this assessment, concluding that increased heating power is necessary to further heat the electrons and reduce the momentum loss.

The simple power balance shown in Figure 2.3 does not solve the particle balance equations. As a result, electron densities above $2 \times 10^{19}$ m$^{-3}$, the background neutral density, are unrealistic. Investigating how the particle balance influences this limit and trade-off is a fundamental motivation for this research.

## 2.2 Plasma Line Emission

That atoms emit radiation at discreet wavelengths has been known since at least the late 1800's when Johann Balmer came up with his empirical formula for the light emitted from a hydrogen

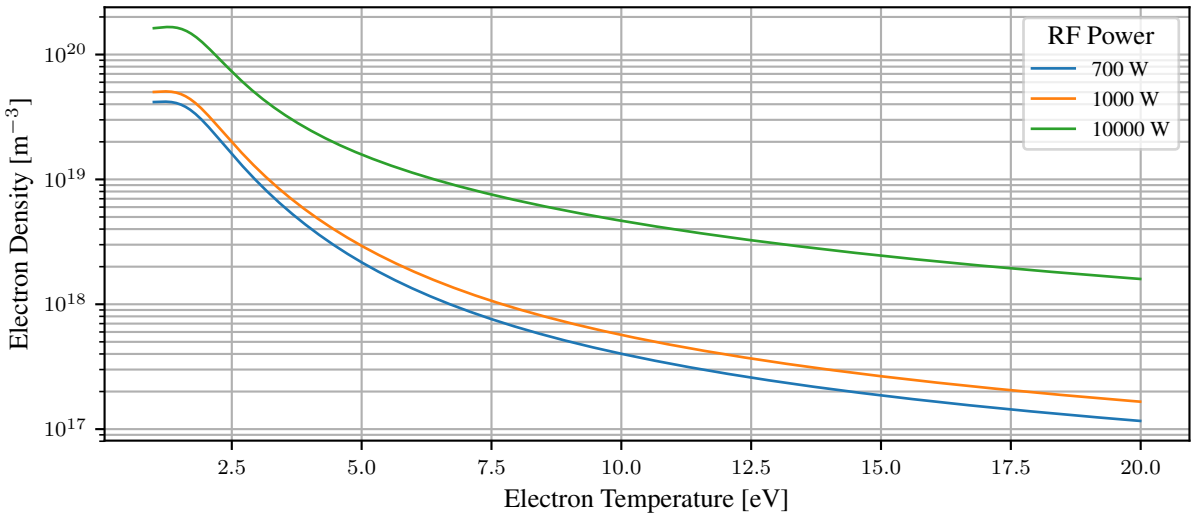


Figure 2.3: 0D power balance calculations performed for MARIA. Neutral density was assumed to be $2 \times 10^{19}$ m$^{-3}$. Calculations were based on work done by Lechte *et al* [41]

atom. The basic physics underlying the appearance of the particular lines Balmer saw were discovered, somewhat collectively, by Bohr, Rutherford, Einstein, in the mid 1910's. It wasn't until quantum mechanics began to be formalized in the mid 1920's by Schrodinger, Heisenberg, and Born that a complete description of the wavelengths at which hydrogen radiates was available.

Today, it is broadly understood that quantum mechanics gives a complete description for the emission and absorption properties of an atom. However, working out the math required from quantum mechanics is difficult and in many cases solutions can only be approximated, as is the case with multiple electron atoms. Due to the mathematical complexity of quantum mechanics, many of the intrinsic properties of atomic states are distilled into easy to use constants such as Einstein's A-coefficient, oscillator strengths, and statistical weights. Coupling this state-specific data with an atom's energy levels and the wavelengths at which it radiates is typically enough for routine spectroscopy. Very little day to day exposure to quantum mechanics is needed!

Fortunately the United States National Institute of Standards and Technology (NIST) hosts an online database of the most current atomic data [43]. From the hosted data, all practical information regarding the line emission measured in this work can be determined.

The wavelength of an emitted photon is related to the energy difference between the two atomic levels involved in the transition by

$$\lambda = \frac{hc}{E_i - E_j}, \tag{2.8}$$

where $h$ is Planck's constant, $c$ is the speed of light in vacuum, and $E_i$ and $E_j$ are the energies of the upper and lower states. The intensity of light emitted at the wavelength $\lambda$ is related to the density of atoms in the upper level by

$$I \propto \frac{dn_i}{dt} \tag{2.9}$$

where $n_i$ is the density of atoms in the upper level.

The astute reader will notice an conflict between equations 2.8 and 2.9. The wavelength is determined from the energy of the two atomic levels, and the intensity is related to the lifetime. If one were to pump a transition from an atomic ground state with a short burst of a perfectly monochromatic light source, the energy of the atom's excited state would be known with zero uncertainty. Heisenberg's uncertainty principle, $\sigma_E \sigma_\tau \geq \hbar/2$, tells us that the uncertainty in the lifetime of the excited atomic state would then be $\infty$.

Actually performing the experiment just described would yield a different result. One would find that the standard deviation of atomic lifetimes is finite. One is then forced to conclude that the energy levels have a finite standard deviation. A rigorous treatment of the atomic transition requires a deep dive into quantum mechanics and quantum electrodynamics. The specific details are not particularly important here and the interested reader is directed to textbooks by Griffiths and Demtroder for a thorough introduction [44, 45].

The result of the quantum treatment, and serendipitously the classical electron oscillator model, is that the energy levels, wavelengths, and lifetime are all intimately related. The radiation intensity for an ensemble of atoms can be shown to have a Lorentzian line shape of the form

$$L(\omega - \omega_0) = \frac{\gamma/2\pi}{(\omega - \omega_0)^2 + (\gamma/2)^2}, \tag{2.10}$$

where $\omega_0$ is the nominal frequency of the emitted photons, $\gamma$ is the full width at half-maximum line width, and $I_0$ is the total intensity of the line. The Lorentzian profile is the result of Fourier decomposing a function of the form

$$f(x,t) = x_0 \exp(-\gamma t)\cos(\omega_0 t). \tag{2.11}$$

Equation 2.11 can be thought of as the probability of finding an atom with its valence electron in an excited state. The oscillatory component, $\cos(\omega_0 t)$, arises from a phenomena called the Rabi flopping frequency, while the decay term, $\exp(-\gamma t)$, arises from the naturally observed trend of decay towards lower energy states.

The $\gamma$ term is thus the same decay rate used in the detailed balance equations of Einstein's 1917 paper, $\gamma = A_{i\to j}$ [46]. Einstein's theory of radiation can then be used to calculate the line intensity for a transition from excited state $i$ to lower state $j$,

$$I_{ij} = h\nu_{ij}\frac{dn_i}{dt} = h\nu_{ij}A_{ij}n_i, \tag{2.12}$$

where $\nu_{ij}$ is the frequency of the emitted photon, $n_i$ is the number of atoms in the excited state $i$, and $A_{ij}$ is the characteristic decay rate for the transition from $i$ to $j$.

The Lorentzian emission line shape is rarely observed in experiment. The analysis that leads to it assumes the atom is stationary. For an atom in motion, the frequency of the emitted photon is shifted by the Doppler effect. The observed frequency for an observer looking directly at the atoms emitting photons is

$$\omega_D = \omega_0 + \mathbf{k}\cdot\mathbf{V} \tag{2.13}$$

where $\omega_D$ is the Doppler shifted frequency, $\mathbf{k}$ is the photon wave vector, and $\mathbf{V}$ is the velocity of the atom in the observer's frame of reference. Of course, when observing a finite volume of atoms in thermal equilibrium, the velocity distribution function (VDF) of the observed atoms is Maxwellian,

$$n_i(v_z)\,dv_z = \frac{n_i}{v_{th}\sqrt{\pi}} \exp[-(v_z/v_{th})^2]\,dv_z \tag{2.14}$$

where $v_z$ is the velocity in the direction of observation and $v_{th}$ is the thermal velocity $v_z = (2kT/m_i)^{1/2}$. Inserting equation 2.13 into the Maxwellian distribution gives the density of atoms that will emit as a function of the emitted photon frequency,

$$n_i(\omega)\,d\omega_z = \frac{n_i}{\omega_0 v_{th}\sqrt{\pi}} \exp\left[-\left(\frac{c(\omega-\omega_0)}{\omega_0 v_{th}}\right)^2\right] d\omega. \tag{2.15}$$

In reality, the true profile typically measured is neither strictly the Gaussian form given by equation 2.15, nor the Lorentzian form given by equation 2.10. Every differential volume of atoms described by the Maxwellian VDF emits with the Lorentzian line shape and the combined effect is a slight additional broadening. The combined effect is found through a convolution

$$I(\omega) = I_0 \int n_i \omega' L(\omega-\omega')\,d\omega'. \tag{2.16}$$

This convolved profile is called a Voigt profile. Typical Lorentzian line widths, called the natural line width, are on the order of 10 MHz, while the Doppler broadened line width is on the order of 5 GHz at 1000 K. Profiles can therefore be fit with Gaussian curves and incur only a small error in thermal temperatures determined by line shape fitting.

## 2.3 Laser Induced Fluorescence

Laser induced fluorescence (LIF) is a non-invasive diagnostic tool that can be used to investigate properties of a plasma without the detrimental disturbance introduced for instance by physical probes. LIF is commonly deployed to measure the velocity distribution function of a plasma

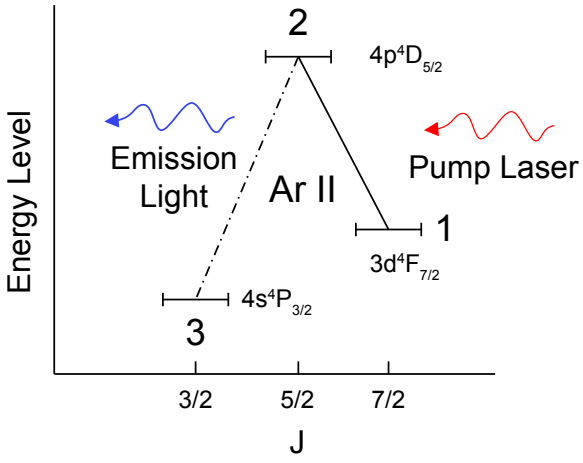


Figure 2.4: Basic LIF scheme.

species [47, 29, 48]. Other more sophisticated techniques can yield direct measurements of the electric field in the vicinity of a plasma boundary [30]. LIF is deployed in this work to measure electron densities, flow velocities, and neutral and ion species temperatures. The LIF development described here was recently published with the journal Measurement Science and Technology and has been included as it forms a foundational role in this research [49]. A brief introduction of the basic idea is provided here, while a deeper dive into the theory is provided in Section 4.

A basic schematic for an argon ion LIF scheme used in this work is shown in Figure 2.4. For this scheme, laser light with a wavelength of 668.614 nm, indicated by the red arrow, will cause atoms to transition from state 1, the 3d $^4$[F] 7/2 level, to state 2, the 4p $^4$[D] 5/2 level. Some of the atoms that are pumped to state 2, will subsequently spontaneously decay to state 3, the 4s $^4$[P] 3/2 level, emitting a photon at 442.6 nm. However, due to the Doppler effect, atoms with some component of velocity either towards or away from the direction of light propagation will, in their frame of reference, observe the light at a slightly different wavelength and thus not undergo the transition. An ensemble of atoms will thus experience an excitation rate according to the inner

product of the light source wavelength and the velocity distribution of the atoms

$$\frac{dn_2}{dt} = n_1 \int\int\int B_{1\to 2} f(x,v) b(v,\nu) \frac{g(x,\nu)}{4\pi} L(\nu)\, d\nu\, d^3v\, d^3x, \tag{2.17}$$

where $n_i$ is the density of the $i$-th excited level, $B$ is the Einstin B-coefficient for absorption, $f$ is the particle velocity distribution function, $g$ is the laser intensity and lineshape, $L$ is the natural line width, and $b$ is the Doppler broadening function.

The intensity of light emitted from the atoms making a transition from state 2 to state 3 is thus given by

$$I \propto A\beta \frac{dn}{dt} = \frac{A\beta}{4\pi} \int\int\int B f(x,v) b(v,\nu) \frac{g(x,\nu)}{4\pi} L(\nu)\, d\nu\, d^3v\, d^3x \tag{2.18}$$

where $A$ is the Einstein A-coefficient for emission and $\beta$ is the branching ratio for the transition from state 2 to state 3 compared to all other possible transitions from state 2. Note that the time integral should be from $t = 0 \to \infty$, but due to the very short time scales, the system is essentially in equilibrium during the observation time scale on the order of microseconds.

Typically the spectral line width of the transition $L(\nu)$ and the laser $g(x,\nu)$ are much much smaller than the line width of the velocity distribution function, (VDF), after accounting for Doppler effects. For example, if one were to imagine $g(x,\nu)$ and $L(\nu)$ to be monochromatic delta functions, then $I$ simply takes the shape of the VDF for the observed volume.

When a magnetic field is present, as in this research, the energy of the states involved in the LIF process are either increased or decreased depending on whether the angular momentum vector is aligned parallel or anti-parallel to the magnetic field. This splitting is the Zeeman effect at low magnetic field strengths shown in Equation 2.19, or the Paschen-Back effect at high field strength.

$$E_Z = \frac{e}{2m} \mathbf{B} \cdot \langle 2\mathbf{S} + \mathbf{L} \rangle = g m_j \mu_B B, \tag{2.19}$$

where $E_z$ is the energy shift due to the Zeeman effect, $\mathbf{B}$ is the magnetic field vector, $\mathbf{S}$ and $\mathbf{L}$ are the spin and angular momentum vectors, $m$ is the electron mass, $g$ is the Lande g-factor, $m_j$ is the magnetic quantum number, $\mu_B$ is the Bohr magneton, and $B$ is the magnetic field strength.

Accounting for the Zeeman effect during the transition from state 1 to state 2 in Figure 2.4 yields a shift in the frequency at which the transition takes place due to a background magnetic field. The dipole selection rules from quantum mechanics allow for a change of $-1 \leq \Delta m_j \leq 1$, where $m_j$ is quantum number associated with the z component of the angular momentum. Transitions resulting in a change of $\Delta m_j = +1$ are labeled $\sigma^+$ transitions, where changes of $\Delta m_j = -1$ are labeled $\sigma^-$ transitions. When one of these $\sigma$ transitions occurs some energy will either be gained or lost due to the interaction of the atom's angular momentum with the external magnetic field. Figure 2.5 depicts the influence of the Zeeman effect on the LIF pumping process in a graphical form. The transition occurring in the absence of a magnetic field is the fundamental transition and is indicated by the blue dashed arrow. $\Delta m_j = +1$ transitions requiring additional energy, thus a higher frequency pump light source, are shown to the right of the blue arrow, and the relative strength of these transitions is indicated by the black lines below the energy level diagram. $\Delta m_j = -1$ transitions requiring less additional energy, thus requiring a lower frequency pump light source, are shown to the left of the blue arrow. The red dashed curves in Figure 2.5b.) indicate the combined appearance of the transition groups in a finite temperature plasma with Doppler broadened absorption profiles. The distance between the two peaks is exactly twice the offset distance of one peak from the fundamental transition frequency; i.e. the peaks are symmetrically displaced from the fundamental. The offset from the fundamental frequency at which the transition will occur can be calculated by

$$\Delta f = [(g_2 - g_1)m_{1,2} \pm g_1]\frac{\mu_B B}{h}. \tag{2.20}$$

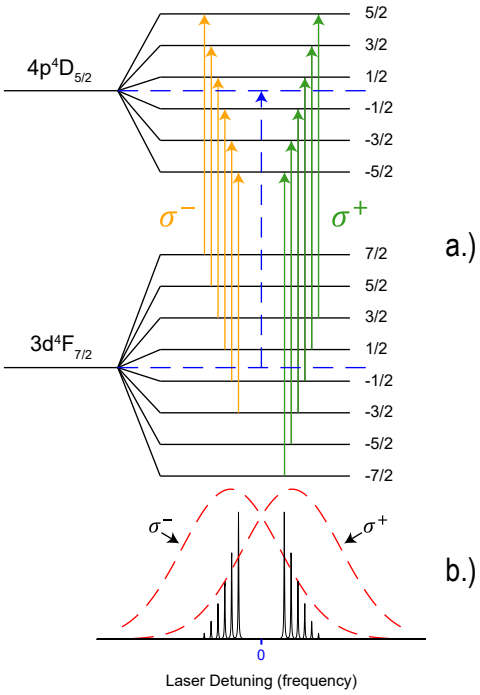


Figure 2.5: The Zeeman effect manifests in a bifurcation in the measured VDF's depending on whether the $\sigma^+$ or $\sigma^-$ transitions are being pumped.

## 2.4 Langmuir Probe Measurements in RF Plasmas

Beyond visual confirmation that a plasma is present in the chamber, Langmuir probes are probably one of the oldest and simplest plasma diagnostics [50, 51]. While the interpretation of Langmuir probe results can often be quite challenging, virtually every plasma experiment has at least one Langmuir probe. Due to their relatively simple construction, electron temperature measurements obtained from a Langmuir probe are often the first publicized result from any new plasma experiment, and are frequently the benchmark against which more complex diagnostics are measured. In this work an RF compensated Langmuir probe constructed specifically for this purpose served as the primary benchmark for other diagnostics, and as a means for comparing MARIA plasmas to devices in other laboratories, and as a basic plasma diagnostic.

A tremendous body of knowledge exists regarding the use and interpretation of Langmuir probe data, and a worthwhile introduction could not be accomplished here. Instead only the specific details that are important to this research is presented.

A particular complication for Langmuir probes is in their use in RF environments. The electron collection current for a single tip Langmuir probe in a quiescent plasma is given by Equation 2.21 [51].

$$I_e(V_B) = An_e e\sqrt{T_e/2\pi m_e}\exp\left[\frac{-e(V_p - V_B)}{Te}\right] \tag{2.21}$$

where $A$ is the probe area, $n_e$ is the electron density, $e$ is the electron charge, $T_e$ is the electron temperature, $m_e$ is the electron mass, $V_p$ is the plasma potential, and $V_B$ is the probe bias potential.

Due to the RF heating mechanism, it is possible for the plasma potential, $V_p$, to oscillate at the RF frequency. Sweeping the bias potential at a rate much slower than the RF excitation frequency yields an I-V curve that is a time-averaged version of the low and high plasma potential I-V curves. This effect is well described for instance by N. Hershkowitz, and the resulting I-V curve is shown in Figure 2.6 [51]. The dotted lines in the figure represent the the $I_e(V_B)$ curve at the high and

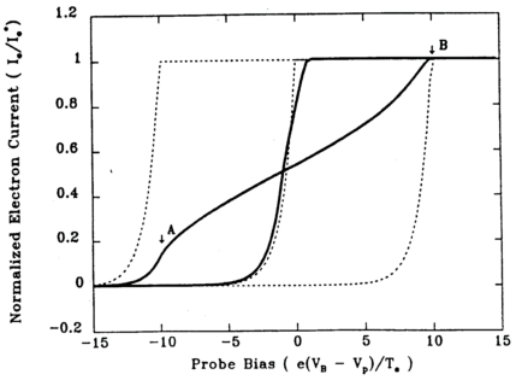


Figure 2.6: The I-V curve measured from a plasma with a sinusoidally oscillating plasma potential [51].

low plasma potential extremes. The solid black curve in the middle is the time averaged result for a fluctuation amplitude of $T_e/e$, and the flatter solid black curve is the time averaged result for a fluctuation amplitude of $10T_e/e$. It is clear that neither of the time averaged traces accurately represent the true $I_e(V_B)$ curve, with the result being severely distorted for high amplitude fluctuations. However, it is important to note that the transition region, between the ion and electron saturation regions, is least distorted at low bias potentials near the ion saturation region, labeled by the 'A'. This suggests that restricting the $I_e(V_B)$ analysis near the ion saturation region will give the most accurate results even when plasma potential fluctuations are possible.

Focusing on the $I_e(V_B)$ curve below the floating potential requires using an accurate model for the ion collection current. The theory of ion collection by a Langmuir probe has been the focus of a tremendous amount of research, and a definitive all-purpose model is still missing. The presence of magnetic fields, ions possibly orbiting the probe tip, and varying ion fractions make selecting the right theory difficult. Two theories that are used frequently in practice are the Orbital Motion Limited (OML) theory first proposed by Langmuir [50], and the Bernstein, Rabinowitz, and LaFramboise (BRL) [52, 53]. The OML theory is the simplest to use, appropriately accounts for the reduction in ion current caused by ions with finite angular momentum orbiting the probe

tip, but does not address magnetic fields. Additionally the OML theory is only strictly valid for low density plasmas where the sheath is larger than the probe tip. The BRL theory on the other hand is valid only in collisionless plasmas, but has the benefit of handling orbiting and probes oriented at an angle to the magnetic field.

The development and analysis of ion collection current theories has been a topic for many PhD theses, but is not the focus of this one. Fortuitously, Dr. Chen of UCLA has performed extensive benchmarking of the two ion collection theories discussed here [17, 54]. By comparing the densities determined by ion current analysis against a microwave interferometer in moderate density plasmas, Chen found that none of the ion collection theories worked flawlessly. However, Chen recommends an average between the BRL and OML theories as being most accurate when working specifically with helicon discharges.

In this work, the OML theory was found to fit the data most reliably. The BRL fit was found to predict more saturated ion collection current while the OML fit captured the $V^{1/2}$ slope well as shown in Figure 2.7. The BRL theory consistently predicted electron densities a factor of two higher than the OML theory. The predicted electron temperatures were typically comparable. At low densities the BRL theory and OML theory both fit the data reasonably well and predicted similar electron densities. These results are very similar to those described by Chen *et al* in an inductively coupled plasma with similar RF power and density [55]. Of the two ion collection current theories, OML and BRL, Chen found that the OML theory agreed most closely with microwave interferometry measurements. Based on their work and the ability to reliably fit IV curves measured in this work, the OML theory was used throughout this work.

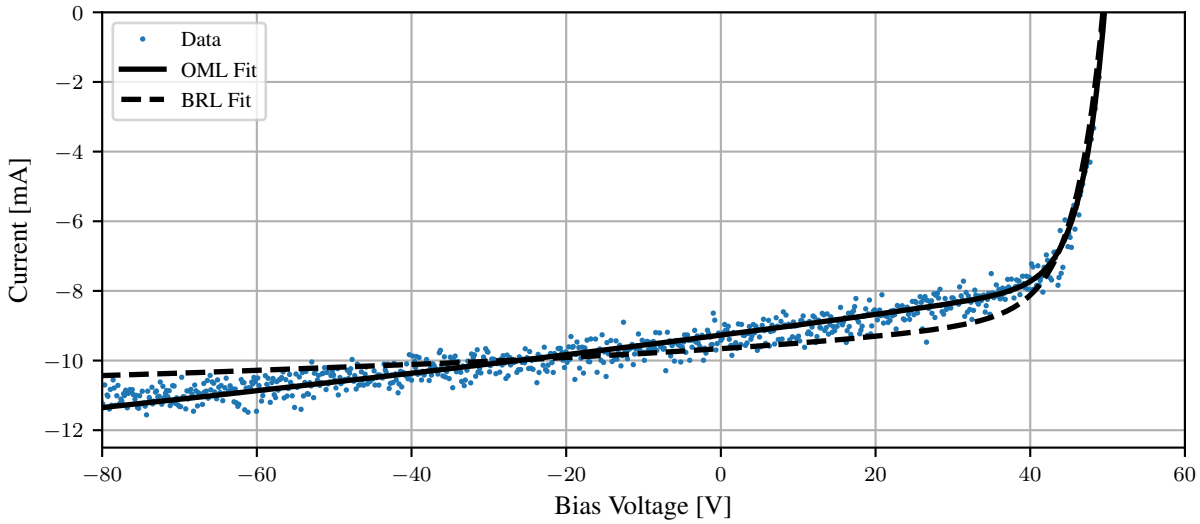


Figure 2.7: The BRL theory predicted an electron temperature of 3.58 eV and an electron density of $7.8 \times 10^{18}$ m$^{-3}$. The OML theory predicted a slightly lower temperature of 2.98 eV and an electron density of $4.4 \times 10^{18}$ m$^{-3}$.

# Chapter 3

# Neutral Argon Line Ratio Spectroscopic Diagnostic

A particularly useful feature of plasmas is that they are full of energetic electrons capable of exciting atoms. A byproduct of this excitation is the light emitted as the atoms relax to a state of lower excitation. This property has been used in astronomy since the mid 1800's to deduce the composition of various gasses [56]. Much more is known today than back in the 1800's and the atomic behavior of plasmas can be investigated in much more detail. Line ratio spectroscopy (LRS) is a technique that can extract bulk plasma properties such as electron temperature and density from pre-tabulated data, while collisional radiative modeling (CRM) enables more detailed information about individual states to be extracted [19, 57, 58].

The usefulness of line ratio spectroscopy can be demonstrated for gasses at elevated temperatures through the use of the Boltzmann equation, which relates the ratio of different excited state densities to temperature,

$$\frac{n_2}{n_1} = \frac{g_2}{g_1} \exp\left(\frac{E_2 - E_1}{kT}\right), \tag{3.1}$$

where $n_{1,2}$ are the number densities of each level, $g_{1,2}$ are the degeneracies of each level, $E_{1,2}$ are the excitation energies, and $T$ is the thermal temperature of the gas. If the spontaneous emission rate is known, the ratio of the line intensities can be calculated by

$$\frac{\varepsilon_{3\to1}}{\varepsilon_{2\to1}} = \frac{A_{3\to1} g_3}{A_{2\to1} g_2} \exp\left(\frac{E_3 - E_2}{kT}\right), \tag{3.2}$$

where $\varepsilon$ is the photon emissivity and $A_{i\to j}$ is the Einstein A-coefficient for the transition from excited state $i$ to $j$.

Notice that if the ratio of line intensities here is measured and the excitation energy of the two states are known, the temperature of the gas can be extracted without requiring any knowledge of particle density. This is obviously a very simple example with many gross assumptions, however the basic principle of relating line intensity ratios to fundamental properties of the medium is established. In practice, much more complicated techniques can be employed requiring more sophisticated models to describe the plasma emission. This work will leverage collisional radiative modeling extensively to calculate the expected emission intensity of neutral argon lines.

## 3.1 Metastable State Populations

Before jumping straight into the details of collisional radiative modeling, the presence of metastable states of neutral argon must be addressed. Table 3.1 shows the energy of the first five energy levels for neutral argon as found in the NIST database. Here $J$ is the total angular momentum quantum number. Since a photon carries one unit of angular momentum, and angular momentum must be conserved in the emission process, the difference between the final state angular momentum $\mathbf{J}_f$ and initial state angular momentum $\mathbf{J}_i$ must be equal to the angular momentum carried away by the photon, $\lambda$, $\mathbf{J}_f = \mathbf{J}_i + \lambda$. However, $J$ is only the magnitude $J = |\mathbf{J}|$, so the direction of $J_f$ can change to allow one unit of angular momentum to be emitted and allowing $J_f - J_i = 0$. However, a $J = 0$ to $J = 0$ transition has no angular momentum to liberate and this transition type is also forbidden. As a consequence, the levels with $J = 0$ and $J = 2$ are forbidden from decaying to the ground state by electric dipole emission by the dipole selection rules $\Delta J = 0, \pm 1$ and no $J = 0 \rightarrow J = 0$ transitions. These levels are therefore classified as 'metastable'.

Due to their inability to decay to the ground state, a significant population can build up in these levels. Additionally, where spontaneous emission typically keeps the relaxation time for ordinary levels very short, the metastable state relaxation time can extend into the millisecond range. On

Table 3.1: Neutral argon has three metastable levels if the ground state is included [43].

| **Configuration** | **Term** | **J** | **Level Energy ($cm^{-1}$)** |
|---|---|---|---|
| $3s^2 3p^6$ | $^1S$ | 0 | 0.0000 |
| $3s^2 3p^5(^2P^\circ_{3/2})4s$ | $^2[3/2]^\circ$ | 2 | 93,143.760 |
| | | 1 | 93,750.5978 |
| $3s^2 3p^5(^2P^\circ_{1/2})4s$ | $^2[1/2]^\circ$ | 0 | 94,553.6652 |
| | | 1 | 95,399.8276 |

these time scales convection and diffusion can contribute significantly to the transport of atoms through an observation volume. The task of calculating the population of metastable states then enters the realm of transport analysis and is no longer appropriate for collisional radiative modeling alone. For this reason the analysis below treats the metastable state densities as required inputs to solve the CRM equations. This framework is called the 'quasi-steady state' assumption in which most, but not all, of the atomic level populations are assumed to relax to their steady-state value on time scales much shorter than the observation time.

Due to the 11.5 eV energy difference between the ground and lowest energy metastable state, the excitation rate coefficient from one of the metastable states is roughly $10^5$ times greater than out of the ground state. At the same time however, the density of atoms in the ground state can easily be $\sim 10^5$ greater than the metastable state, making the actual excitation rate out of the ground and metastable states comparable. For this reason it is very important to know the ratio of the metastable state densities to the ground state density if an accurate model of the plasma emission is desired.

## 3.2 Collisional Radiative Modeling

Collisional radiative modeling is a highly detailed approach that can be used to extract almost any desirable quantity about a plasma's state of atomic excitation. The basic principle is to collect spectroscopic information regarding the collisional excitation/relaxation rates to and from as many excited atomic states as possible and incorporate them into a system of coupled differential equations that describe all the processes acting on the atoms. The system of equations is then solved, yielding the density of each exited state for the given plasma conditions. The process of solving the differential equations is straightforward. The complexity and detail involved in using collisional radiative models comes from gathering the transition rate information, i.e. the atomic data describing the rates for each atomic process considered, and interpreting the results.

The codes typically used to solve the collisional radiative model in this work are part of the suite of codes known as the Atomic Data and Analysis Structure (ADAS) [59]. ADAS was developed to address the need for centralized modeling and storage of high quality atomic data for fusion plasmas at the Joint European Torus (JET). It is largely a generalized set of codes built around CRM that can look up and use atomic data for any atom as inputs and output information about excited state density, line widths etc. Due to the reliance on atomic rate information, ADAS also oversees a large database containing fundamental atomic data as well as codes capable of generating new atomic data from theory.

### 3.2.1 CRM Theory

The following discussion reviews the basics of collisional radiative modeling using ADAS notation as applicable to this research. Much more detailed information can be found elsewhere by the interested reader [59]. For a given ionization stage of an atom the system of equations

describing the state balance is:

$$\begin{bmatrix} \frac{dn_1}{dt} \\ \vdots \\ \frac{dn_n}{dt} \\ \frac{dn_{1+}}{dt} \end{bmatrix} = \begin{bmatrix} C_{11} & \dots & C_{1n} & r_1 n_e \\ \vdots & \ddots & \vdots & \vdots \\ C_{n1} & \dots & C_{nn} & r_n n_e \end{bmatrix} \begin{bmatrix} n_1 \\ \vdots \\ n_n \\ n_1^+ \end{bmatrix} \tag{3.3}$$

where the terms $C_{ij}$ are elements of the collisional radiative matrix, $n_i$ is the density of the $i$-th excited state, $r_i$ is the recombination rate from the next higher ion stage to excited state $i$, $n_1^+$ is the density of the next higher ion stage, and $n_e$ is the electron density. The $C_{ij}$'s are each a sum of transition probabilities such as the Einstein A-coefficient, the electron impact excitation rate coefficient multiplied by the electron density, the electron impact ionization rate coefficient multiplied by electron density, etc. The notations is such that $C_{51}$, for example, is the transition probability for excitation out of energy level 1 into energy level 5.

Generally the plasma is assumed to be in quasi-static equilibrium, meaning individual excited states can relax to their equilibrium value much faster than plasma transport processes can carry the atoms out of an observed volume but the metastable states relax to their equilibrium value at a similar or slower rate than motion through the observation volume by transport processes. Using this assumption, the CRM code does not solve for the metastable densities, and they must be given as an input. The metastable densities can be solved for with plasma transport codes or measured directly.

Reducing Equation 3.3 according to the quasi-static equilibrium, and setting levels 1, 2, and 4 to be metastable for example, gives

$$\begin{bmatrix} \frac{dn_3}{dt} \\ \frac{dn_5}{dt} \\ \vdots \\ \frac{dn_n}{dt} \end{bmatrix} = \begin{bmatrix} C_{33} & C_{35} & \dots & C_{3n} \\ C_{53} & C_{55} & \dots & C_{5n} \\ \vdots & \vdots & \ddots & \vdots \\ C_{n3} & C_{n5} & \dots & C_{nn} \end{bmatrix} \begin{bmatrix} n_3 \\ n_5 \\ \vdots \\ n_n \end{bmatrix} + \begin{bmatrix} C_{31}n_1 + C_{32}n_2 + C_{34}n_4 + r_3 n_e n_1^+ \\ C_{51}n_1 + C_{52}n_2 + C_{54}n_4 + r_5 n_e n_1^+ \\ \vdots \\ C_{n1}n_1 + C_{n2}n_2 + C_{n4}n_4 + r_n n_e n_1^+ \end{bmatrix} \tag{3.4}$$

$$\mathbf{D} = \mathbf{CN} + \mathbf{M} \tag{3.5}$$

The left hand side of Equation 3.4 is then set to zero $\mathbf{D} = 0$ and the ordinary excited states are found by $-\mathbf{C}^{-1}\mathbf{M} = \mathbf{N}$:

$$\begin{bmatrix} n_3 \\ n_5 \\ \vdots \\ n_n \end{bmatrix} = \begin{bmatrix} C_{33} & C_{35} & \dots & C_{3n} \\ C_{53} & C_{55} & \dots & C_{5n} \\ \vdots & \vdots & \ddots & \vdots \\ C_{n3} & C_{n5} & \dots & C_{nn} \end{bmatrix}^{-1} \begin{bmatrix} C_{31}n_1 + C_{32}n_2 + C_{34}n_4 + r_3 n_e n_1^+ \\ C_{51}n_1 + C_{52}n_2 + C_{54}n_4 + r_5 n_e n_1^+ \\ \vdots \\ C_{n1}n_1 + C_{n2}n_2 + C_{n4}n_4 + r_n n_e n_1^+ \end{bmatrix} \tag{3.6}$$

Within the ADAS nomenclature, metastable levels are indexed with Greek letters, like $\sigma_1$, $\sigma_2$, etc., while normal excited levels are indexed with Roman letters, like $1, 2, etc.$. Using index notation, Equation 3.6 can be written as:

$$n_j = \underbrace{-\sum_{i=1}^{O} \left(C^{-1}\right)_{ij} \sum_{\sigma=1}^{M} C_{i\sigma}\, n_\sigma}_{\equiv \sum_{\sigma=1}^{M} F_{j\sigma}^{(\mathrm{exc})} n_e n_\sigma} + \underbrace{\sum_{i=1}^{O} \left(C^{-1}\right)_{ij} r_i\, n_e n_1^+}_{\equiv F_{j1}^{(\mathrm{rec})} n_e n_1^+} + \cdots \tag{3.7}$$

where $(C^{-1})_{ij}$ represent the elements of the inverted reduced collisional radiative matrix, $O$ is the number of ordinary excited levels, and $M$ is the number of metastable levels. Other effects such as charge exchange, ionization, etc. are not shown in Equation 3.7 but could be included. The spontaneous emission resulting from transitions is then:

$$\varepsilon_{j\to k} = A_{j\to k} \left( \sum_{\sigma=1}^{M} F_{j\sigma}^{(\mathrm{exc})} n_e n_\sigma + \sum_{\nu'=1}^{M_{z+1}} F_{j\nu'}^{(\mathrm{rec})} n_e n_{\nu'}^+ + \cdots \right) \tag{3.8}$$

$$\varepsilon_{j\to k} = \sum_{\sigma=1}^{M} PEC_{\sigma,j\to k}^{(\mathrm{exc})} n_e n_\sigma + \sum_{\nu'=1}^{M_{z+1}} PEC_{\nu',j\to k}^{(\mathrm{rec})} + \cdots$$

Within the ADAS notation, the two terms in Equation 3.8 are called photoemissivity coefficients (PECs). The first term is a sum over each of the metastable states of the ionization stage of interest, while the second term sums over the metastable states of the next higher ionization stage. These PECs are the terms that are used later in this work.

By substituting Equation 3.7 back into Equation 3.3, the collisional dielectronic ionization, $S_C D$, and recombination, $\alpha_C D$, coefficients can be identified:

$$S_{CD} = C_{11} - \sum_{j\neq 1}\sum_{i\neq 1} C_{1j} C_{ji}^{-1} C_{i1} \tag{3.9}$$

$$\alpha_{CD} = r_1 - \sum_{j\neq 1}\sum_{i\neq 1} C_{1j} C_{ji}^{-1} r_i \tag{3.10}$$

These collisional dielectronic coefficients give the rate of change of the ground (or metastable) states due to ionization and recombination. The resulting rates of change become:

$$\frac{d}{dt} n_1 = -n_e S_{CD} n_1 + n_e \alpha_{CD} n_+ \tag{3.11}$$

These coefficients can be combined with the PECs to form new derived quantities:

$$S/XB_{\sigma,j\to k} = \sum_{\nu=1}^{M_{z+1}} \frac{S_{CD,\sigma\to\nu}}{PEC^{(\text{exc})}_{\sigma,j\to k}} \tag{3.12}$$

$$\alpha/XB_{\sigma,j\to k} = \sum_{\nu=1}^{M_{z+1}} \frac{\alpha_{CD,\nu\to\sigma}}{PEC^{(\text{rec})}_{\sigma,j\to k}} \tag{3.13}$$

where the sum is over the metastable states of the next higher charge state and the PEC is for a specific transition from excited state $j$ to excited state $k$ originating from a metastable state of the lower charge state. The $S/XB$ coefficient relates the ionization rate to the photon emission rate and the $\alpha/XB$ coefficient relates the recombination rate to the photon emission rate. These two coefficients can be used to recover ionization and recombination rates from line emission measurements alone.

## 3.3 Line Ratio Spectroscopy

To infer information about a plasma using line emission spectra, simulated spectra are generated using the PECs derived in the previous section and compared with experimental observations. A first order observation might be whether a plasma exists or not, by looking for the presence of *any* emitted photons! In practice one is quite aware that a plasma is present, and utilizing absolute intensity requires additional complexity. A clever technique for avoiding the first order 'brightness' scaling, and dealing with higher order effects, uses ratios of line intensities from the same plasma. Doing so avoids the need for complicated absolute calibration and mitigates the associated uncertainty. Line ratio spectroscopy is used in this work to access the information that would normally be lost in the absolute brightness uncertainty.

To understand how collisional radiative modeling can be used with line ratio spectroscopy, consider the line ratio shown in Equation 3.14. Here the discussion relates to neutral argon, which has two metastable states and the ground state for which densities must be specified, so the $\sum_{\sigma=1}^{M}$ will run through $\sigma = 3$. The metastable levels in argon are the ground state, first excited 4s $^2$[3/2] 2 state, and fourth excited 4s $^2$[1/2] 0 state and are notationally indicated as $n_1$, $n_2$, and $n_4$ respectively. So, under the assumption of quasi-static equilibrium, the line ratio is a function of five independent variables: the electron temperature $T_e$, the electron density $n_e$, and the density of the three metastable states $n_{1,2,4}$. However, by multiplying the numerator and denominator by a common factor, e.g. $1/(n_e n_4)$, one variable can be eliminated. The result, given by Equation 3.15, replaces the three invididual metastable state densities, $n_{1,2,4}$, with ratios of metastable state densities $n_1/n_4$ and $n_2/n_4$. It is often the case that metastable state population accounts for greater than 99% of the neutral density. So, if the relative distribution of metastable state densities can be determined, the absolute populations may be recovered using simpler techniques such as local

pressure and temperature measurements.

$$\frac{\varepsilon_{i\to j}}{\varepsilon_{m\to n}} = \frac{A_{i\to j}\left(PEC^{(\mathrm{exc})}_{1,ij}(n_e,Te)n_1 + PEC^{(\mathrm{exc})}_{2,ij}(n_e,Te)n_2 + PEC^{(\mathrm{exc})}_{3,ij}(n_e,Te)n_4\right)n_e}{A_{mn}\left(PEC^{(\mathrm{exc})}_{1,mn}(n_e,Te)n_1 + PEC^{(\mathrm{exc})}_{2,mn}(n_e,Te)n_2 + PEC^{(\mathrm{exc})}_{3,mn}(n_e,Te)n_4\right)n_e} \tag{3.14}$$

$$\frac{\varepsilon_{i\to j}}{\varepsilon_{m\to n}} = \frac{A_{ij}\left(PEC^{(\mathrm{exc})}_{1,ij}(n_e,Te)\frac{n_1}{n_4} + PEC^{(\mathrm{exc})}_{2,ij}(n_e,Te)\frac{n_2}{n_4} + PEC^{(\mathrm{exc})}_{3,ij}(n_e,Te)\right)}{A_{mn}\left(PEC^{(\mathrm{exc})}_{1,mn}(n_e,Te)\frac{n_1}{n_4} + PEC^{(\mathrm{exc})}_{2,mn}(n_e,Te)\frac{n_2}{n_4} + PEC^{(\mathrm{exc})}_{3,mn}(n_e,Te)\right)} \tag{3.15}$$

### 3.3.1 Selection of Atomic Data

There are many possible sources of atomic data suitable for use in collisional radiative modeling. Some cross sections and rate coefficients can be measured directly [60]. In other cases, complex numerical techniques are used to calculate the cross section directly from theory [61]. The underlying atomic data used in this work consists of electron impact excitation and dexcitation rate coefficients from a very new R-matrix calculation with Pseudo-States performed by Ivan Arnold and Stuart Loch at Auburn University. The paper detailing their work has not yet been published at the time this thesis was written but much of the detail can be found in Arnold's thesis [62]. Included in this dataset are the energy levels for each of the excited atomic states of neutral argon and the Einstein A coefficients for each possible transition. The energy levels have already been shifted from those calculated by the R-matrix method to the energies found in NIST's database. The A coefficients were left as is, but correction factors to scale to the NIST A coefficients were used as described in the next section.

### 3.3.2 Identifying Appropriate Lines

To make use of the collisional radiative modeling and line ratio techniques described above, appropriate lines must be selected. The ideal situation would be to find a pair of lines who's ratio is strictly sensitive to a single plasma parameter, like electron temperature or density. Unfortunately this is unrealistic and in practice each line has some dependence on every variable. So, the initial

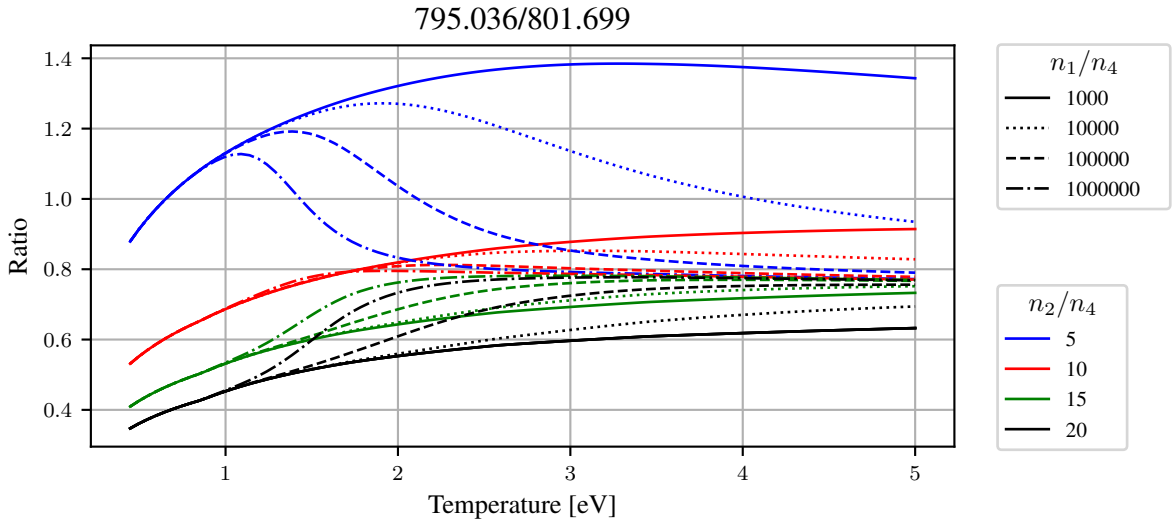


Figure 3.1: Density averaged line ratios the the 795/801 neutral argon lines. The line ratio has been plotted for several values of $n_1/n_4$ and $n_2/n_4$.

search to find appropriate line ratios started out by averaging over some parameter, electron density for example, and staring at ∼2500 possible line ratios that looked something like that shown in Figure 3.1. The figure shows the ratio of the 795 nm and 802 nm lines as a function of electron temperature for different ratios of $\frac{n_1}{n_4}$ and $\frac{n_2}{n_4}$. This 795/802 line ratio appears to be predominantly sensitive to the 4s $^2$[3/2] 2 $\big/$ 4s $^2$[1/2] 0 ($\frac{n_2}{n_4}$) metastable ratio and electron temperature up to about 1.5 eV. Above 1.5 eV the high energy tail of the electron energy distribution function is able to cause sufficient excitation out of the ground state that the ground state to metastable state ratio becomes important; indicated by the divergence of the different line styles. By selecting four similar line ratios and solving for the best fit with a non-linear solver, one might think that the choice of line ratios is arbitrary. In reality, there are a number of reasons to pick certain line candidates and reject others.

One of the main complicating factors is opacity. Imagine a photon emitted from an atom in the center of the plasma decaying to the ground state. As that photon makes its way to the plasma edge

it will encounter many ground state atoms and thus have some probability of being absorbed. A newly excited atom that absorbed the photon can either decay back to the ground state, re-emitting the same photon, or decay to a different level, in which case the initial photon is lost and cannot be detected by the spectrometer. The farther a photon has to travel through a cloud of atoms that can absorb it – the optical depth – the greater the chance of it being absorbed. The end result is that plasmas with appreciable optical thickness at a given wavelength will appear to be emitting less at that wavelength.

Thankfully, there is a relatively simple technique to test for optical thickness. Consider two emission lines originating from the same excited atomic level but decaying to different lower levels. If the ratio of a line for which the plasma is the least optically thick is measured with respect to the one that is most optically thick, the line ratio should increase as the optical thickness increases. Since the light collected by the spectrometer is due to spontaneous emission this line ratio can be initially calibrated by calculating the ratio of branching fractions between the two lines. The branching fraction is defined as

$$\beta = \frac{A_{k\to j}}{\sum_k A_{k\to k}} \tag{3.16}$$

where $A_{i\to j}$ is the Einstein A-coefficient, the transition probability between an upper excited state $i$ and a lower state $j$. The intensity ratio between two lines emitted from the same upper level is then

$$\frac{\beta_{i\to j}}{\beta_{i\to k}} = \frac{A_{i\to j}}{A_{i\to k}}. \tag{3.17}$$

By comparing line intensity ratios in MARIA plasmas with tabulated A-coefficients from the NIST, the opacity of MARIA plasmas can be checked. Dividing ratios of experimental emission lines coming from the same upper level divided by the ratio of NIST A-coefficients for those same transitions, a result of 1 indicates that the emitted light is not affected by excessive absorption due to opacity. Figure 3.2 shows the results for one spectrum from MARIA. The calculated ratio of

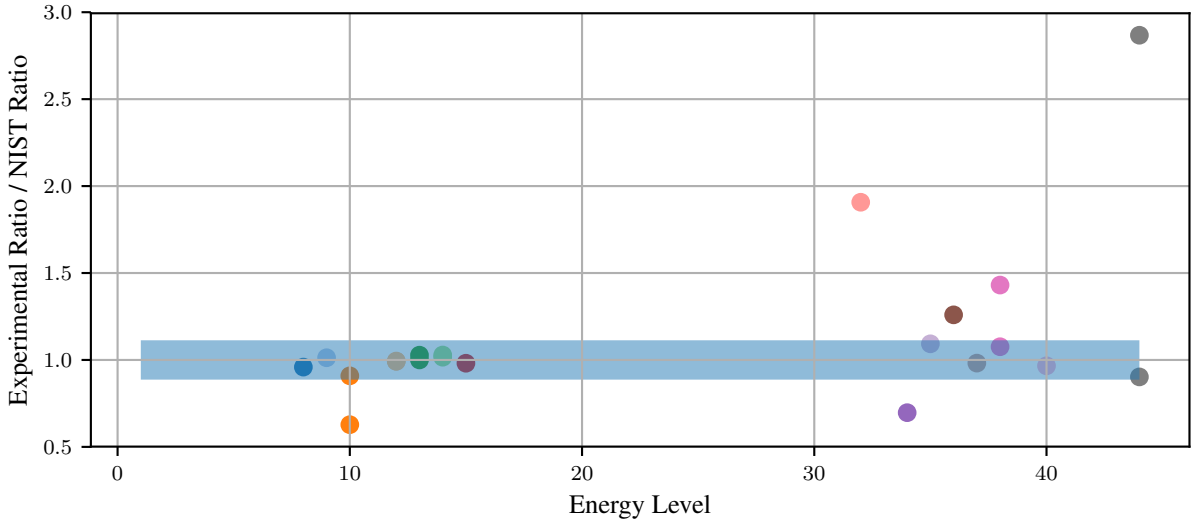


Figure 3.2: A ratio of experimental line ratios to NIST A-coefficient ratios for emission lines originating from the same upper level equaling one indicates the plasma is not optically thick.

ratios are shown by the dots, and the experimental uncertainty in the A values reported by NIST is indicated by the blue bar around 1. Points in the blue bar are thus not affected by opacity to within the error bars listed by NIST. The data in the figure suggest detectable transitions originating from energy levels below 20 are not significantly impacted by opacity effects.

The data contained in Figure 3.2 can also be used to evaluate the calibration quality as well as the possibility of blended lines. In the figure, fewer of the line ratios for levels above 40 are equal to one. This means that either the measured peak in the spectrum is a sum of multiple blended lines, the calibration is worse for in the wavelength region of those lines, or that these lines are very optically thick. By consulting the NIST database of Ar I and Ar II lines, the cause is largely due to blended lines. The emission lines originating at levels above 30 tend to be in the 300-500 nm range and thus overlap with the lower energy lines from Ar II which emit in the 400 nm range.

Figure 3.2 indicates that working with Ar I lines originating from levels below 20 is relatively safe and unlikely to be affected by opacity. However, lines originating from levels above 20 must be handled carefully to avoid blending, calibration, and opacity effects.

### 3.3.3 Sensitivity of Population Densities

Taking ratios of emission lines in optically thin plasmas is the same as taking a ratio of excited state densities. From Equation 3.8, the emission intensity is simply the excited state density multiplied by the Einstein A-coefficient. This fact can be utilized to help identify the atomic levels whose population rates vary the most. By taking spectra at various radii in a MARIA plasma and dividing the observed line intensities by the appropriate Einstein A-coefficient, the relative behavior of the level populations is investigated. The data in Figure 3.3 shows the density of the 15 lowest excited levels of neutral argon, normalized to the population density of the 8th excited level, as a function of plasma radius and magnetic field strength. In the figure, with increasing radius and magnetic field strength (electron density), the population of levels 7 and 10 appear to increase with respect to level 8, while other levels stay relatively constant or decrease a little bit.

The data in Figure 3.3a suggests the population of levels 7, 10, and 13 measured with respect to the population of level 8 have the highest sensitivity to changing plasma conditions. From this data alone, the population of level 7 appears to decrease with increasing density, which is greatest on axis. However, the variation with increasing magnetic field strength, which is correlated with increasing electron density, shown in Figure 3.3b, indicates the opposite trend. From this data alone, it is not clear whether the variation is due to temperature, density, or both.

By considering how the level populations with respect to the population of level 8 vary as a function of temperature, density, ground$/$4s $^2$[1/2] 0 ratio, and 4s $^2$[3/2] 2$/$4s $^2$[1/2] 0 ratio, some intuition about the atomic state of the plasma can be gained from Figure 3.3a directly. For example,

(a)

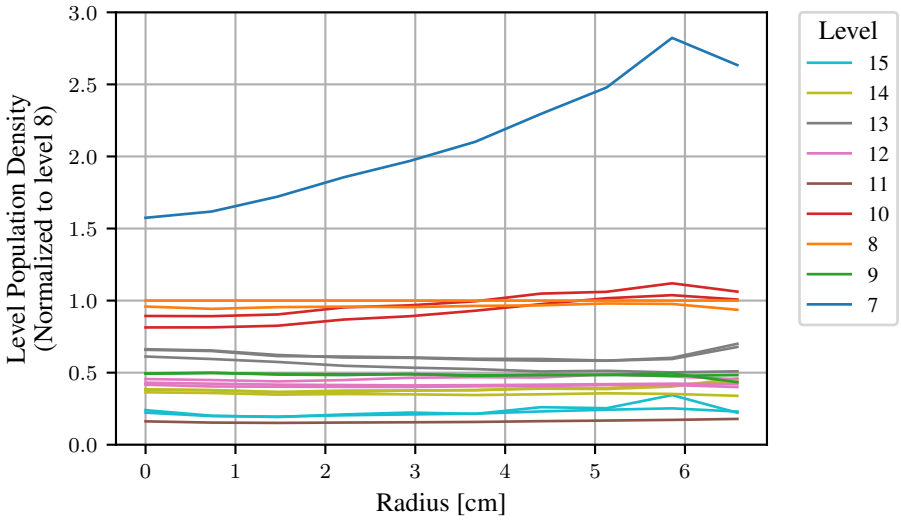


(b)

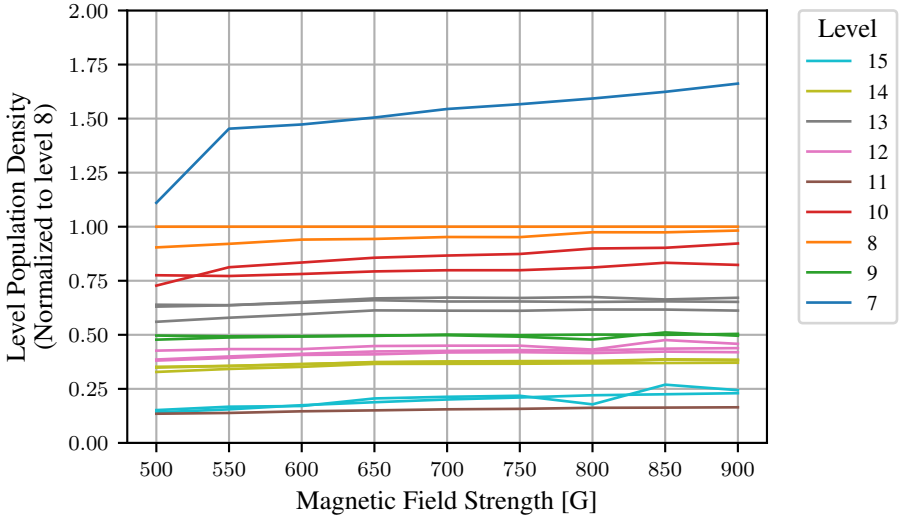


Figure 3.3: Level population densities normalized to the level 8 population density.

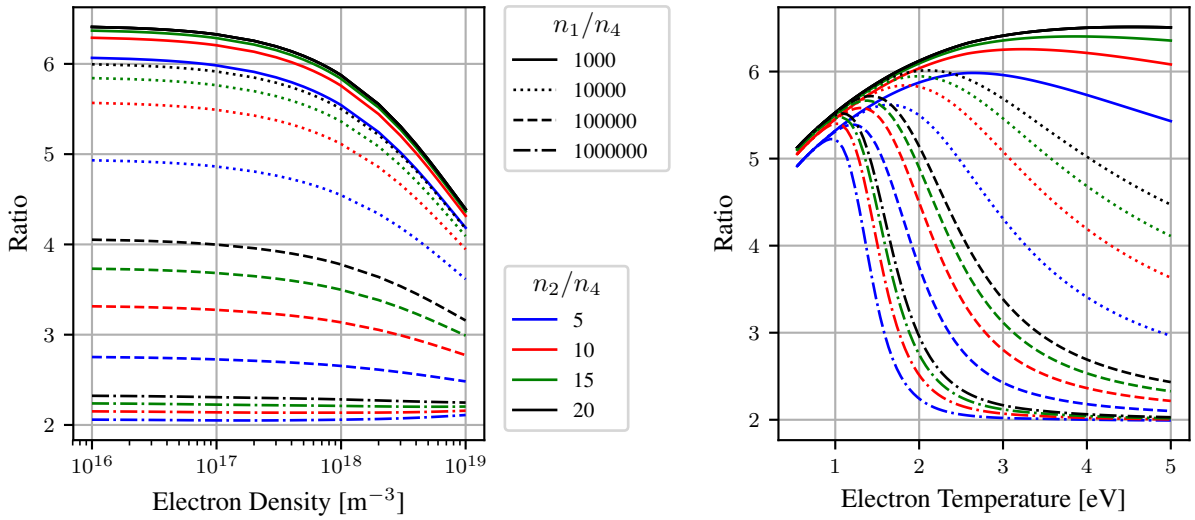


Figure 3.4: Theoretical line ratio plots like these can bring insight to the variations observed in experimental line ratios. The 811 nm / 842 nm line ratio (level 7 / level 8) is plotted here for several densities at 2.5 eV electron temperature (left), and for several temperatures at $2 \times 10^{18}$ m$^{-3}$ electron density (right). $n_1$ is the ground level, $n_2$ is the 4s $^2$[3/2] 2 level, and $n_4$ is the 4s $^2$[1/2] 0 level.

the variation of the 811 nm over 842 nm line ratio, which originate from energy level 7 and 8 respectively, as a function of these parameters is shown in Figure 3.4. From the figure it appears that the population of level 7 increases with respect to level 8 with decreasing ground$/$4s $^2$[1/2] 0 ratios and increasing 4s $^2$[3/2] 2$/$4s $^2$[1/2] 0 ratios. Additionally the dependence on electron density is many times smaller than on the other three parameters. This means inferring electron density will depend on very small changes in emission intensity line ratios that are difficult to separate from statistical fluctuations. However, that there is any dependence on electron density at all gives some hope that the 811 nm / 842 nm line ratio (level 7 / level 8) can be used to extract electron density information.

Due to the low temperatures around 1-4 eV typically encountered in MARIA plasmas, excitation out of the ground state is very difficult and only possible due to excitation by electrons in the high energy tail of the distribution function. As a result increasing the ground$\big/$4s $^2$[1/2] 0 ratio generally has the same effect as increasing electron temperature. The result is an inverse relationship between the ground$\big/$4s $^2$[1/2] 0 population ratio and electron temperature necessary to yield a specific emission line ratio. This can qualitatively be seen in the right panel of Figure 3.4. The 811 nm / 842 nm line ratio is about 5 at 0.5 eV irrespective of ground$\big/$4s $^2$[1/2] 0 ratio. As the electron temperature is increased, the ground$\big/$4s $^2$[1/2] 0 ratio must be lower and lower to maintain a line ratio of 5. This fact will become more important when comparing experimental line ratios to simulated ones in the next section.

### 3.3.4 Emission Line Selection

The ultimate goal is to find lines that are primarily populated by excitation out of only a single metastable state. This is basically impossible. However, by carefully studying the electron impact excitation coefficients produced by Stuart Loch's group at Auburn University, the population mechanism itself can be leveraged to aid the selection process. By considering excitation out of only the ground, 4s $^2$[3/2] 2, and 4s $^2$[1/2] 0 levels into the first first 15 excited levels, the population process becomes clearer. The excitation rate coefficient out of each of these metastable levels, normalized to the range $[0, 1]$, for a 2.5 eV plasma is shown in Figure 3.5. The figure makes it pretty clear that the highest excitation rate out of the ground level is into energy levels 5 and 15 (left blue bars), the highest excitation out of the 4s $^2$[3/2] 2 level is into level 7 (middle orange bar), and the highest excitation out of the 4s $^2$[1/2] 0 level is into level 12 (right green bar). The excitation rate coefficients out of the two excited metastable states are approximately equal at $2.15 \times 10^{-13}$ m$^3$s$^{-1}$, while excitation out of the ground level into level 5 is 5 order of magnitude

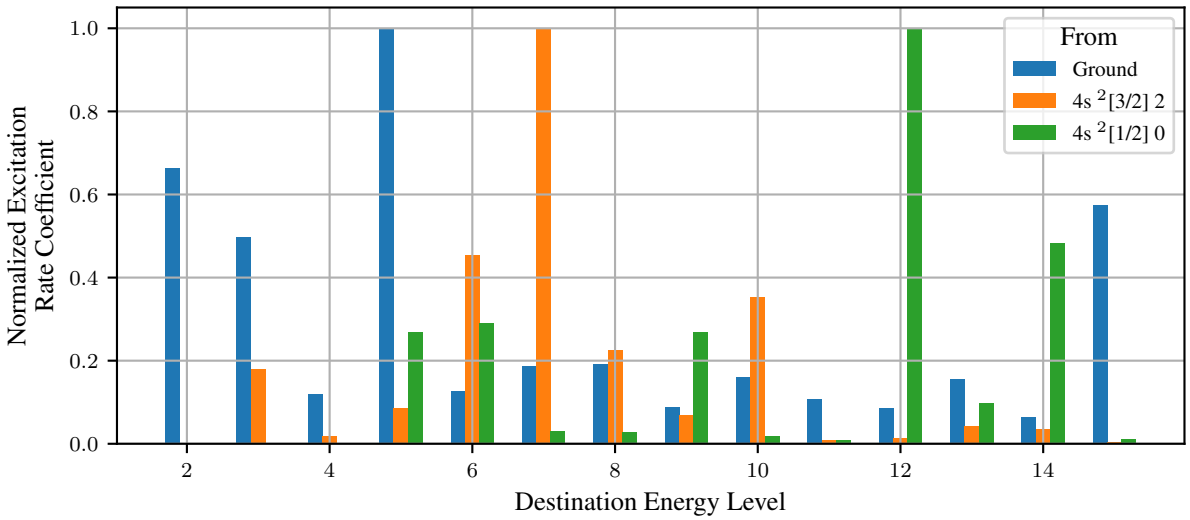


Figure 3.5: Normalized excitation rate coefficients from the ground level and two excited metastable levels into the lowest 15 excited levels of neutral argon.

weaker at $4 \times 10^{-17}$ $m^3s^{-1}$. Since decays from level 5 only emit in the ultraviolet, it cannot be observed with the detection equipment on MARIA which is only sensitive to visible light.

Since the line ratio spectroscopy technique relies on emitted light to infer the population of lower energy levels, a logical approach is to observe light from levels that are most affected by changes in the population distribution of the lower energy levels. This connection is made by the excitation rates. Therefore, photons emitted during decays from level 12 should be sensitive to changes in the population of the 4s $^2$[1/2] 0 level, and similarly photons emitted from levels 7 and 15 should be sensitive to changes in the 4s $^2$[3/2] 2 and ground levels respectively. The three strongest lines coming from levels 7, 12, and 15 are the 811 nm, 852 nm, and 750 nm lines. The 795 nm line, which also comes from level 12, is actually stronger than the 852 nm line, but using that line led to very inconsistent results from the LRS algorithm. In the absence of any opacity effects, as shown to be the case earlier, observing the 750 nm, 852 nm, and 811 nm lines should be the best combination for extracting relative metastable state ratios.

Two more lines are necessary to construct the 4 line ratios necessary to constrain the 4 independent variables. Since the three lines discussed so far mostly relate to the ground and metastable state population densities, looking for lines that are sensitive to electron density, $n_e$, and temperature, $T_e$, would be the most useful. It turns out that the 738/842 line ratio has a moderate dependence on electron density, changing from approximately 0.24 to 0.35 from $1 - 10 \times 10^{18}$ m$^{-3}$. No explicit dependence on electron temperature is included by selecting a specific line or line ratio but all of the lines have some dependence on electron temperature that should be recoverable by solving for all dependent variables simultaneously. The 842 nm line was used as a denominator both because it works well in the case of the 738/842 ratio, but it is also the most equally populated from the ground and metastable states after accounting for the typical relative population densities. These transitions are indicated in the partial Grotrian diagram shown in Figure 3.6.

## 3.4 Line Ratio Spectroscopy Algorithm

The simulated line ratios used for comparison are calculated as shown by Equation 3.18. Experimental line ratios were compared to theory in a least squared sense as indicated in Equation 3.19, where $w_i$ is the inverse square of the experimental line ratio uncertainty. No uncertainty is assigned to the simulated line ratios determined from theory, but they are scaled by a ratio of Einstein A-coefficients to their NIST equivalents.

$$\frac{\varepsilon_{826.7}}{\varepsilon_{842.7}} = \frac{A_{14\to5}\left(PEC^{(\text{exc})}_{1,14\to5}(n_e,Te)\frac{n_1}{n_4} + PEC^{(\text{exc})}_{2,14\to5}(n_e,Te)\frac{n_2}{n_4} + PEC^{(\text{exc})}_{3,14\to5}(n_e,Te)\right)}{A_{8\to3}\left(PEC^{(\text{exc})}_{1,8\to3}(n_e,Te)\frac{n_1}{n_4} + PEC^{(\text{exc})}_{2,8\to3}(n_e,Te)\frac{n_2}{n_4} + PEC^{(\text{exc})}_{3,8\to3}(n_e,Te)\right)} \tag{3.18}$$

$$\chi^2_i = w_i(LR_{i,\text{th}} - LR_{i,\text{exp}})^2 \tag{3.19}$$

Based on discussions with Stuart Loch's group at Auburn university, the R-matrix methods used to calculate the electron impact excitation cross sections are best at calculating the scattering rates

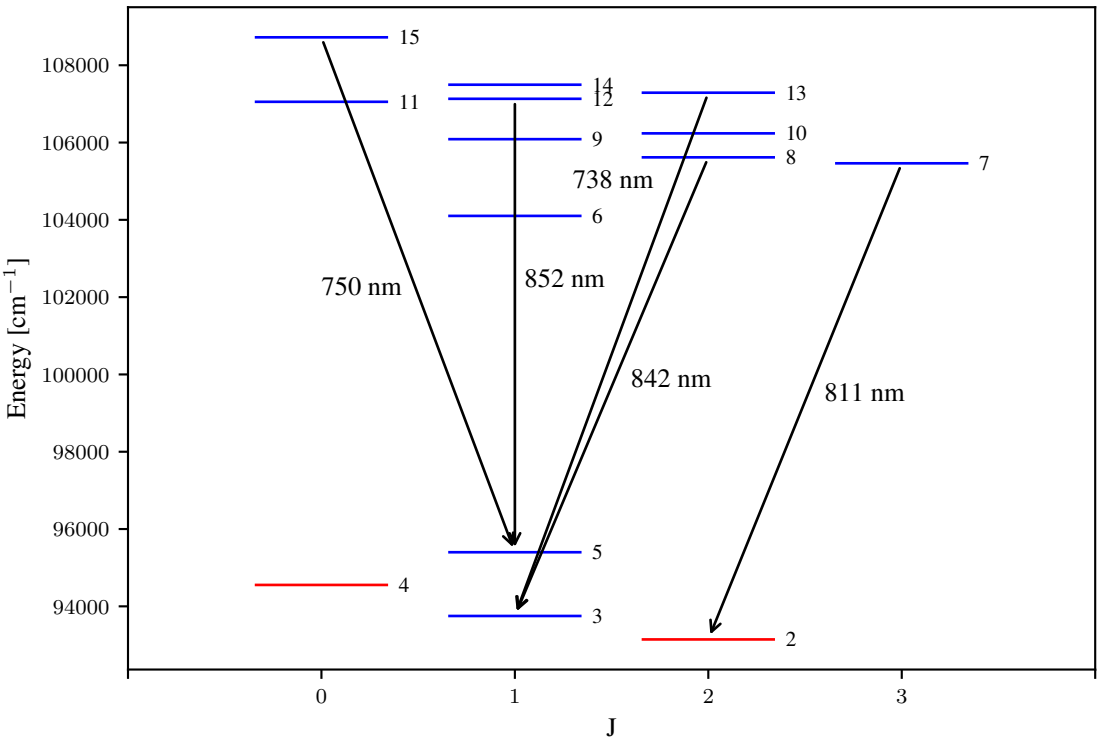


Figure 3.6: Partial Grotrian diagram of Ar I showing the transitions used in the line ratio spectroscopy algorithm. The wavelengths associated with each transition is shown, and the energy level is indicated to the right of the level line.

of incoming electrons, but are not optimized for calculating level energies or spontaneous transition rates. Connecting a particular excited level with the proper energy associated with that level is extremely important for calculating the emitted photon energies and ionization thresholds. The wavelength of an emitted photon, $\lambda$, is directly calculated from the difference in energy between the states involved in the transition, $E_i - E_j$, by $\lambda = hc/(E_i - E_j)$. If the energies are not correct, identifying state transitions from observed emission lines in the plasma would be nearly impossible. Similarly the difference between the ionization threshold and the energy of a particular level

directly affects the energy required to ionize an atom by electron impact. Calculating ionization rates with incorrect energies will yield erroneous ionization rates. Lastly, the spontaneous transition rates, i.e. the Einstein A-coefficients, allow the photon emission rate to be calculated from the excited state population. Any innacuracy in these transition rates will degrade the agreement between theoretical line ratios and experimental ones. In the calculation of the rate coefficients, the energies were already shifted to the NIST values as described in Arnold's thesis [62].

Many of the transition rates calculated by the group at Auburn agreed with NIST values within 20%-30%. However, that level of disagreement is outside the quoted uncertainties of many of the transition rates for neutral argon listed in NIST's database. When comparing experimental line ratios to line ratios calculated from PECs, the PEC sourced line ratios were multiplied by the correction factor of $C = A_{NIST}/A_{PEC}$.

The basic solution algorithm proceeds as follows:

1. Define a set of line ratios.

2. Initialize a set of 500 random combinations of $n_3$, $T_e$, $\frac{n1}{n4}$, and $\frac{n2}{n4}$ within predefined domain bounds as starting points.

3. Compute the total squared error – $\sum \chi_i^2$ (Equation 3.19) – for each point and save the 5 points with the least $\chi^2$ value.

4. Allow each test point to seek the best fit by minimizing $\sum \chi_i^2$ using a heavy ball gradient descent method using $n_e$, $T_e$, $\frac{n1}{n4}$, and $\frac{n2}{n4}$ as fitting parameters.

5. Return the plasma parameters for the test point with the least $\sum \chi_i^2$.

If the gradient descent optimization is terminated early, the shape of the $\sum \chi^2$ function for a particular spectrum can be visualized. Figure 3.7 shows one local minimum and the global minimum to one such $\sum \chi^2$ function for the $\frac{n1}{n4}$ ratio. The $\chi^2$ difference between these minimums

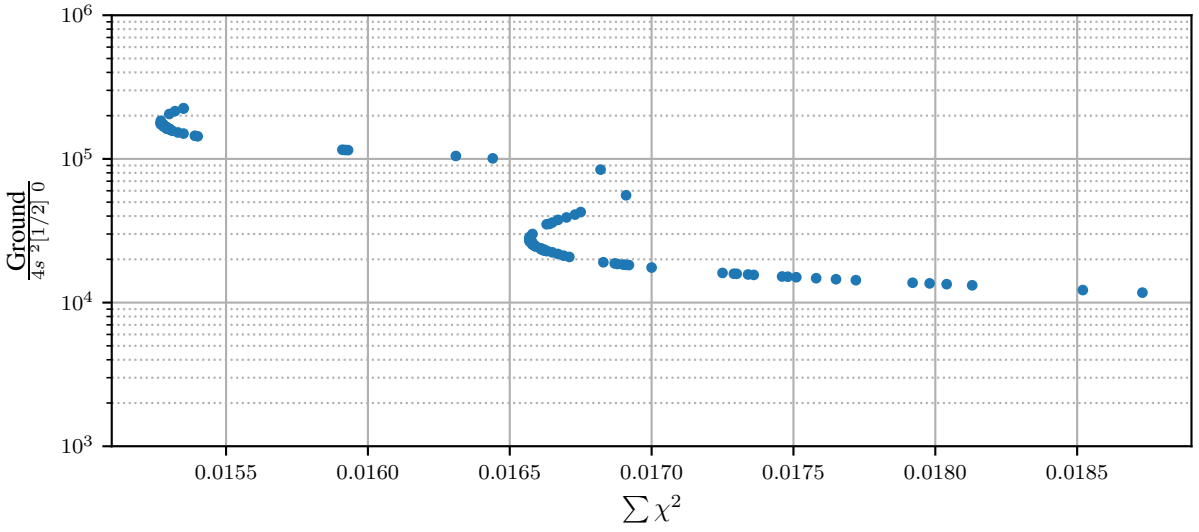


Figure 3.7: Terminating the gradient descent optimization early lets us peek at what the $\sum \chi^2$ function looks like. The $\sum \chi^2$ function has multiple local minima, two of which are shown here.

is only about 8%. It is important to note that for this particular solution, the statistical fluctuation in the best fit $\sum \chi^2$ due to the uncertainty in the experimental line ratio is on the order of 50%. So, even though a global or even a local minimum can be found for any particular experimental line ratio, the gradient of the $\sum \chi^2$ function is sufficiently shallow that a family of statistically significant solutions exist.

Indeed, if the level populations for the two possible solutions indicated in Figure 3.7 are plotted, the negligible difference between the two possible solutions is clear. Figure 3.8 shows the level populations for the 6th through 15th excited levels of neutral argon calculated at the two local minima shown in Figure 3.7. The two solutions, indicated by the squares and triangles, lie right on top of each other despite a 1.5 eV difference in electron energy.

By plotting the 'best fit' $g$ values with respect to the best fit $T_e$ values, as shown in Figure 3.9, the apparent scaling of the ground/4s $^2$[1/2] 0 ratio with temperature is evident. For a given 'best

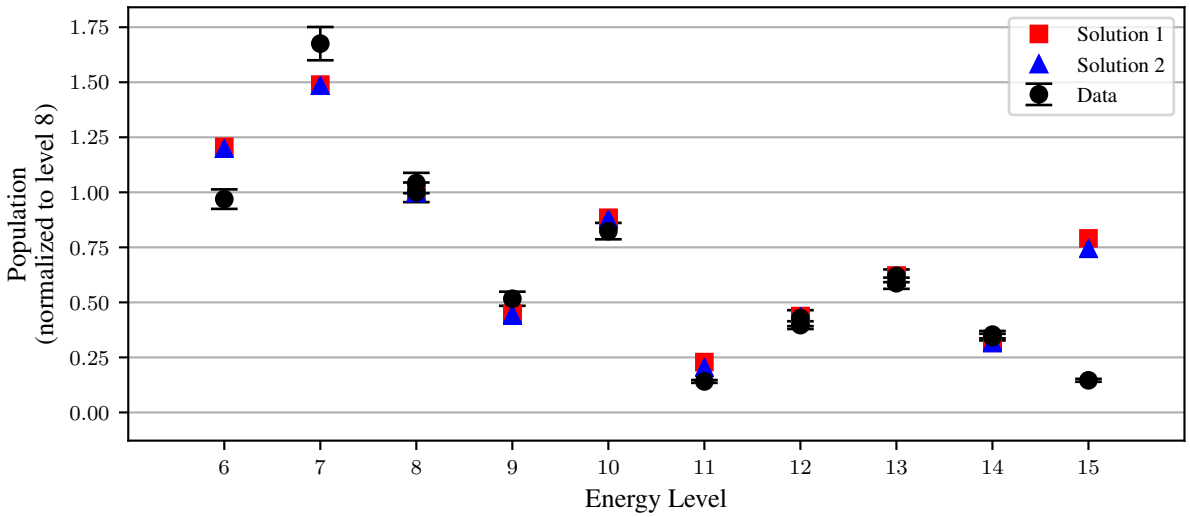


Figure 3.8: There is no discernible difference in the relative level populations determined from the two local minima indicated in Figure 3.7. Solution 1 has an electron temperature of 2.11 eV and a ground/4s $^2$[1/2] 0 ratio of $1.78 \times 10^5$. Solution 2 has an electron temperature of 3.68 eV and a ground/4s $^2$[1/2] 0 ratio of $2.81 \times 10^4$.

fit,' values for the ground/4s $^2$[1/2] 0 ratio and electron temperature can be taken from this curve with minimal impact to the quality of fit.

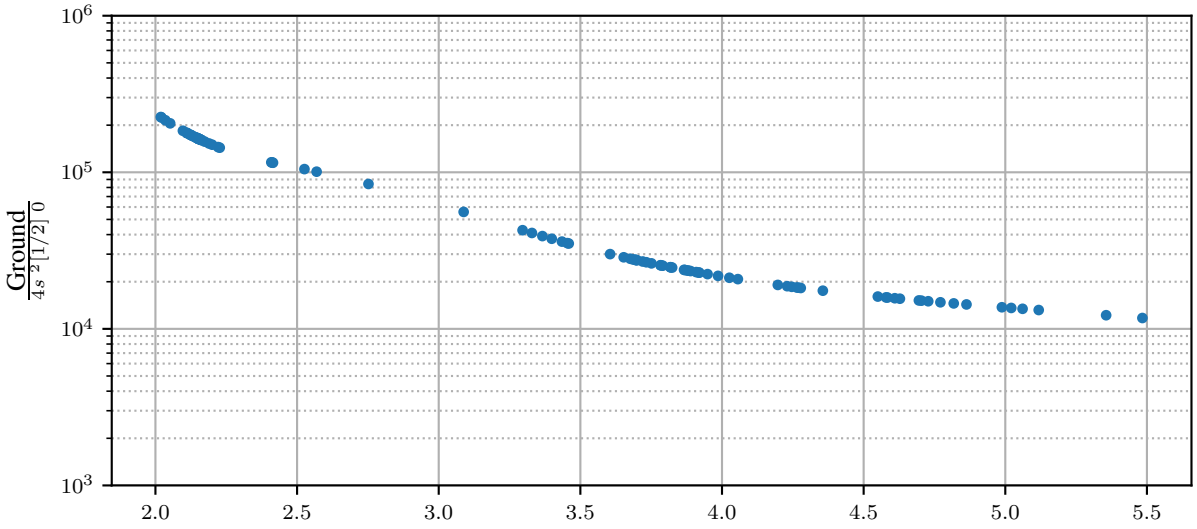


Figure 3.9: Terminating the gradient descent optimization early also shows how the ground/4s $^2$[1/2] 0 population ratio depends on the electron temperature.

# Chapter 4

# Laser Induced Fluorescence of Neutral and Singly Ionized Argon

Laser induced fluorescence (LIF) was introduced in section 2.3. This section will dive deeper into the theory underlying the LIF process and describe a method of measuring flow velocities that leverages the symmetry of the Zeeman effect. The first few paragraphs of this section are a repetition of section 2.3, but have been included again here for clarity.

The initial goal of the LIF measurement is to find the first moment of the velocity distribution function (VDF):

$$\langle V \rangle = \int_{-\infty}^{\infty} V f(V)\, dV \tag{4.1}$$

where $f(V)$ is the normalized velocity distribution function, and $V$ is magnitude of a particle's velocity in the direction of the laser.

The LIF scheme used to measure properties of the VDF describing a population of argon ion atoms is shown in Figure 4.1. Atoms initially in state '1' can be pumped to state '2' by absorbing photons emitted by a laser. The strength of this interaction can be monitored by collecting the fluorescence light emitted during the decay from state '2' to state '3'. As explained below, the intensity of fluorescence light will be proportional to the number of atoms able to absorb the laser light and undergo a transition, which is found by the convolution of the VDF with the laser spectral profile:

$$I \propto \int_{-\infty}^{\infty} f(V) * g(V)\, dV \tag{4.2}$$

where $g(V)$ is the linewidth of the laser in velocity space and the $*$ indicates a convolution.

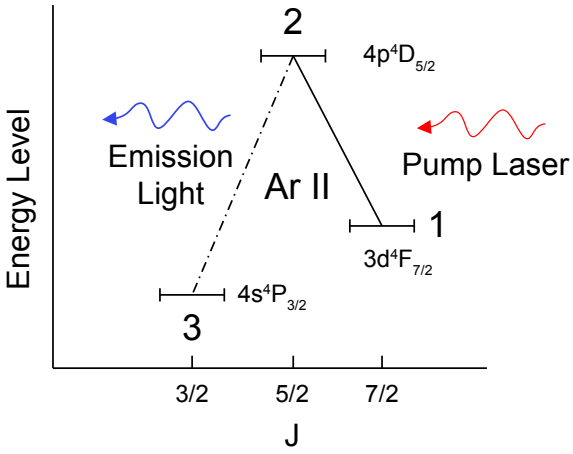


Figure 4.1: 668.614 Ar II LIF Scheme.

In a magnetized plasma, the Zeeman effect breaks the degeneracy of the atom's energy levels according to the interaction strength between the atom's magnetic moment and the background magnetic field. The energy shift for each level is given in Equation 4.3.

$$\Delta E = \langle nljm_j|\hat{H}_z|nljm_j\rangle, \tag{4.3}$$

where the Zeeman Hamiltonian, $\hat{H}_z = \mu_b g_j \mathbf{J}\cdot\mathbf{B}$, and the Landé g-factor,

$$g_j = 1 + \frac{j(j+1)+s(s+1)-l(l+1)}{2j(j+1)}, \tag{4.4}$$

are assumed to have their usual expressions.

The effect of this energy splitting on the $4\mathrm{p}^4\mathrm{D}_{5/2}$ and $3\mathrm{d}^4\mathrm{F}_{2/2}$ levels involved in the pumping process is shown in Figure 4.2a. By subtracting the energy shift of the upper levels from the lower levels, the shift in the frequency of laser light required to cause a transition can be calculated as shown in Equation 4.5:

$$\Delta\nu_{\Delta j=\pm1} = [(g_2-g_1)m_{j,2} \pm g_1]\frac{\mu_B B}{h}. \tag{4.5}$$

For a small volume of atoms under investigation, the fraction of atoms with a certain magnitude of their total angular momentum oriented along the magnetic field line will be not be equal. As a

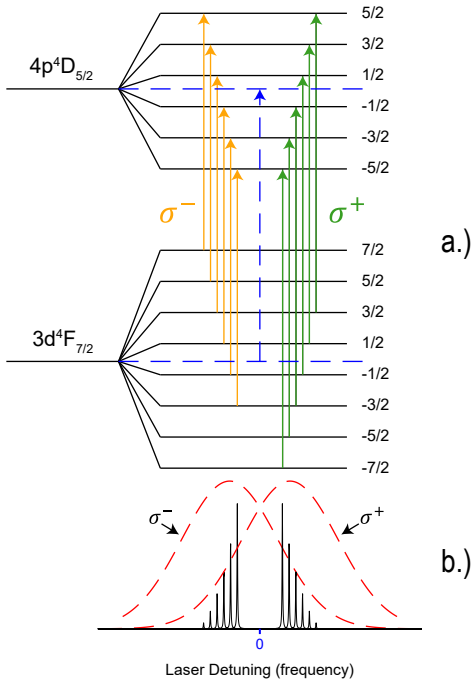


Figure 4.2: The $\Delta m_j = \pm 1$ dipole selection rule combines with Zeeman splitting to produce two groupings of transition lines labeled $\sigma^+$ and $\sigma^-$, shown in part (a). The figure in part (b) shows the envelope (red dashes) created by the convolution of all the lines (black lines) with a Maxwellian velocity distribution function.

result, the intensity of individual Zeeman transitions will be different. The relative intensities of the Zeeman lines are given by Condon and Shortley as [63]:

$$|\langle nljm_j|\mathbf{P}|n'l'j-1m_j\mp 1\rangle|^2 = |\langle nlj|\mathbf{P}|n'l'j-1\rangle|^2\frac{1}{2}(j\pm m_j)(j\pm m_j-1) \qquad (4.6)$$

The frequency shifts and relative intensities are shown by the black lines in Figure 4.2b. The mirror symmetry about $\nu = 0$ seen in the figure for the $\Delta m_j = \pm 1$ transitions is a direct result of the $\pm g_j$ term in Equation 4.5. The fundamental transition frequency from the $3d^4F_{7/2}$ state to the $4p^4D_{5/2}$ state is then directly between the two $\sigma^+$ and $\sigma^-$ groupings.

As the laser is scanned across the transitions, the LIF signal is proportional to the fraction of atoms making the $\Delta m = +1$ and $\Delta m = -1$ transitions and is thus weighted by the appropriate relative intensity:

$$A_i = \frac{(j \pm m_{j,i})(j \pm m_{j,i} - 1)}{2\sum_i (j \pm m_{j,i})(j \pm m_{j,i} - 1)} \tag{4.7}$$

The LIF signal is then given by the total VDF, which is the sum of contributions from each of the Zeeman transitions:

$$I_{tot} \propto \int_{-\infty}^{\infty} \sum_i A_i \Big[ f_i(V + V_{z,i}) * g(V) \Big] \, dV \tag{4.8}$$

where $\sum_i$ is over all $-J \leq m_j \leq J$ quantum numbers, $f_i$ is the velocity distribution function for atoms with angular momentum quantum number $m_j$, $V_{z,i}$ is the apparent velocity offset introduced by the Zeeman effect frequency shifts given in Equation 4.5, and $g(V)$ is, again, the line shape of the laser in velocity space. The Doppler effect relates the apparent velocity shift introduced by the Zeeman effect frequency shifts.

$$V_z = c\Delta\nu_z/\nu_0 \tag{4.9}$$

where $\Delta\nu_z$ is the frequency offset given by Equation 4.5, $\nu_0$ is the fundamental transition frequency of an atom with zero velocity, $V_z$ is the apparent velocity of the atom, and c is the speed of light.

If the laser line width is sufficiently narrow, and can be considered to be a delta function, Equation 4.8 then becomes:

$$I_{tot} \propto \sum_i A_i f(V + V_{z,i}) \tag{4.10}$$

If the Doppler relation from Equation 4.9 is substituted into Equation 4.10, the intensity of the LIF signal in frequency space due to the sum of Zeeman components becomes:

$$I_{tot} \propto \sum_i A_i f\left(\frac{c}{\nu_0}(\Delta\nu + \Delta\nu_{z,i})\right) \tag{4.11}$$

where $\nu_0$ is the fundamental transition frequency for the transition from state '1' to state '2', $\Delta\nu$ is the difference between the fundamental transition frequency and the laser frequency, and $\Delta\nu_{z,i}$ is the Zeeman frequency shift given in Equation 4.5.

Taking the first moment of this 'LIF distribution function' gives:

$$\langle \Delta\nu \rangle = \int_{-\infty}^{\infty} \sum_i \Delta\nu A_i f \left( \frac{c}{\nu_0}(\Delta\nu + \Delta\nu_{z,i}) \right) \, d\Delta\nu \tag{4.12}$$

Using the change of variables, $\Delta\nu' = \Delta\nu + \Delta\nu_{z,i}$ pulls the frequency offset out of the distribution function:

$$\langle \Delta\nu \rangle = \sum_i \int_{-\infty}^{\infty} \Delta\nu' A_i f \left( \frac{c}{\nu_0}\Delta\nu' \right) \, d\Delta\nu' - \sum_i \Delta\nu_{z,i} A_i \int_{-\infty}^{\infty} f \left( \frac{c}{\nu_0}\Delta\nu' \right) \, d\Delta\nu' \tag{4.13}$$

By summing over both $\Delta m = +1$ and $\Delta m = -1$, the second part of Equation 4.13 sums to zero. By definition $\sum_i A_i = 1$, and the flow velocity can be recovered by:

$$\langle V \rangle = \frac{c}{\nu_0} \langle \Delta\nu \rangle \tag{4.14}$$

This fact was also briefly mentioned in Edrich's doctoral thesis, but the implications on the flow velocity were not explored nor utilized [64]. Edrich was focused on extracting ion temperatures and showed that a correction for the Zeeman effect is required.

By way of example, a one dimensional Maxwellian velocity distribution is given by:

$$f(V_p)\, dV = \frac{1}{V_{th}\sqrt{\pi}} \exp \left[ - \left( \frac{V - V_f}{V_{th}} \right)^2 \right] \, dV \tag{4.15}$$

where $V_{th}$ is the thermal velocity and $V_f$ is the flow velocity, $\langle V \rangle$. Here the particle's velocity is $V_p = V + V_f$. Including the frequency offset for the Zeeman components and substituting the Doppler relation again yields a relation describing the fraction of atoms absorbing at a given frequency:

$$f(\Delta\nu) df = \sum_i \frac{A_i c}{\nu_0 V_{th}\sqrt{\pi}} \exp \left[ - \left( \frac{c\Delta\nu_0 - V_f\nu_0 + c\Delta\nu_{z,i}}{\nu_0 V_{th}} \right)^2 \right] \, d\Delta\nu \tag{4.16}$$

The first moment then becomes:

$$\langle \Delta\nu \rangle = \int_{-\infty}^{\infty} \sum_i \frac{A_i c \Delta\nu}{\nu_0 V_{th}\sqrt{\pi}} \exp \left[ - \left( \frac{c\Delta\nu - V_f\nu_0 + c\Delta\nu_{z,i}}{\nu_0 V_{th}} \right)^2 \right] \, d\Delta\nu \tag{4.17}$$

Using the change of variables $\nu' = c\Delta\nu - V_f\nu_0 + c\Delta\nu_{z,i}$ yields:

$$\langle\Delta\nu\rangle = \sum_i \frac{A_i}{c\nu_0 V_{th}\sqrt{\pi}} \int_{-\infty}^{\infty} (\nu' + V_f\nu_0 - c\Delta\nu_{z,i}) \exp\left[-\left(\frac{\nu'}{\nu_0 V_{th}}\right)^2\right] d\nu' \tag{4.18}$$

$$\langle\Delta\nu\rangle = \frac{V_f\nu_0}{c\nu_0 V_{th}\sqrt{\pi}} \nu_0 V_{th}\sqrt{\pi} - \sum_i \Delta\nu_{z,i} = \frac{V_f\nu_0}{c} - \sum_i \Delta\nu_{z,i} \tag{4.19}$$

Then, from Equation 4.14:

$$\langle V\rangle = \frac{c}{\nu_0}\langle\Delta\nu\rangle = V_f - \frac{c}{\nu_0}\sum \Delta\nu_{z,i} \tag{4.20}$$

Recall from Equation 4.5 that $\Delta\nu$ has symmetric $\Delta_j = +1$ and $\Delta_j = -1$ components. So, Equation 4.20 can be rearranged to show how the $\sigma^+$ and $\sigma^-$ grouping of the LIF signal contribute to the first moment of the VDF. As shown in Equation 4.21, the first moment of each grouping is one half of the total flow velocity plus a perturbation due to the Zeeman effect. By finding the midpoint between the groupings, the Zeeman effect perturbations cancel and only the unperturbed flow velocity remains.

$$\langle V\rangle = \frac{1}{2}(V_f - \frac{c}{\nu_0}\sum \Delta\nu_{\Delta j=+1}) + \frac{1}{2}(V_f - \frac{c}{\nu_0}\sum \Delta\nu_{\Delta j=-1}) \tag{4.21}$$

Finding $\langle V\rangle$ as shown in this example using a Maxwellian velocity distribution function is only strictly true if underlying VDF is symmetrical, like a Maxwellian distribution. However, the first moment of the LIF signal, $\langle\nu\rangle = \int \nu\text{LIF}(\nu)\, d\nu$, will still yield $\Delta\nu$ and $\langle V\rangle$ can still be determined from Equation 4.14 even when the velocity distribution function is not symmetric. The only requirement is that the spectral range of the LIF scan is sufficient to cover all Zeeman transitions. Eliminating the need to worry about the magnetic field strength and the particular shape of the LIF spectrum and how it affects the fit is the primary benefit of using the midpoint between the two Zeeman groupings.

Some attention must be paid to the spectral distribution of the fluorescence transition in addition to the absorption transition. One might be concerned that by pumping atoms to a different state the

plasma equilibrium is sufficiently disturbed that the plasma cannot respond quickly to the square wave laser excitation pulses causing a deviation of the LIF response from linear proportionality. However, the LIF process can be approximated as steady state under the assumption that the time constants associated with the atomic transitions are much smaller than the observation time. The relaxation times can be approximated as $\tau \sim (\sum n_e q_{i\to j} + \sum A_{i\to j})^{-1}$, where $n_e$ is the plasma density in units of $m^{-3}$, $q_{i\to j}$ is the electron impact excitation rate coefficient in $m^3/s$, and $A_{i\to j}$ is the typical Einstein A-coefficient in $s^{-1}$. For plasma densities in the range $10^{16}m^{-3} - 10^{19}m^{-3}$, electron temperatures in the range 1-100 eV, and atom temperatures in the range .1-3 eV, the excited state lifetime is on the order of tens to hundreds of nanoseconds. This is much shorter than the kHz chopping frequency and the 10s of seconds it takes to scan the pump laser across the relevant range. Thus the fraction of pumped atoms undergoing a radiative transition from state '2' to state '3' will be linearly proportional to the pumping rate. Furthermore, since the atom remains in a magnetic field during the transition from state '2' to state '3', the spectral distribution of the fluorescence photons is also affected by the Zeeman effect. If the full spectrum of fluorescence light is collected by using a filter with a wide enough bandwidth, then all of the individual Zeeman contributions from the emission process will be collected and accounted for. Therefore the LIF signal is linearly proportional to the absorption spectra, and the details of the fluorescence transition become unimportant.

To evaluate the reliability of using this midpoint technique, a more traditional fitting procedure is undertaken. This procedure consists of using the more accurate Voigt profile to fit each set of LIF data, using the thermal temperature and Doppler shift as fitting parameters. The shift due to the Zeeman effect is accounted for by using the measured magnetic field strength values shown in Figure 4.3. Since only one curve is needed to obtain a measurement in this case, fitting both the $\sigma^{\pm}$ lines yields two estimates of the flow velocity.

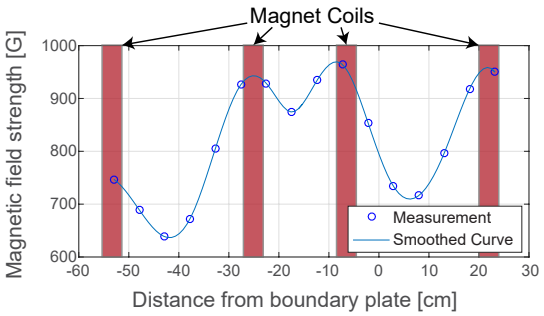


Figure 4.3: Axial magnetic field profile in the MARIA device. Measurements were taken in the region from 0 to 20 cm.

The ion velocity measured by using both the midpoint method and the verification process is shown in Figure 4.4. The techniques agree well with one another, with both seeing the same approximately exponential increase in flow velocity with decreasing distance from the boundary plate. Because the verification is done by measuring the magnetic field and fitting a convolved profile to each of the $\sigma^+$ and $\sigma^-$ groupings, two estimates of the flow velocity can be made for each axial location. Both of these results are shown for each location in Figure 4.4. The lack of perfect agreement between the two flow velocity measurements from the fitted convolution could be due to an imperfect measurement of the magnetic field at this location, or a fitting error. Using the midpoint method, which does not require measurement or knowledge of the local magnetic field strength, leads to measurements of the the flow velocity with reduced uncertainty and are thus the more accurate result.

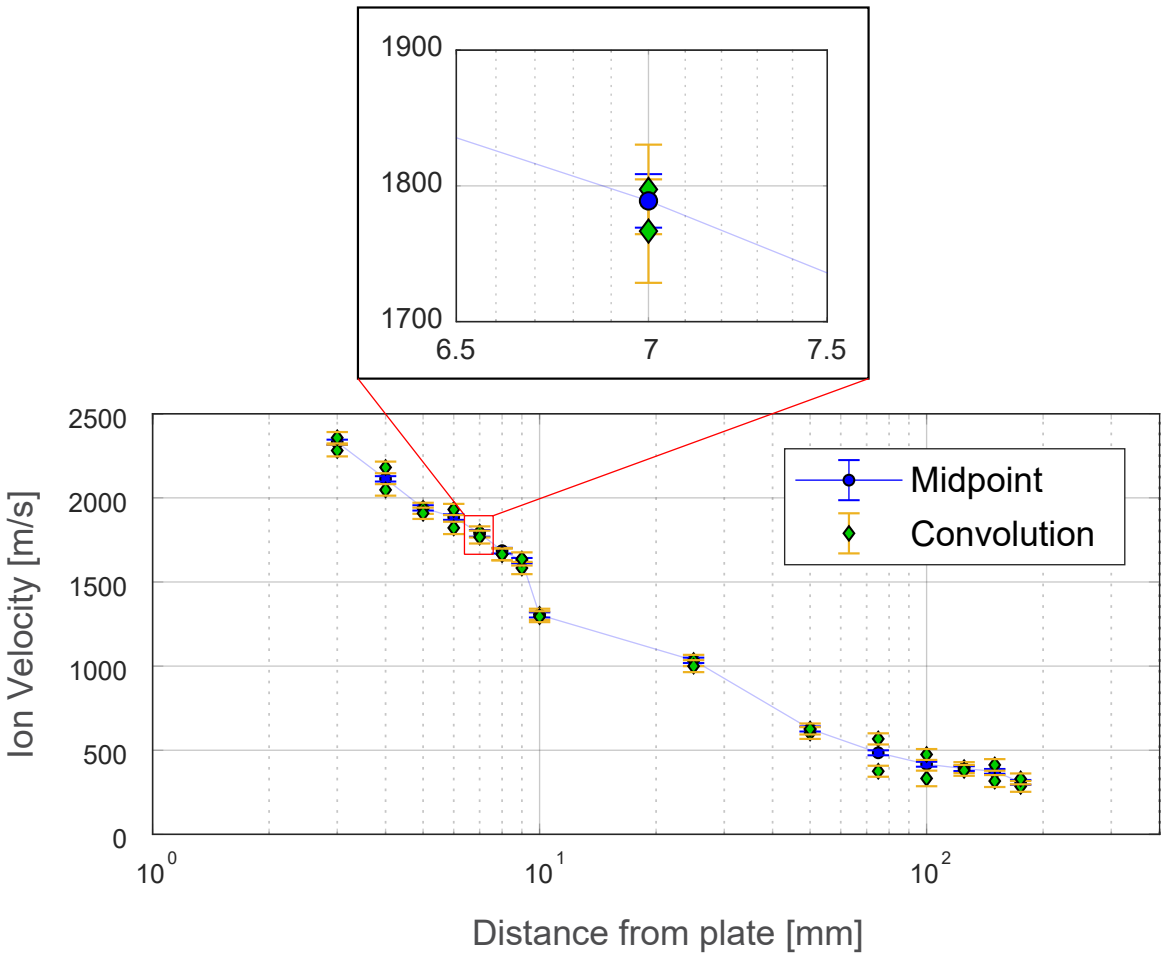


Figure 4.4: The flow velocities measured by fitting the convolved profile to the LIF signal and by using the midpoint technique with a Gaussian fit yield nearly identical results. Fitting the convolved profile produced velocity estimates for both the $\sigma^+$ and $\sigma^-$ lines, so both estimates are plotted. Uncertainties are shown more clearly on the inset image. Here, a positive velocity means motion in the direction of the laser $\mathbf{k}$ vector (towards the plate).

# Chapter 5

# Experiment

## 5.1 The MARIA Helicon Device

Experimentally studying helicon plasmas would be a difficult endeavor without a device that can produce helicon plasmas; enter the **M**agnetized **A**nisot**R**opic **I**on-distribution **A**pparatus (MARIA). MARIA is the evolution of the device used in a previous graduate student's research [65]. The current version, depicted in Figure 5.1 is 2 m long with a maximum magnetic field strength of 1000 G and 10 kW of available RF power. The chamber is constructed of borosilicate glass tube with an inner radius of 7.5 cm. The gas inlet and vacuum pump are located on the same end of the chamber while the axial magnetic field is pointing towards the 'blind' end away from the gas source.

A CAD rendering of the MARIA device, shown in Figure 5.2, gives a better indication of the spatial arrangement of the device. The plasma chamber is constructed from borosilicate glass crosses with the main bore being 14 cm in diameter and two smaller tubes perpendicular to the main bore that are 10 cm in diameter. These crosses permit flexible installation of diagnostics such as the Langmuir probe seen on the device's left side. The helicon antenna is located between the two magnets closest to the vacuum pumps, while the boundary plate referenced in this work is located at the far end of the chamber, labeled 'Target Chamber' in Figure 5.1. The magnetic field is oriented along the axis pointing away from the vacuum pumps (to the upper left in the figure), and this direction is referred to as downstream. A primary benefit of the glass chamber is that its transparency permits collection optics to be placed virtually anywhere along the chamber. The

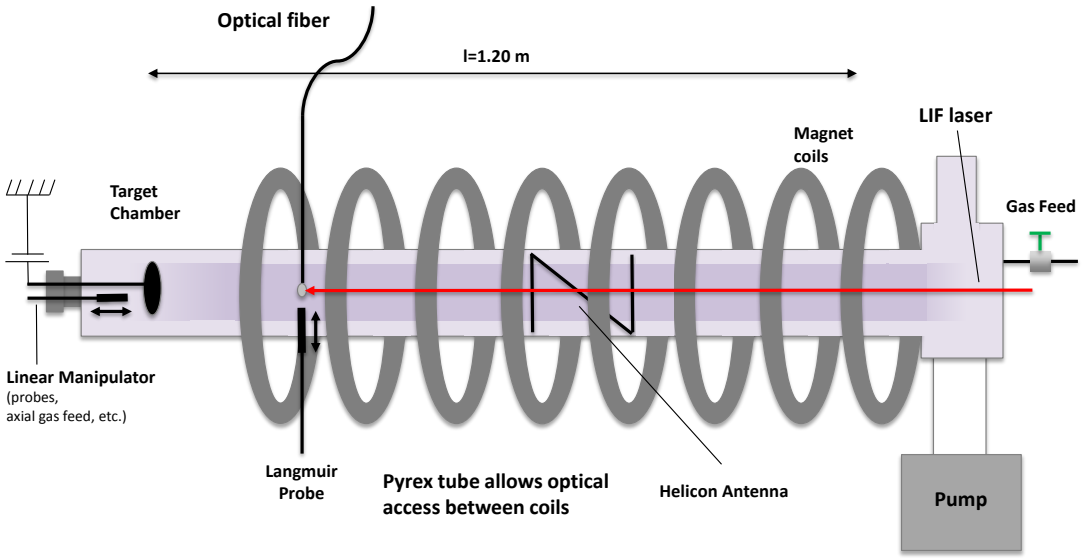


Figure 5.1: The gas source and pumping are located on the same side in MARIA. A floating boundary plate is placed downstream of the antenna in the target chamber area. Fiber coupled laser light is shown down the axis of the device while fluorescence light is collected perpendicular to the magnetic field. An RF compensated Langmuir probe is placed 2/3 the length of the chamber from the pump and about 1/3 the chamber length from the antenna.

LIF collection telescope can be seen mounted on rails above the device, and the array of optical fibers collecting light for the spectrometer can be seen in the view on the right. However, care must be taken when observing through the chamber wall as it can be coated by metals sputtered by the intense plasma and alter the glass transmission spectrum. Additionally diffraction caused by nonuniformities in the glass walls can reduce the spatial resolution and accuracy of measurements.

For most of the results shown in this paper, the RF system consists of a water cooled solid state 10 kW CW generator that is coupled to the 14 cm long $m = +1$ helical antenna through a $\pi$ matching circuit, except with the output capacitor in series with the load instead of parallel with it. The RF generator contains built-in directional couplers that permit real-time monitoring of

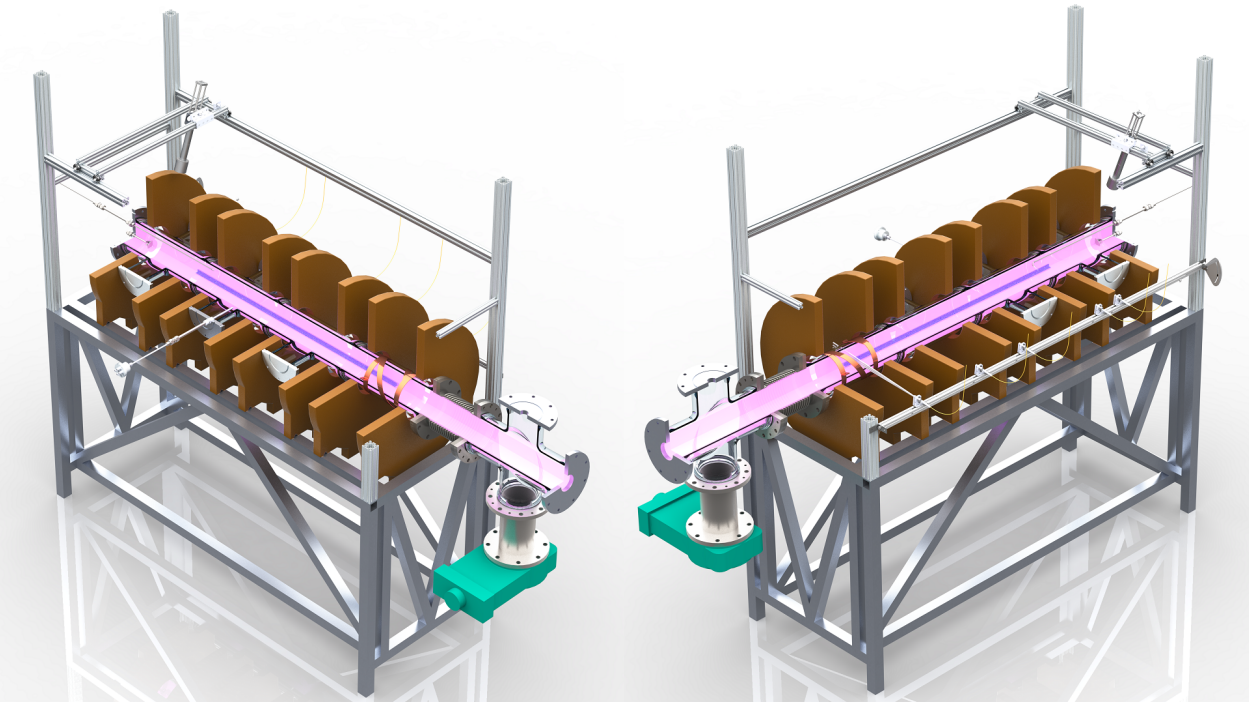

Figure 5.2: MARIA is a 1.2m long device with a peak axial magnetic field of 1000 G and 10 kW of available RF power. The chamber is a 7.5 cm radius borosilicate tube.

the forward and reflected power. Despite 10 kW of available RF power, cooling constraints limited power levels to less than 1 kW for the vast majority of this work. A cooling upgrade was completed on March 20, 2019, and some data presented in this thesis made use of up to 4 kW of RF heating power. A further upgrade to a water cooled antenna will be needed to enable CW operation up to the full 10 kW.

Typical MARIA plasmas are in the range of $5 \times 10^{17}$ m$^{-3}$ to $1 \times 10^{19}$ m$^{-3}$ for $P_{\mathrm{RF}} \leq 1.8$ kW and magnetic fields $B \leq 1000$ G. Langmuir probe measurements, shown in Figure 5.3, indicate the characteristic linear scaling of electron density with magnetic field above 500 G [66]. Figure 5.4 shows the relative change in emitted light intensity as a function of magnetic field strength for neutral and ion lines. The 422.8 nm Ar II ion emission line, shown in red, shows an approximately linear intensity increase beyond 450 G which qualitatively indicates the linear scaling of density

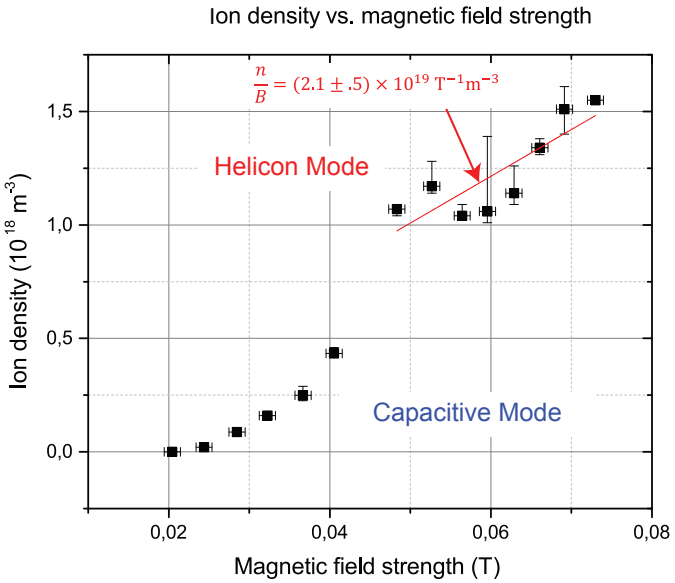


Figure 5.3: Langmuir probe measurements of the electron density as a function of the magnetic field strength show the linear scaling characteristic of the plasma helicon mode [66].

with magnetic field strength in this 700 W plasma. The appearance of argon ion emission lines aligns with the sudden jump in electron density shown in Figure 5.3 at about 450 G. Additionally, the initial rise in neutral argon emission intensity up to 300 G followed by gradual decay hints at the increasing ionization rate.

While the various diagnostics are a good quantitative means to investigate the plasma, a major advantage at MARIA is that the plasma can be seen visually with the naked eye thanks to the glass chamber construction. At low magnetic field strength, 200 G or less, the plasma is typically quite bright near the antenna but takes on a very diffuse character down stream of it. The plasma also appears to have a 'hollow' center that does not radiate strongly. This mode of operation is attributed to a capacitive power coupling mode. At higher magnetic field strengths, usually in the range of 350-450 G, a distinct radiative core develops in the plasma. The pinkish color attributable to neutral argon emission, and confirmed by spectroscopic measurements lacking significant argon ion emission, indicates a neutral dominated plasma with low ion fraction. As soon as the very rapid

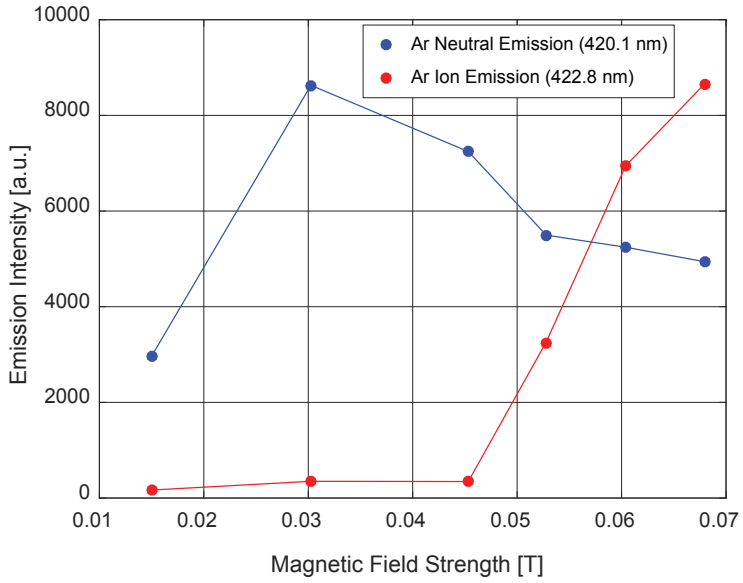


Figure 5.4: Spectral measurements in MARIA plasmas also show a transition to linear scaling of ion emission beyond about 450 G. After this transition there is a distinct decrease in the neutral argon emission.

jump into the helicon mode takes place a distinct blue core, owing to argon ion emission, starts to develop. Initially the blue core is somewhat faint, growing progressively brighter as the magnetic field strength is increased. This progression is shown in Figure 5.5.

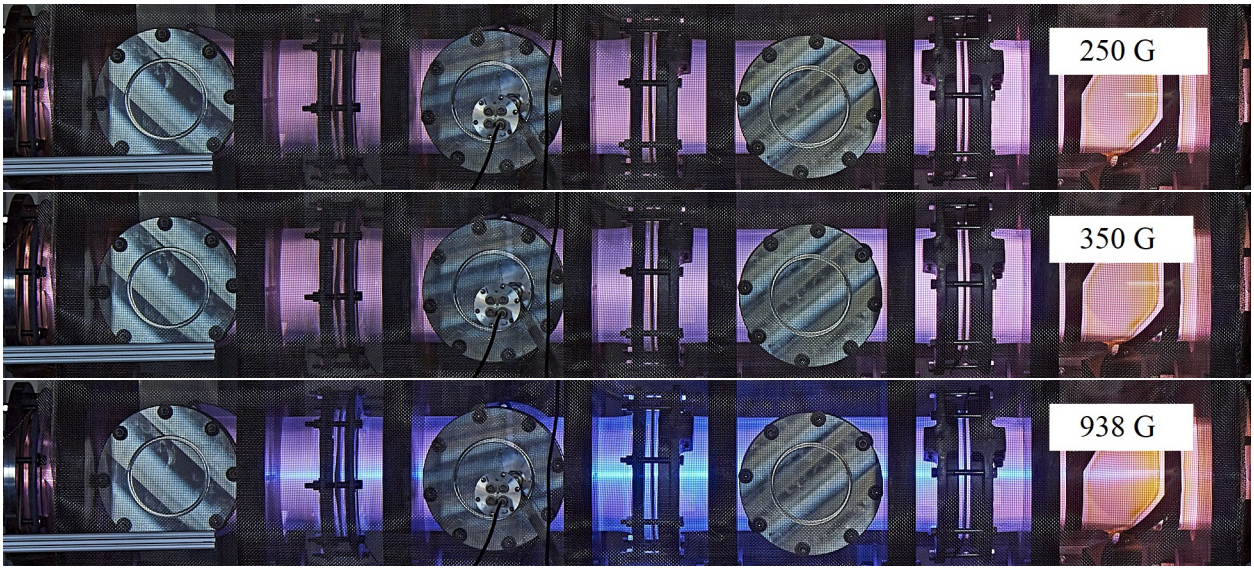


Figure 5.5: As the magnetic field strength increases, the visual character of MARIA plasmas evolve. From top to bottom: 250 G low density capacitive coupling, 350 G 2x higher electron density inductive coupling, 938 G 10x higher density helicon mode.

## 5.2 Narrow Bandwidth LIF System

The usefulness and theory underlying LIF is discussed at length in Chapter 4. The hardware implementation and details regarding the data analysis techniques are discussed here.

The optical arrangement used in this work is depicted schematically in Figure 5.6a and the hardware is shown in Figure 5.6b. The LIF system consists of a 668 nm Toptica DL100 diode seed laser amplified by a Toptica BoosTA tapered amplifier, producing a final power output of 420 mW, which is shined along the axis of the device. The beam is passed through two 10% beamsplitters, with one portion going to a Burleigh WA1000 wavemeter and the other portion passing through a molecular iodine gas reference cell before terminating in a Coherent Model 240 Spectrum Analyzer. The remaining laser power is passed through an optical chopper, coupled to a 50 $\mu$m optical fiber and routed to the plasma chamber. The light exiting the optical fiber is first collimated, passes through a linear polarizer, a $\lambda/4$ wave plate, and a quartz window before passing through the plasma. The laser beam terminates in a beam dump built into an in-plasma boundary plate. Right-hand or left-hand circularly polarized light is produced by rotating the $\lambda/4$ wave plate.

Fluourescence light from the plasma is collected by a telescope, focused onto the end of an optical fiber, and shined on a ThorLabs PMM01 photomultipliter tube (PMT) after passing through a 1 nm bandpass filter. The PMT signal is routed to a Stanford Research Systems SR510 Lock-In Amplifier to extract the signal from the strong background radiation.

For radial LIF measurements, the laser is shined radially through the plasma, instead of along the axis. In this configuration the laser light is propagating perpendicular to the magnetic field, and increased signal to noise ratio is gained by linearly polarizing the laser light in the direction of the magnetic field and pumping the $\pi$ lines of the Zeeman effect. The $\pi$ transitions, for which $\Delta m_j = 0$, have intensities twice that of the $\sigma$ lines.

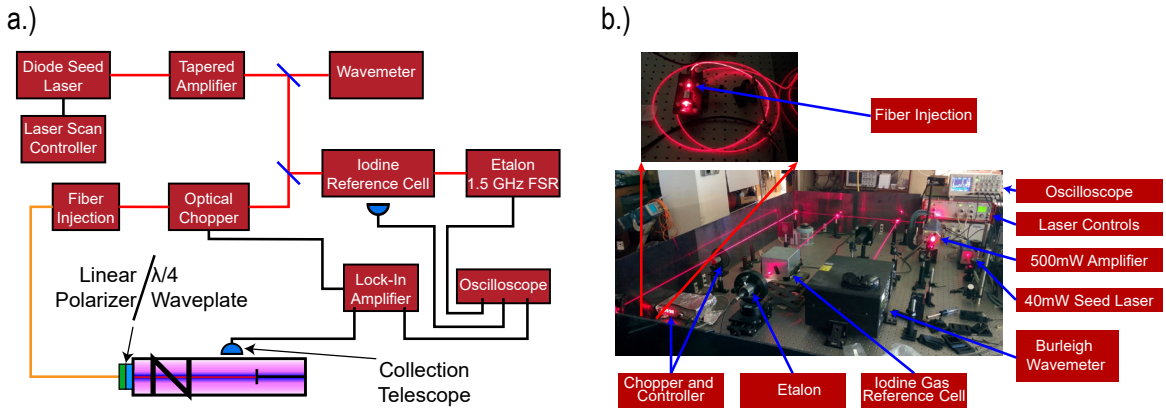


Figure 5.6: a.) Schematic layout of the optical configuration used in this work. Black lines denote BNC signal cables, red lines denote the laser beam line, and the orange lines denote optical fibers. b.) Overview of the optical table layout used in this work.

Once the laser is tuned to the right wavelength, the absolute wavelength reference is taken from the iodine reference cell, not the wavemeter, thanks to increased precision. To account for variations in laser output power, the laser light intended for the wavemeter was shined instead on a photodiode. The LIF response data can then be normalized to the laser power such that accurate comparisons can be made between the intensity of different sets of data which may have had slightly different laser power due to changes in the tuning.

### 5.2.1 Data Reduction and Analysis

The analysis consists of three primary phases: characterization of the pump laser source and relative wavelength calibration, absolute wavelength calibration, and curve fitting. Each of these steps was performed on each set of data. The process of determining the wavelength of the absolute wavelength reference was only performed once, but in each dataset the appropriate peak had to be identified.

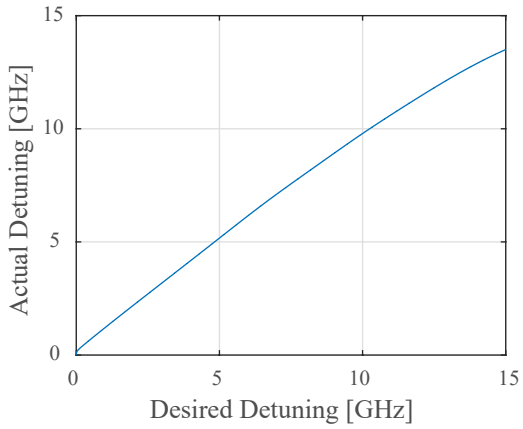


Figure 5.7: While the ramp input for the laser frequency tuning and the oscilloscope used for measurement are linear in time, the response of the actual laser frequency to the ramp input is not linear. This non-linearity must be accounted for during data analysis in order for models to be properly fit to the data.

#### 5.2.1.1 Relative Laser Frequency Calibration

During the actual LIF measurement, the seed laser is scanned over a range of approximately 15 GHz in the vicinity of the argon atom fundamental transition frequency by a 0-5V ramp input over about 100 seconds. The wavelength tuning of the seed laser is not quite linear, so an initial scaling must be made in order to recover true VDF profiles. The correction is made possible by a Coherent Model 240 confocal Fabry-Perot etalon with a 1.5 GHz free spectral range. The etalon acts as an ultranarrow bandpass filter, with a repeating transmission maximum every 1.5 GHz. By fitting the spectral width between each of the etalon transmission peaks with a cubic spline, a correction function for the nonlinearity is realized. The actual laser detuning vs. the detuning desired via the ramp input as measured by the etalon is shown in Figure 5.7. The deviation between the true and expected frequency grows towards larger desired frequency, becoming significant above 10 GHz.

#### 5.2.1.2 Absolute Wavelength Reference

Although the etalon provides an accurate means to measure relative frequencies within a laser scan, it provides no information about the absolute frequency of the laser. The method of using a diatomic iodine gas reference cell described by Keesee *et al* is followed as an absolute frequency reference [29]. However, the wavelength of the prominent peak around 668.614 nm is subject to some controversy. Keesee *et al* report the wavelength of the prominent peak to be at 668.6144 nm, while Woo *et al* report a wavelength of 668.6126nm [67]. This discrepancy could result in an absolute velocity difference of 807 m/s. By reflecting the laser off of a reflective surface in the plasma, an LIF signal was obtained from a laser beam with the opposite $\mathbf{k}$ as shown in Figure 5.8. The flow speed in lab coordinates in the same observation volume should be identical irrespective of sign of $\mathbf{k}$. This method was used in this work to reevaluate the appropriate iodine reference wavelength for argon ion measurements. To build up some statistics for the reference wavelength, the appropriate wavelength was calculated 7 times over a range of plasma parameters and the average was found to be 668.61272 nm $\pm$ $2.56 \times 10^{-5}$ nm, similar to Woo. The individual calculated values are shown in Figure 5.9. The average value is indicated by the thick black line, and the location of the peak is indicated by the arrow in the frame to the right.

A similar process was used to further constrain the wavelength of the peak near the neutral argon LIF wavelength of 667.6125 nm. Unfortunately, the neutral argon atoms move much more slowly compared to the ions. Performing the same analysis used for the ion line yielded inconclusive results since the $\mathbf{k} \cdot \mathbf{V}$ and $-\mathbf{k} \cdot \mathbf{V}$ signals were indistiguishable. This made it impossible to identify two different peaks. A different approach was thus used for the neutral line. By shining the laser radially through the plasma, the laser light coould be reflected off of a mirror and the same type of analysis can be implemented. By covering the mirror in a non-reflective material, an LIF signal for $\mathbf{k} \cdot \mathbf{V}$ alone could be measured. By uncovering the mirror, the $-\mathbf{k} \cdot \mathbf{v}$ component could

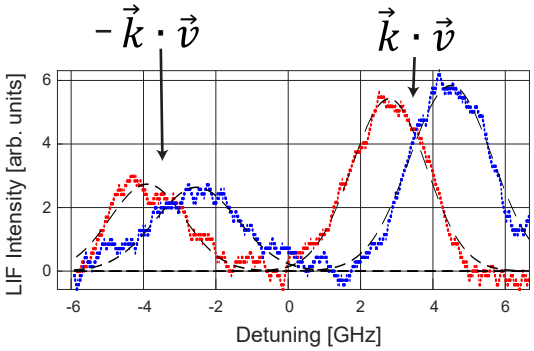


Figure 5.8: The laser used in the LIF process was reflected off a partially reflective surface in the plasma chamber. By capturing the LIF response for the beam propagating in both directions, both the $\mathbf{k}\cdot\mathbf{V}$ and $-\mathbf{k}\cdot\mathbf{V}$ terms can be measured.

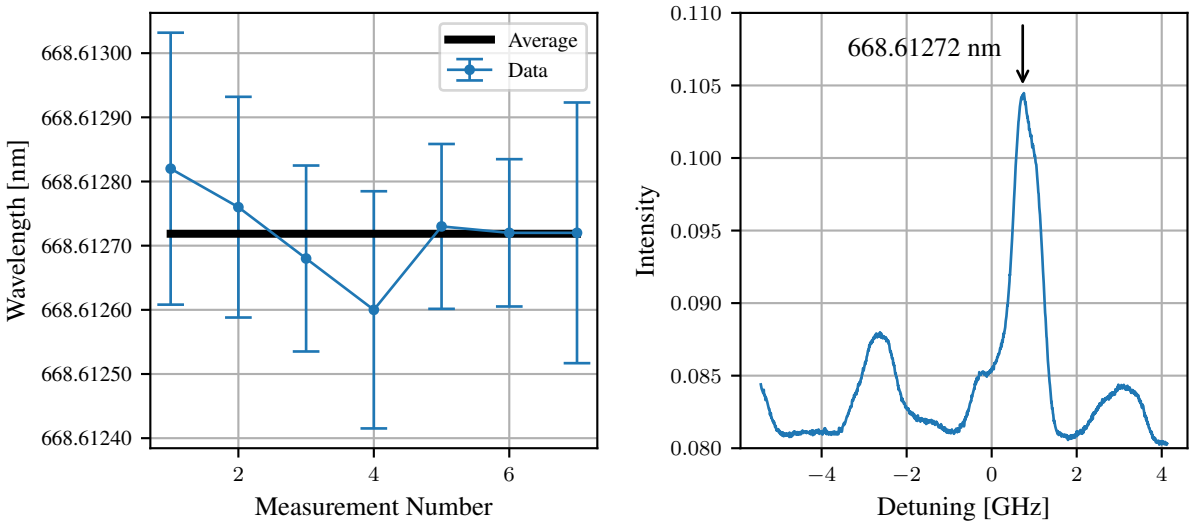


Figure 5.9: The wavelength for the prominent molecular iodine peak used for calibrating the singly ionized argon LIF measurements was found to be 668.61272 nm $\pm$ 2.56 $\times$ $10^{-5}$ nm.

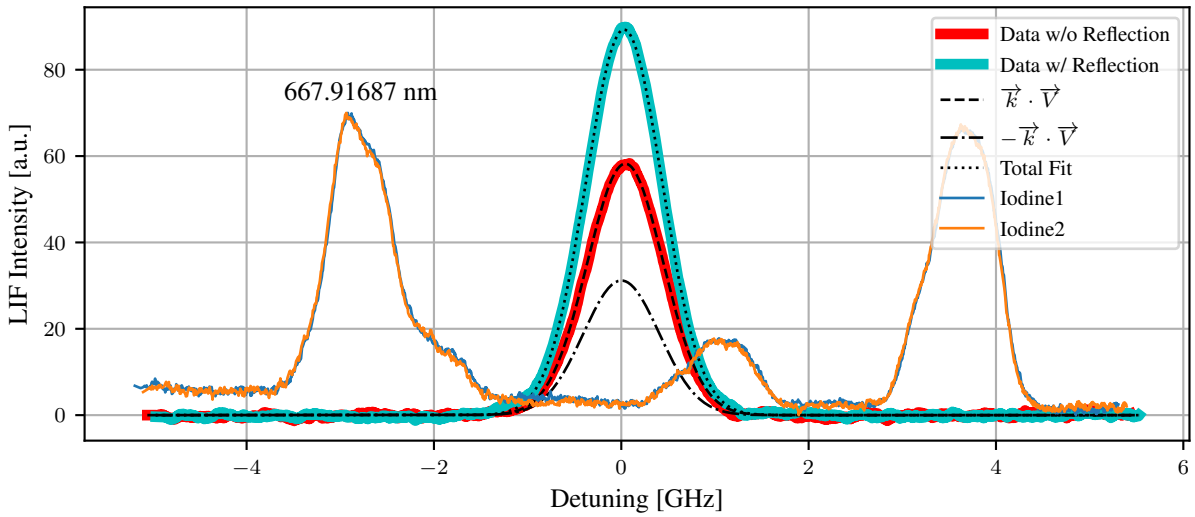


Figure 5.10: The LIF response for both the $\mathbf{k} \cdot \mathbf{V}$ and $-\mathbf{k} \cdot \mathbf{V}$ terms. To find the $-\mathbf{k} \cdot \mathbf{V}$ term, the $\mathbf{k} \cdot \mathbf{V}$ had to be subtracted from the signal containing both components. In this way the iodine reference wavelength could be refined such that the speeds for both components were equal in magnitude, but opposite in sign.

be subtracted from the combined signal, and the iodine reference wavelength could be adjusted to again yield a consistent speed.

Figure 5.10 shows the LIF curves with and without the reflected laser component. The $-\mathbf{k} \cdot \mathbf{V}$ component, shown in the dot-dashed line style, was found by subtracting the $\mathbf{k} \cdot \mathbf{V}$ component found without reflection, the red curve, from the combined signal, the teal curve. Due to low flow velocities less than 10 m/s, this measurement was very sensitive to small perturbations like temperature and plasma activity. To gain greater confidence in the iodine reference wavelength, this measurement was made 8 times, with the results shown in Figure 5.11. An average value of 667.91687 nm $\pm$ $1.6 \times 10^{-5}$ nm was found to be the appropriate wavelength and the location is indicated by right frame of the figure. The uncertainty in the reference wavelength yields an absolute velocity uncertainty of 7.2 m/s.

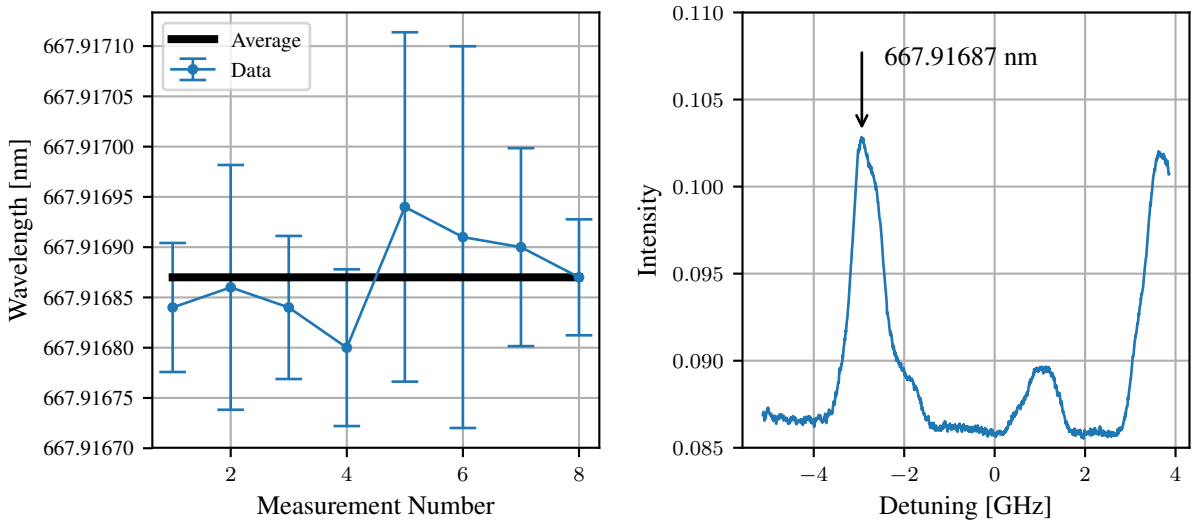


Figure 5.11: The wavelength for the prominent molecular iodine peak used for calibrating the neutral argon LIF measurements was found to be 667.91687 nm $\pm$ $1.6 \times 10^{-5}$ nm.

### 5.2.1.3 Curve Fitting

Once the frequency scale is re-linearized and calibrated, the LIF signal can be analyzed. Figure 5.12 shows a typical set of raw data captured by the PMT for both the $\sigma^+$ and $\sigma^-$ polarizations along with the molecular iodine and etalon signals. The $\sigma^+$ curve in Figure 5.12a is shown in blue while the $\sigma^-$ is shown in red.

Although the LIF signal *can* be fit by a simple Gaussian function of the form:

$$I(f') = A \exp\left[\frac{-c(f' - v_f f_0)^2}{f_0^2 v_{th}^2}\right] \tag{5.1}$$

each $\sigma^+$ and $\sigma^-$ LIF profile is not strictly a pure Gaussian function, as discussed in Section 2.3. Since the magnetic field strength is not large in this work, the spacing of the individual Zeeman lines is much closer together than the broadening due to the Doppler effect and the thermal velocities. Therefore the six individual Voigt profiles merge into a single broad peak. The green curve in Figure 5.13 shows the slight additional broadening from convolving a Gaussian distribution (blue) with the Zeeman lines. In this case, fitting the LIF profile with a pure Gaussian leads to a 10%

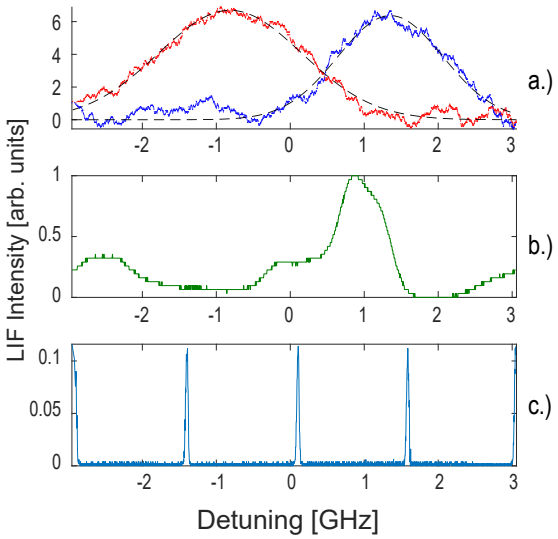


Figure 5.12: Collection of raw data obtained during a typical frequency scan. The profiles for the $\sigma^+$ and $\sigma^-$ lines are shown in a.), while the emission profile from the iodine reference cell is shown in b.). The etalon transmisison peaks, spaced at regular 1.5 GHz intervals, are shown in c.). The data shown here have been corrected for non-linearities in the laser tuning.

overestimate of the ion temperature. This 10% difference in the ion temperature is due to the correction for the additional broadening introduced by the Zeeman lines and predicted by Edrich in his thesis [64]. Figure 5.14 shows the ion temperatures measured along the magnetic axis as the ions are accelerated towards a boundary plate. Both curves show the temperature increasing as the ions get closer to the plasma boundary followed by a dropoff. However, red points show the extent to which fitting the curves with a pure Gaussian curve overestimates the ion temperature. The fitting process followed a typical least-squares algorithm using the center frequency $\nu_0$ and the ion temperature $T_i$ as the fitting parameters.

Due to the differing intensities of the individual Zeeman lines, the least squares fitting places the fit of the Gaussian curve and the convoluted curve at slightly different locations. The disagreement in peak location is typically on the order of 5 MHz in this device. This yields a velocity disagreement of 4 m/s. To reiterate, due to the mirror symmetry of the $\sigma^+$ and $\sigma^-$ lines, the Doppler shifted

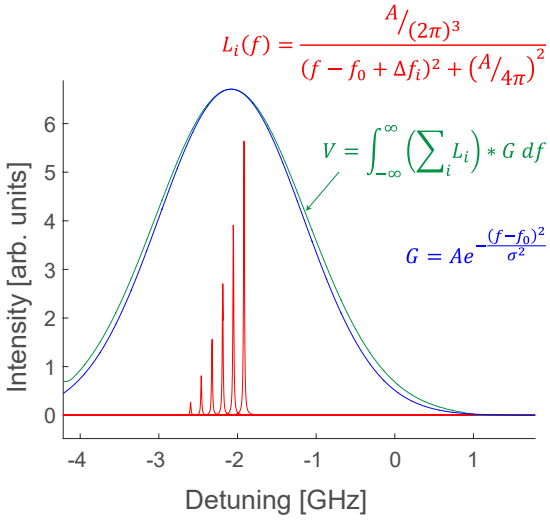


Figure 5.13: While the Gaussian shape due to Doppler broadening (blue) is the dominant contributor to the LIF profile, the actual profile is a convolution of the natural width of the Zeeman lines (red), Doppler broadening, and the width of the laser (not included), among other possible broadening effects. The profile shown here (green) is only a convolution of the Zeeman lines and Doppler broadening. The effect of assuming a pure Gaussian distribution on measured ion temperatures is evident.

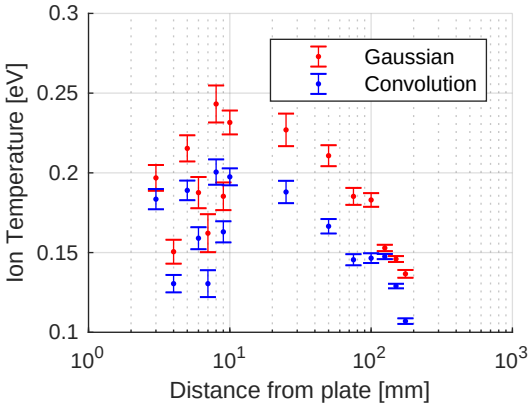


Figure 5.14: Fitting the LIF signal with either a pure Gaussian curve (red points) or a convolved curve (blue points) yield the same general trend. However fitting with a pure Guassian curve overestimates the ion temperature by approximately 10%.

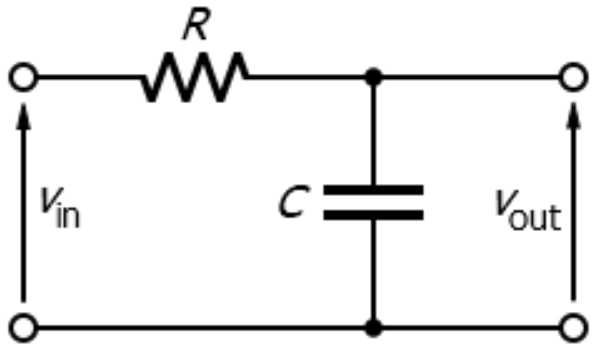


Figure 5.15: Simple RC filter schematic. Source: Inductiveload / Wikimedia Commons / Public Domain.

center frequency found using the midpoint method described in Section 4 will be unaffected by this slight shift in the fitting process, even when fitting with a pure Gaussian. However, this is only strictly true if underlying VDF is symmetrical, like a Maxwellian distribution. For other devices with higher magnetic fields or non-Maxwellian VDFs, this effect becomes more pronounced and fitting with a pure Gaussian function is no longer accurate. The first moment of the LIF signal, $\langle \nu \rangle = \int \nu \mathrm{LIF}(\nu)\, d\nu$, will still yield the Doppler shift, $\Delta\nu$, and $\langle V \rangle$ can still be determined from $\langle V \rangle = \frac{c}{\nu_0}\langle \Delta\nu \rangle$, even when non-symmetric VDFs are measured in stronger magnetic fields. Eliminating the need to worry about the magnetic field strength and how it affects the fit is the primary benefit of using the midpoint between the two Zeeman groupings.

Irrespective of the underlying shape of the LIF response, the lock-in filter introduces another asymmetry as a result of a first order low pass filter used in the output stage of the device. Increasing the time constant of the low pass filter results in smoother data, but at the expense of an asymmetric distortion and a time shift. Both of these effects are particularly troublesome because the output of the lock-in amplifier is compared with data not affected by a time shift to determine the flow velocity. It is thus important to accurately account for the effects of the low pass filter used in the lock-in amplifier.

A simple resistor-capacitor (RC) low pass filter is shown in Figure 5.15. The series resistor is labeled 'R' and the parallel capacitor is labeled 'C'. The output voltage will be the input voltage minus the voltage drop through the resistor,

$$V_{out} = V_{in} - IR, \tag{5.2}$$

where $I$ is the current flowing through the resistor with resistance $R$. The current flowing through the capacitor is proportional to the time derivative of the voltage across it,

$$I = C\frac{dV}{dt}. \tag{5.3}$$

Combining these two equations yields

$$V_{out} = V_{in} - RC\frac{dV}{dt}. \tag{5.4}$$

Discretizing the derivative as $\frac{dV}{dt} = \frac{\Delta V}{\Delta T}$, and exchanging variables $S_{out,i} = V_{out,i}$ and $S_{in,i} = V_{in,i}$, gives a recurrence relation that can be used to simulate the output of the filter for a given input. $\Delta T$ here is the time interval used by the digitizer when acquiring LIF data, and $S_i$ is the measured signal at each point.

$$S_{out,i} = \alpha S_{in,i} + (1-\alpha)S_{out,i-1} \quad \alpha = \frac{\Delta_T}{RC + \Delta_T}. \tag{5.5}$$

The value of $\Delta_T$ is determined by total sweep time (typically 100 s) divided by the number of data points acquired (2500 here), and $RC$ is the time constant of the filter. Figure 5.16 shows the effects of increasing the lock-in amplifier's low pass filter time constant. The same LIF measurement was performed multiple times, changing only the time constant of the filter. The total sweep time of the laser was 100 s in all cases. For longer filter time constants, the effect of the filter is to lower the amplitude of the LIF response, shift it towards lower frequencies, and severely distort the shape. However, as indicated by the black fitted curves, the effect was able to be accurately reproduced by Equation 5.5.

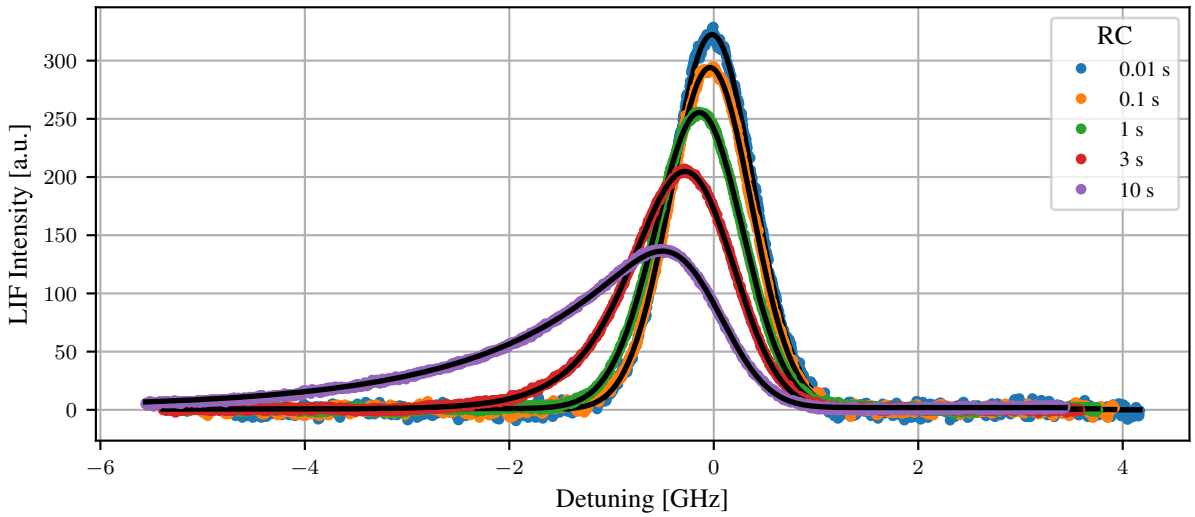


Figure 5.16: The effects of the lock-in filter low pass filter is easily seen by acquiring LIF data at the same position and under the same conditions, changing only time constant. The fit to the data in each case, black curve, demonstrates that the effects of the low pass filter can be accurately accounted for.

## 5.3 Passive Spectroscopic System

Spectroscopy is an extremely valuable tool in plasma physics. Thanks to the temperatures involved, nearly all plasmas emit radiation due to electron impact excitation. Exactly which atomic levels get excited and to what degree depends on the density and energy distribution of the electrons. As a result, all of the information concerning the state of the plasma is encoded in the spectral emission. A spectrometer is the tool used to access this information.

The workhorse spectrometer used on MARIA is a 500 mm Czerny-Turner grating spectrometer manufactured by Princeton Instruments. The spectrometer has a turret with three gratings that can be selected to produce spectra with varying degrees of resolution. The highest resolution spectra are acquired using a 1800 groove/mm holographic grating blazed at 500 nm giving a resolving power of 7100. Two lower resolution 1200 groove/mm gratings with a resolving power of 5700

are available: one blazed at 500 nm, and one blazed at 300 nm. The detector is a PIXIS 256E CCD camera from Princeton Instruments, a back-illuminated open electrode camera that can be thermoelectrically cooled down to -70 $\deg$ C. It features a quantum efficiency of $>$20% from 250 nm up to 950 nm. The dispersed light from the grating can also be directed to an exit slit where any kind of detector may be mounted. In this work, a PMM-01 photomultiplier tube from Thor Labs was typically mounted there.

The spectrometer wavelength was calibrated using the Princeton Instruments IntelliCal system and by a OL-455 NIST traceable integrating sphere irradiance standard from Optronic Laboratories. The IntelliCal system comes with mercury vapor and an Ar/Ne plasma sources integrated into one unit. Emission lines from these sources were compared with reference spectra from Princeton Instruments to calibrate the wavelength in air at standard temperature and pressure. The wavelength calibration was an automated routine developed by Princeton Instruments. The intensity calibration procedure was developed in-house using a MATLAB API interface for the Princeton Instruments Lightfield software used to control the spectrometer. The intensity calibration procedure is thoroughly explained in Appendix A.

## 5.4 RF Compensated Langmuir Probe

The distortion introduced in the I-V curves of swept Langmuir probes by radiofrequency heating can lead to an overestimate of the measured electron temperature. RF compensation of the probe tip is one method for removing the effect of the time varying plasma potential and is well described by I.D. Sudit and F. F. Chen [54, 68]. The basic idea is to decouple the tip of the Langmuir probe from the rest of the circuitry at RF frequencies through the use of RF chokes. A large 'compensation' electrode placed near the probe tip is used to collect sufficient electrons to drive the probe tip at the RF frequency and follow the oscillating plasma potential. The compensation electrode is coupled to the probe tip through a small capacitor such that it appears to be a direct short

at the RF frequencies of interest, but does not allow a DC current to flow to the measurement electronics. RF compensation has been used on multiple helicon experiments by several researchers with acceptable results [69, 70, 71].

A CAD model of the probe construction is shown in Figure 5.17. The body of the probe is a 6 mm diameter 316 stainless steel tube. A 6 cm length of alumina ceramic tubing makes up the tip of the probe body and is exposed to high density plasmas. The probe tip is constructed from a 0.5 mm diameter tungsten rod and is inserted into bores of the alumina rod. The tungsten tip is crimped to wires using a thin stainless steel tube. The compensation electrode is made up of a 6 mm wide .01 mm thick tantalum foil wrapped around the tip of the alumina rod. A thin strip of tantalum is passed through one of the remaining bores in the alumina rod and connected to one side of a 1.5 nF capacitor. The other side of the capacitor is soldered to the wire connecting to the tungsten tip. Two inductive chokes, with resonant frequencies of 13.5 Mhz and 27 Mhz, are connected to the capacitor-tip junction. The signal wire from the inductors is passed down the stainless steel probe body, out through a vacuum tight BNC feed through, and to the probe electronics via coax cable.

The probe sensing circuitry is a simple circuit built around two operational amplifiers (OP-AMP). A schematic of the circuit is shown in Figure 5.18. The circuit works by biasing the probe tip, shown on the right side of the figure, with a 100 V programmable power supply, shown on the left side. The current collected by the probe is measured by the AD629 OP-AMP from the voltage drop across the 10 $\Omega$ resistor. The real probe voltage is monitored by the voltage drop across the 1 $M\Omega$ resistor which is part of a 10x voltage divider.

Despite a careful attempt to apply the principles of RF compensation to the probe construction, it is unfortunately not possible for the probe to be perfectly compensated under all conditions. As the density changes, the sheath thickness and capacitance can change the properties of the effective probe circuit and degrade the effectiveness of the RF compensation. Measuring the I-V

Figure 5.17: Single tip Langmuir probe sensing circuity as implemented at MARIA.

curve below the floating potential, where RF oscillations have a minimal impact, has been shown to be the best practice for extracting electron temperature measurements [18].

If an accurate I-V curve can be obtained from the Langmuir probe, it has been shown that the first and second derivatives $\left(\frac{dI}{dV}, \frac{d^2I}{dV^2}\right)$ are proportional to the electron energy distribution function (EEDF) [51, 72, 39]. This approach has yielded acceptable results when applied to other helicon devices and is used when evaluating electron temperatures on MARIA in some cases [69]. Figure 5.19 shows a typical semi-logrithmic plot of the I-V curve, and the electron energy probability function (EEPF) evaluated using the second derivative method [73]. The deviation from linearity below Te (1.4 eV) in the EEPF is a result of the mathematical approach used and is not physical. The deviation from linear between Te and $\sim$5 eV is believed to be due to still insufficient RF compensation. The deviation in the EEPF is the same as that in the I-V curve between 45-50 volts.

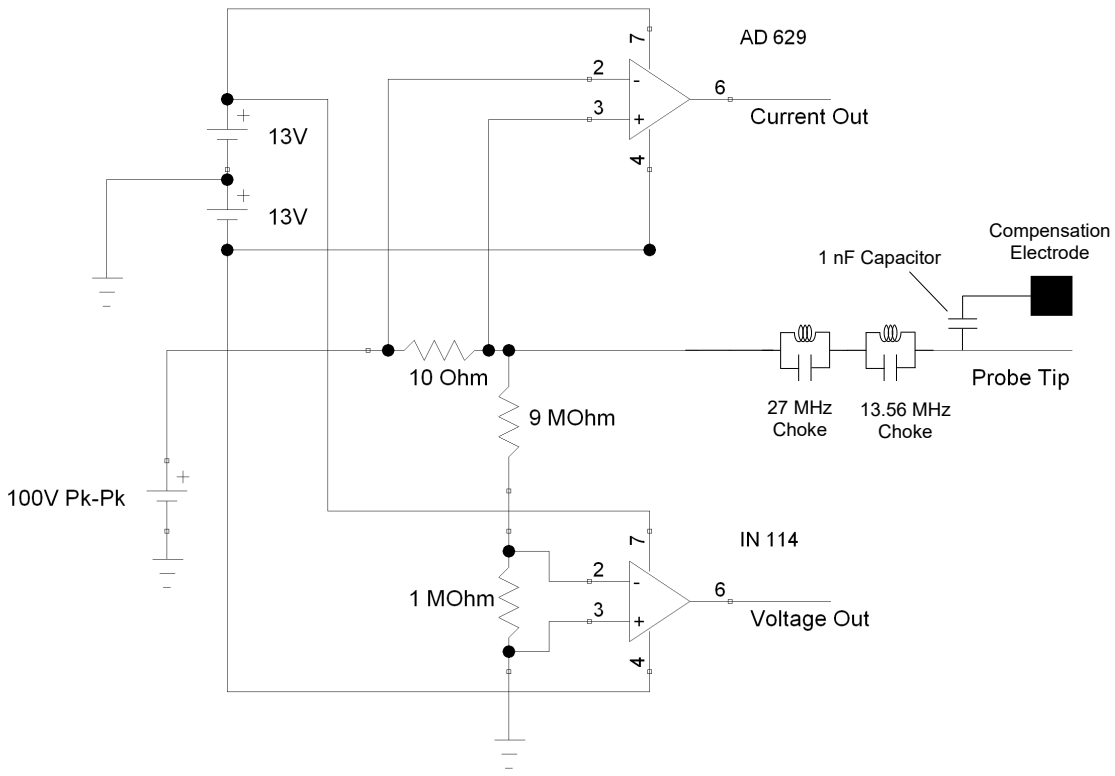


Figure 5.18: Single tip Langmuir probe sensing circuity.

An important consideration to keep in mind is the effective dynamic range of the plasma density. The size of shunt resister for the Langmuir probe and the size of the probe tips must be carefully chosen to be durable when measuring high density plasmas without causing excessive disruption to the plasma. The small probe size and low shunt resistance, 15 $\Omega$, establish a lower limit beyond which insufficient current is drawn for reliable fitting. The lowest density able to be measured in this work was about $1 \times 10^{16}$ m$^{-3}$.

This current version of the RF compensated single Langmuir probe has yielded the best results to date on MARIA plasmas. Achieving ideal RF compensation is an art form, as evidenced by

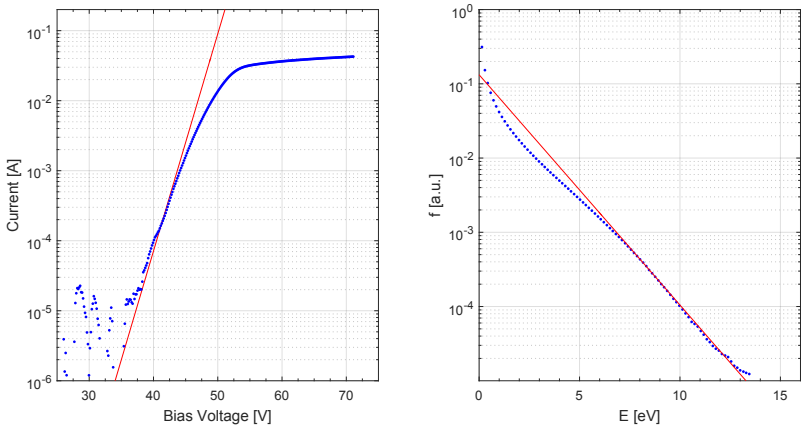


Figure 5.19: Taking the second derivative of the I-V curve yields a curve that is proportional to the electron energy probability function (EEPF). This technique has been used to evaluate the electron temperatures presented in this paper. The temperature measured here is 1.4 eV. The data is shown with blue dots while theoretical curves for 1.4 eV are shown with red lines.

Chen's discussion on the subject with respect to helicon discharges [54]. As discussed above RF oscillations of the Langmuir probe IV curve appear as a shallower slope when plotted logrithmically. While this probe is a dramatic improvement over an uncompensated probe, some oscillation is still believed to occur closer to the electron saturation region. The effects of this oscillation is seen as the deviation from the linear slope, indicated by the red line, between bias voltages of 45 V and 55V in the left panel of Figure 5.19. While there is still room for improvement, this probe is used as the primary benchmark for electron temperatures and densities measured on MARIA.

# Chapter 6

# Results

## 6.1 Operational Parameter Space in Helicon Plasmas

As mentioned in Section 5.1 MARIA represents a significant upgrade from Dr. Siddiqui's recent PhD work [74]. Not all of the infrastructure upgrades occured at the same time and elements of it, such as the RF system, evolved during the course of this research. Even during the writing of this thesis, MARIA was receiving cooling system upgrades to extend CW operation up to 10 kW. Understanding the operational range of parameters where the helicon mode appeared to propagate was vital in the development of such a repeatable and stable device, and revealed the ideal conditions under which the particle and momentum balance measurements, explained in Section 6.3, should be made.

The first set of obvious measurements to acquire were the range of electron temperatures and densities that could be achieved and with what parameters. To accomplish this, a systematic set of Langmuir probe measurements were made at a range of magnetic field strengths, RF heating powers, and neutral gas pressures. The RF power was varied from 100 W to 1000 W, magnetic field strength varied from 200 G to 800 G, and pressure varied from 1.4 mTorr to 2.4 mTorr. The parameters were maintained in a region where MARIA could be operated for up to 10 minutes. Higher RF power could be used, but until early 2019, cooling capacity limited the duration of the plasma to a few seconds. In all cases the probe measurements were made on axis 800 mm

downstream of the antenna, about mid length between the antenna and the downstream boundary plate.

The abrupt jump into the helicon mode can be seen in Figure 6.1 by the factor of two to three increase in electron density followed by a steeper $n_e/B$ slope. In these measurements, taken on axis, the RF power is indicated by the different curves and magnetic field strength is indicated along the horizontal axis. An inverse relationship between the power and magnetic field strength required to propagate a helicon wave is evident. At very low RF power, 100-200W, before the helicon wave can propagate, power is capacitively coupled to the plasma which only exists very close to the antenna and an insufficient current is collected by the Langmuir probe for reliable fitting [75]. At higher RF power, 300-400 W, and moderate magnetic field strength, 200-500G, power is inductively coupled to the plasma and the magnetic field is able to confine the electrons enough for them to propagate downstream of the antenna and be measured by the Langmuir probe. However, the very low current collected still prevents reliable fitting. As the RF power increases, a more intense plasma is created and more of the low energy bulk electrons are able to propagate away from the antenna and be measured. Finally at higher RF power and magnetic field strength a sufficient electron density for the helicon wave to propagate is reached and ionization takes place down stream of the antenna. At this stage significant quantities of electrons are being produced closer to the Langmuir probe and a high density low temperature plasma is measured.

The increasing electron density with increasing magnetic field strength shown in Figure 6.1a is truly a remarkable characteristic. For each trace shown in the figure, the RF power was held constant during the magnetic field scan. In the case of the 700 W scan, the electron density increased from $4 \times 10^{17}$ m$^{-3}$ at 200 G to $4.36 \times 10^{18}$ m$^{-3}$ simply by increasing the magnetic field strength. That's over an order of magnitude increase in electron density, with no increase in applied RF power! In all cases the reflected power was less than 10 W, indicating very efficient RF coupling to the plasma. Glancing back at the 0D power balance, a 700 W plasma with 10 eV electrons

(a)

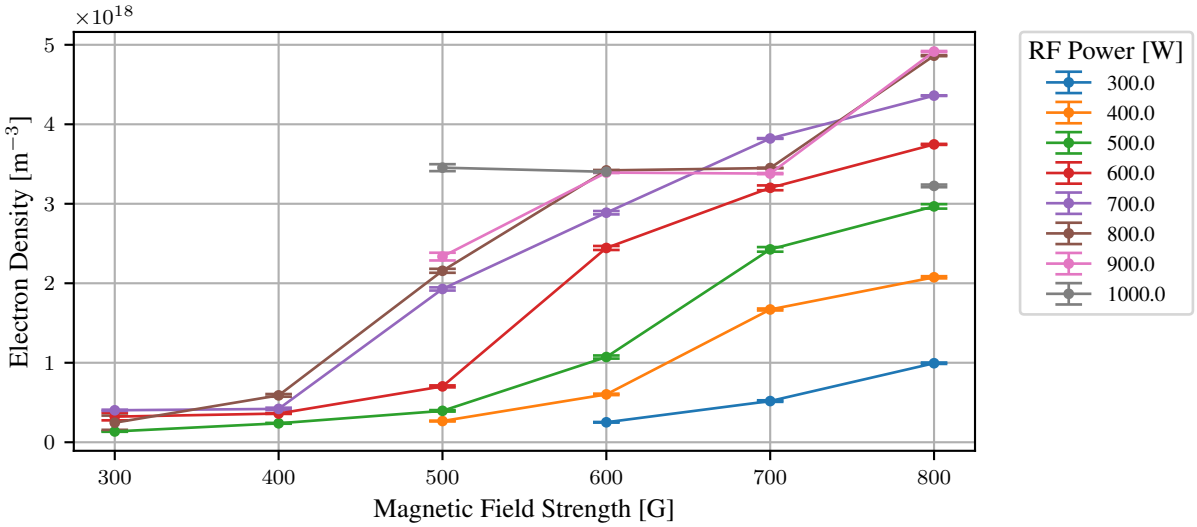


(b)

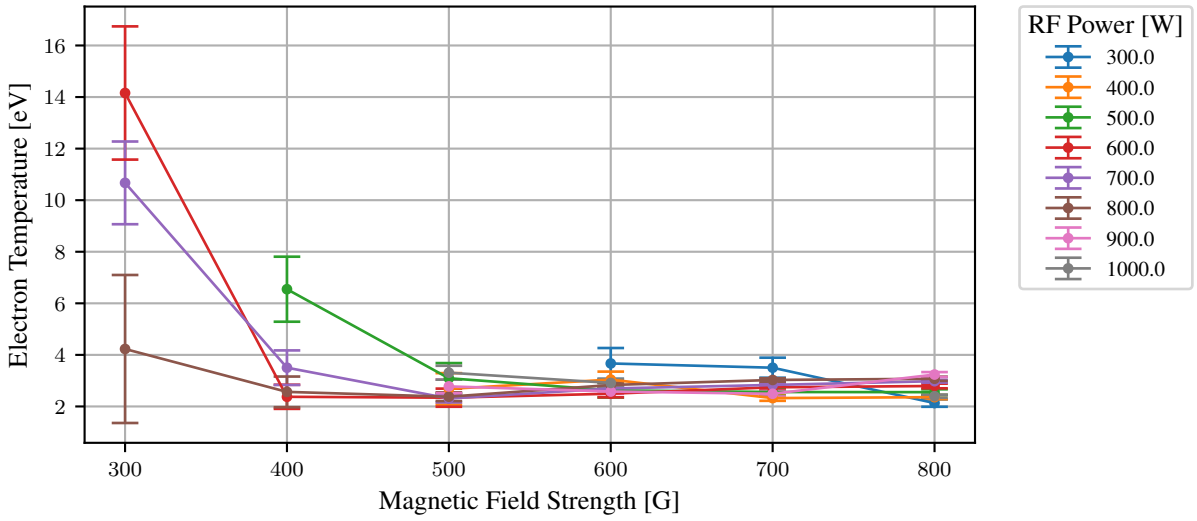


Figure 6.1: The electron density and temperature range of operation for MARIA plasmas. The jump into the helicon mode is evident by the factor of three increase in electron density, e.g. between 500 G and 600 G at 600W. Ion saturation currents below 0.5 mA, corresponding to an electron denisty of $10^{17}$ m$^{-3}$ could not be fit reliably and are not shown.

yields a density of $4 \times 10^{17}$ which agrees very well with the measurement at 300 G. The same power plasma with an electron temperature of 3.0 eV yields an electron density of $9.5 \times 10^{18}$ m$^{-3}$, roughly a factor of two higher than the measurement at 800 G. However, between 400 G and 800 G the electron temperature only drops from 3.5 eV to 3.0 eV. The order of magnitude increase in electron density over the same range is the effect of the helicon wave increasing the ionization rate dramatically. The ionization mechanism itself is not discovered, but the real ionization rate increase is measured and presented in this work.

The plasma was typically not in the helicon mode below 450 G, and was a reliable high density helicon plasma above 700 G. As laser induced fluorescence of argon ions will be used throughout this work to investigate the flux of ions in the plasma, a sufficient density of ions must be present. The threshold for the argon ion LIF scheme used was about $1 \times 10^{18}$ m$^{-3}$. As seen in Figure 6.1a, the transition into the helicon mode occured fairly reliably at 450 G for an RF power of 700 W. At this power the plasma could run for up to 20 minutes, and could reach densities in the range of $5 \times 10^{18}$ m$^{-3}$ with sufficient range to establish decent scaling of densities, particle fluxes, etc. with magnetic field strength. For these reasons, this work focuses on magnetic field strengths in the range of 450-900 G, with a fixed RF power of 700 W.

Curiously a limit appears to be reached in Figure 6.1a. At RF powers beyond 700 W, no further increase in electron density is measured. This suggests some kind of saturation exists where sufficient RF power is available to increase the ionization rate, but some other factor becomes limiting. One possibility is the ion fraction on axis is already very high and insufficient neutral particles are able to reach the axis to increase the density. If this is true, a sort of radial flat-top electron density profile is expected. In this case, further increases in RF power would increase the radial extent over which a high ion fraction extends without further increases to the electron density on axis. Another possibility is that sufficient power is available to meet the ionization rate required to generate the appropriate electron density to satisfy the dispersion relation.

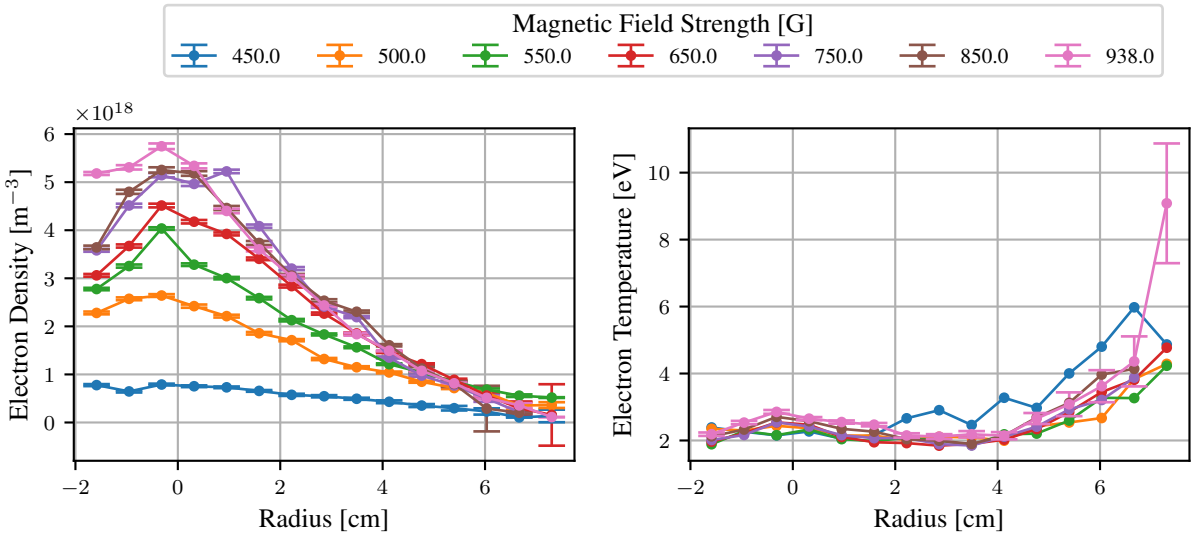


Figure 6.2: Radial variation of electron temperature and density for various magnetic field strengths. Typical electron temperature uncertainties are indicated by the 938 G trace.

If it is true that not enough neutral particles are available on axis to sustain higher electron densities, varying the neutral fill pressure might have some effect. To investigate this, Langmuir probe measurements were taken on axis at 700 W and 700 G for various fill pressures. The electron density shown in Figure 6.3a appears to peak just above 2 mTorr. At lower fill pressures insufficient neutral particles may be present to sustain the high ionization rate and electron density. Above this optimal point, excessive electron-neutral collisions likely lead to the cooler electron temperatures seen in Figure 6.3b. The lower electron temperatures are likely an indication that the ionization rate is negatively impacted.

The simple parametric exploration and analysis presented here indicates that a sort of Goldilocks combination of neutral pressure, magnetic field strength, and RF power is required to achieve a broad high density helicon mode plasma. As any one of these parameters are adjusted, so too must the others in order to maintain optimal coupling efficiency. The principle goal of this work is to

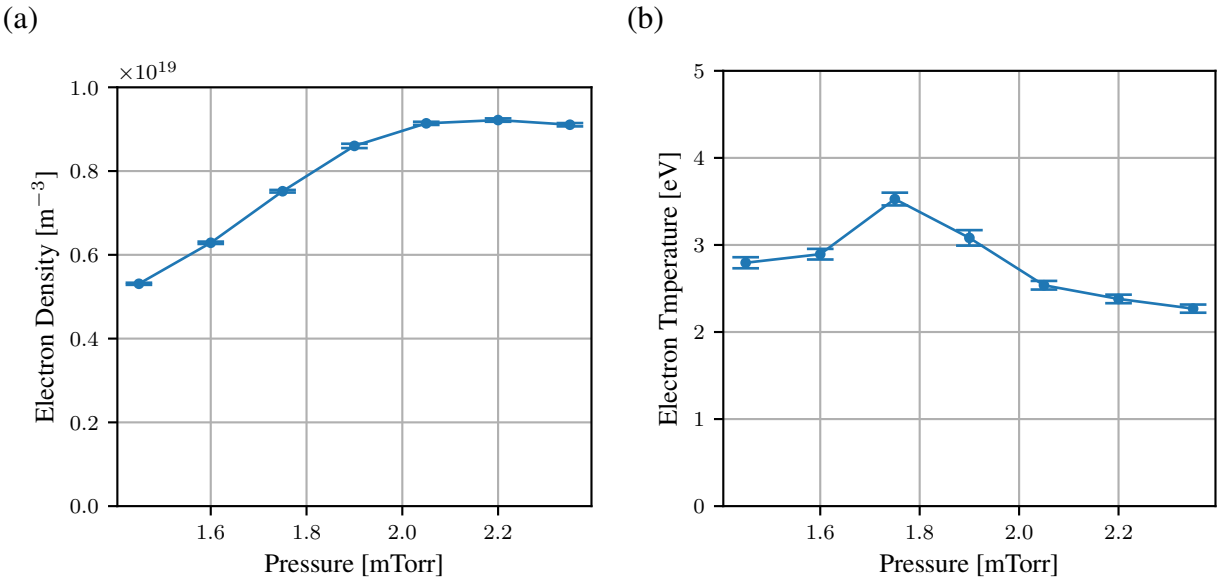


Figure 6.3: To observe how the electron density depends on the gas fill pressure the plasma was operated at different pressures. The peak electron density appears to be at about 2 mTorr for an RF power of 700 W and magnetic field strength of 700 G.

investigate the particle and momentum balance and shed light on the processes that conspire to limit the ultimate electron density.

### 6.1.1 Repeatability

A tremendous amount of work involved in the research presented here was put into ensuring that MARIA is able to create robust and repeatable plasmas. Due to the low cooling capacity installed during much of this research, a 30-40 minute cool-down period was required after every 5-10 minutes of data taking. High quality research could not be performed if identical plasma conditions could not be reliably created each time the plasma was re-lit.

To investigate the reliability of MARIA operation, Langmuir probe measurements were taken every time the plasma was reestablished while acquiring the LIF magnetic field scans presented in the next section. The discharge to discharge variation of electron density and temperature is shown

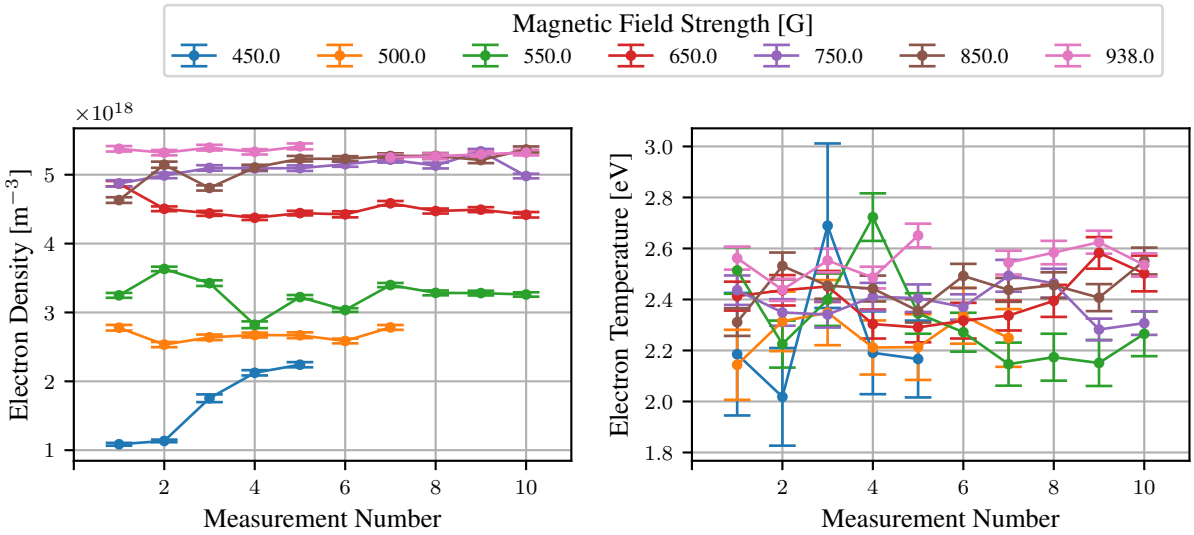


Figure 6.4: During the LIF measurements presented in the next section, Langmuir probe measurements were taken each time the plasma was turned off and on again, to allow cooling.

in Figure 6.4. As discussed above, the plasma made the transition into the helicon mode near 450 G, and could be a bit unstable depending on the condition of the chamber and concentration of lingering impurity gasses such as nitrogen. The electron density increase from 1 to $1.8 \times 10^{18}$ m$^{-3}$ between measurement 2 and 3 at 450 G indicates the plasma made the jump into the helicon mode during these measurements. Above 500 G the helicon mode of operation was reliably reached with standard deviation less than 10% and typically around 5% within a magnetic field set. The electron density data for the 550 G case was especially variable with a standard deviation of 6.7%. The cause of this is unclear.

Another interesting confirmation of MARIA's repeatability was found by taking radial Langmuir probe data before venting the chamber, shortly afterward while the chamber was still conditioning, and 48 hours after the vent when the chamber was again well conditioned. These scans are shown in Figure 6.5. In the data taken shortly after the vent, some water vapor was probably still on the chamber walls and impurity gasses like nitrogen were likely present. The increased

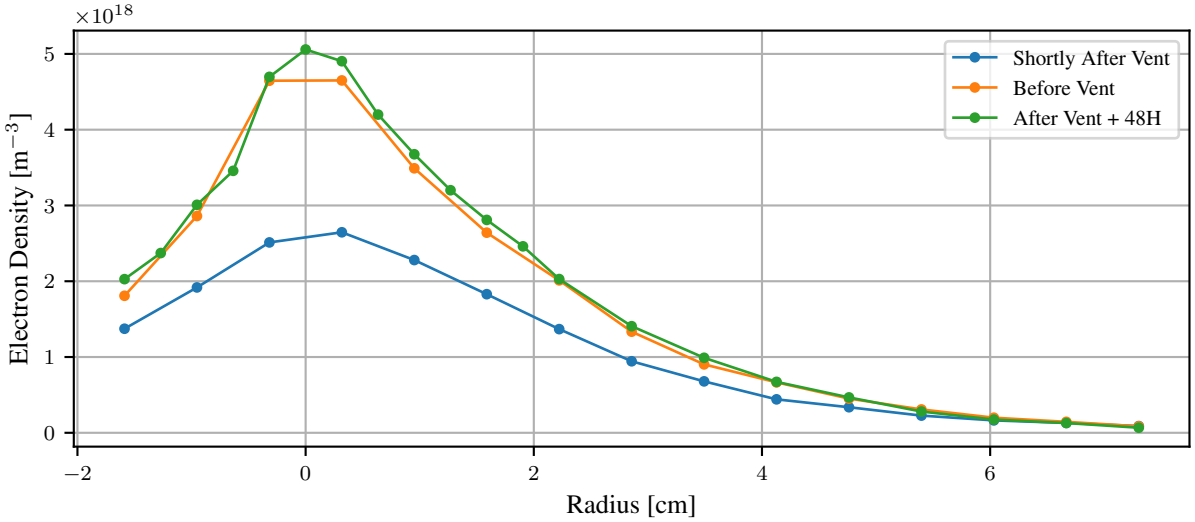


Figure 6.5: Taking Langmuir probe measurements before and after venting the chamber confirmed that plasma conditions could be reliably duplicated. The operating parameters were 700 W of RF power, 700 G magnetic field strength, and 2.0 mTorr neutral pressure in all three cases.

radiation from these impurities limited the performance of the helicon mode and the electron density suffered. However, after 48 hours had elapsed with periodic cleaning discharges and constant vacuum operation the plasma performance recovered fully.

## 6.2 Atomic Population Measurements in Argon Fueled Helicon Plasmas

Applying the line ratio spectroscopic technique to plasma can provide valuable insights into the electron density and temperature of the plasma as well as the relative populations of atomic energy states that would otherwise be difficult to acquire. By rotating the collection optics to acquire light from chords at different radii, and calculating the inverse abel transform, the line ratio spectroscopy algorithm was used to measure the radial variation of various plasma properties. The variation of electron density and temperature as well as the relative population of the ground to 4s $^2$[1/2] 0 level ratio and 4s $^2$[3/2] 2 to 4s $^2$[1/2] 0 level ratio is shown in Figure 6.6. The electron

density exhibits the same profile as the Langmuir probe measurements shown in Figure 6.2, with the highest density on axis and a Gaussian looking profile. However the absolute value differs by a factor of between 3.5 and 7, the Langmuir probe measuring peak electron densities of $5 \times 10^{18}$ $m^{-3}$ (at 750 G and 700W) and the LRS diagnostic reporting a value of $3.5 \times 10^{19}$ $m^{-3}$. The electron temperature matches the Langmuir probe data in Figure 6.2 quite well, even capturing the slight peaking of electron density on axis. The Langmuir probe is located at 1091 mm so is most comparable to the spectroscopic data at 1297 mm. The relative metastable state population ratios are a new measurement that cannot be corroborated at this time.

The poor agreement between electron density determined from the Langmuir probe vs the LRS diagnostic is still an open topic of investigation. While the LRS diagnostic is not yet reliable enough for its intended use, the framework set up to implement it, the spectrometer and analysis tools, can still be used to gain valuable insights into the behavior of the atomic populations. Efforts to identify the possible reason for the poor density agreement are presented in the rest of this section. These investigations include evaluation of the fitting algorithm performance and detailed analysis of the transitions used and the population process for their originating atomic levels.

Using the LRS algorithm to infer plasma parameters while varying the magnetic field, shown in Figure 6.7, appears to show the exact opposite electron density trend compared to Langmuir probe measurements in Figure 6.2 and LIF data in Figure 6.13c. From LIF measurements, the electron density clearly peaks at an axial position between 680 mm and 1100 mm down stream of the antenna. Additionally, as the magnetic field strength is increased, the electron density increases. In Figure 6.7 a peculiar feature that may yield insights into the cause of disagreement is that the shape of the axial electron density profile appears to agree reasonably well with the LIF data below 550 G or so, with a peak electron density near the axial position of 600 mm. Above 550 G, the LRS algorithm yields a density minimum where the LIF measurement find a density maximum. This

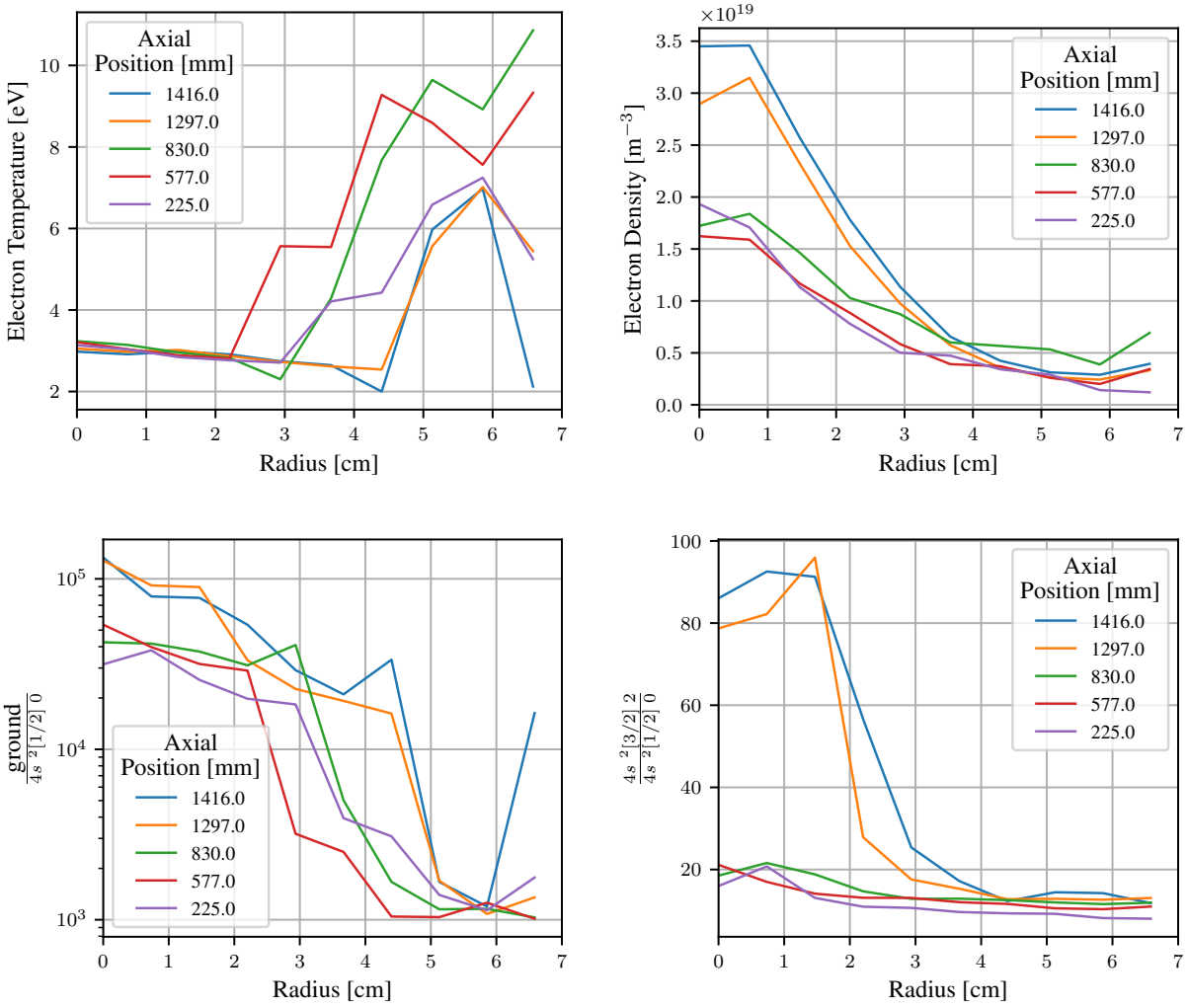


Figure 6.6: The gradient descent line ratio spectroscopy technique is capable of inferring valuable information about the plasma. Here is the electron density is an order of magnitude higher than the Langmuir probe measurements, while the electron temperature is approximately the same. The LRS technique is capable of providing information regarding the metastable state densities.

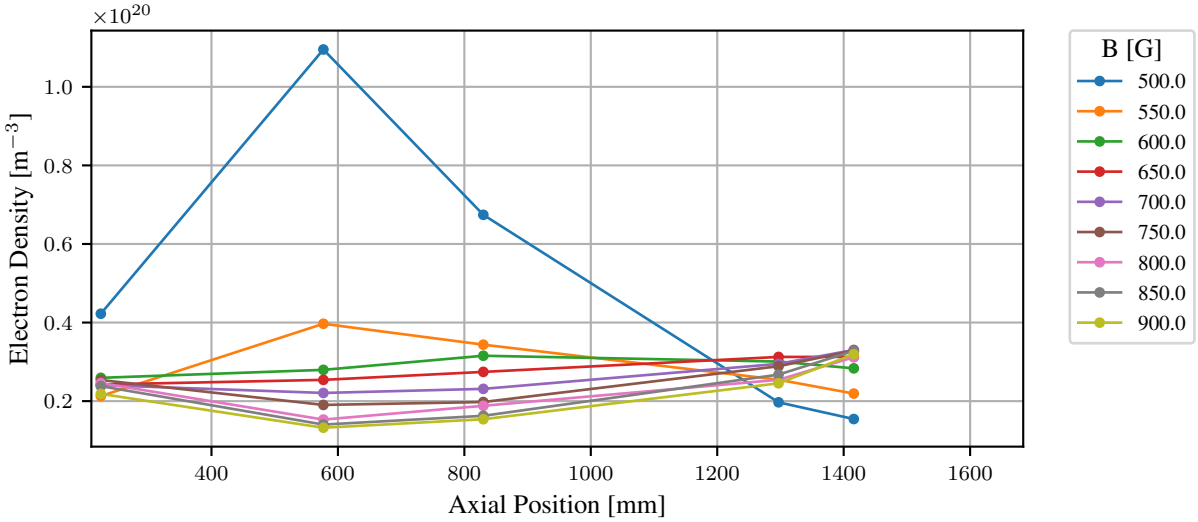


Figure 6.7: A clear scaling with magnetic field strength is visible in the electron density data inferred by the LRS algorithm. Unfortunately the scaling, high and low magnetic field strength and low at high field strength, appears to be the exact opposite of that shown in Figure 6.2.

suggests that at high magnetic field strength, and therefore at high electron density, some atomic process is not being correctly captured by the model.

The poor agreement at high magnetic field strength between the LRS and LIF diagnostics doesn't appear to be an inability of the LRS algorithm to find an optimal fit to the data. Figure 6.8 shows a simulated emission spectrum (blue lines) overlaying an experimental spectrum at 550 G and 900 G. The quality of the fit between the simulated line intensity and the experimental data for both cases at an axial position of 577 mm is very good. Here the inferred density at 550 G is $3.9 \times 10^{19}$ m$^{-3}$, and the inferred density at 900 G is $1.32 \times 10^{19}$ m$^{-3}$, while Langmuir probe densities were $4.0 \times 10^{18}$ m$^{-3}$ and $5.5 \times 10^{18}$ m$^{-3}$ respectively.

In the course of this research, the the particular behavior of the 4p $^2$[1/2] 0 level (level 15) stood out. Figure 6.9 shows the population of level 7, 10, and 15, normalized to the population of level 8, found by the collisional radiative model as a function of electron density, assuming the

(a)

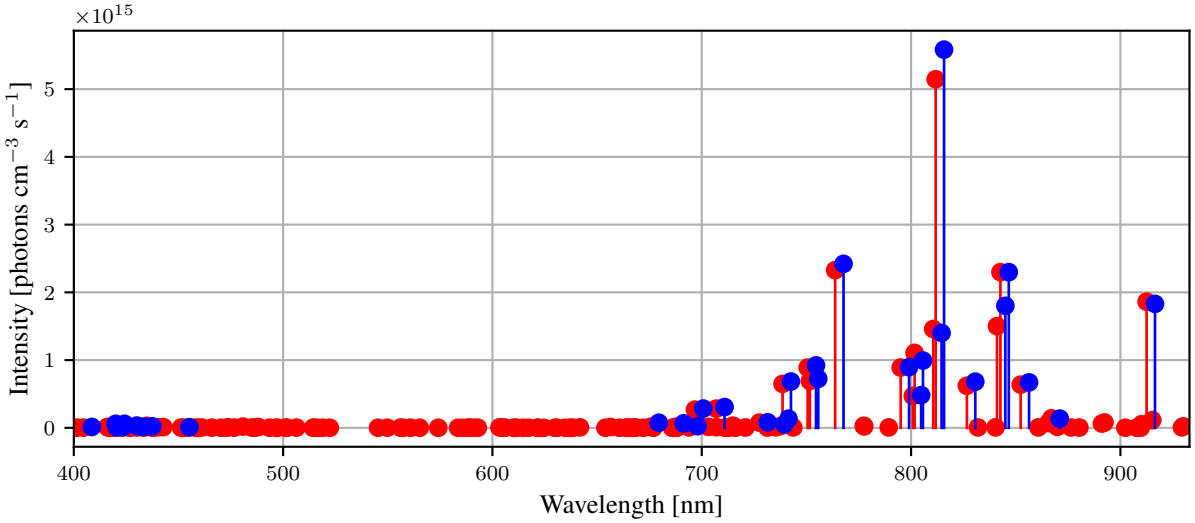


(b)

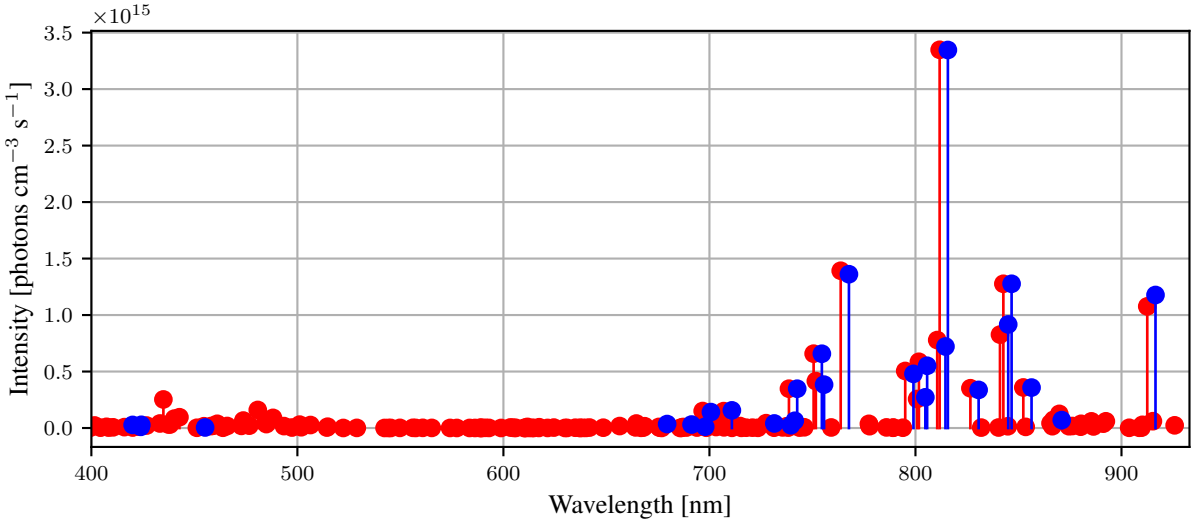


Figure 6.8: The quality of agreement between the best-fit simulated spectrum, blue, and the experimental spectrum, red, at a.) 550 G, and b.) 900 G. The simulated spectra are offset 4nm to aid comparison. Plasma parameters for the 550 G case were $T_e = 2.99$ eV, $n_e = 3.97 \times 10^{19}$ m$^{-3}$, $g = 1.09 \times 10^5$, $m = 43.8$. Plasma parameters for the 900 G case were $T_e = 3.92$ eV, $n_e = 1.32 \times 10^{19}$ m$^{-3}$, $g = 1.69 \times 10^5$, $m = 15.7$

plasma is in equilibrium. A typical measured population ratio is shown by the dashed horizontal lines. The level ratio trend vs density for level 15, low at high density and high at low density, is particularly interesting because it seems to disagree with measurements. Figure 6.10 shows the population density for level 15, normalized to level 8, as a function of axial position. The slight rise in the population of level 15 between 600 and 800 mm would suggest a lower density here, but in fact the LIF data indicates the opposite. Level 15 is predominantly populated both directly and via radiative cascade from excitation out of the ground state. At equilibrium the population rate of level 15 with respect to level 8 is relatively insensitive to electron temperature. The only conclusion then is that an increase in the population of level 15 with respect to level 8 is due to changing metastable fractions. While a match can be found using the LRS algorithm, the photoemissivity coefficients sourced from the collisional radiative model seem to consistently over predict the population density of level 15, especially at densities that agree with Langmuir probe measurements.

An obvious response to the possible discrepancy in behavior of the 4p $^2$[1/2] 0 level is to simply not use it in the LRS algorithm. However, the 750 nm emission line that originates on that level is a good monitor of the ground state population because it is populated by direct excitation out of the ground state as well as step-wise excitation from the 4s $^2$[1/2] 1 level (which is also populated from ground state excitation). So, the 750 line and the population of the 4p $^2$[1/2] 0 level is very important when trying to constrain the ground to metastable state density ratio. Unfortunately none of the other lines easily detectable in the visible range of the spectrum are similarly populated by direct excitation from the ground state. In future work, refining the population mechanisms for this level will be very important.

Some important population mechanism at high density appears to be missing from the collisional radiative model. Recombination would be an obvious first choice. However, including ionization and radiative recombination using the Exchange Classical Impact Parameter (ECIP)

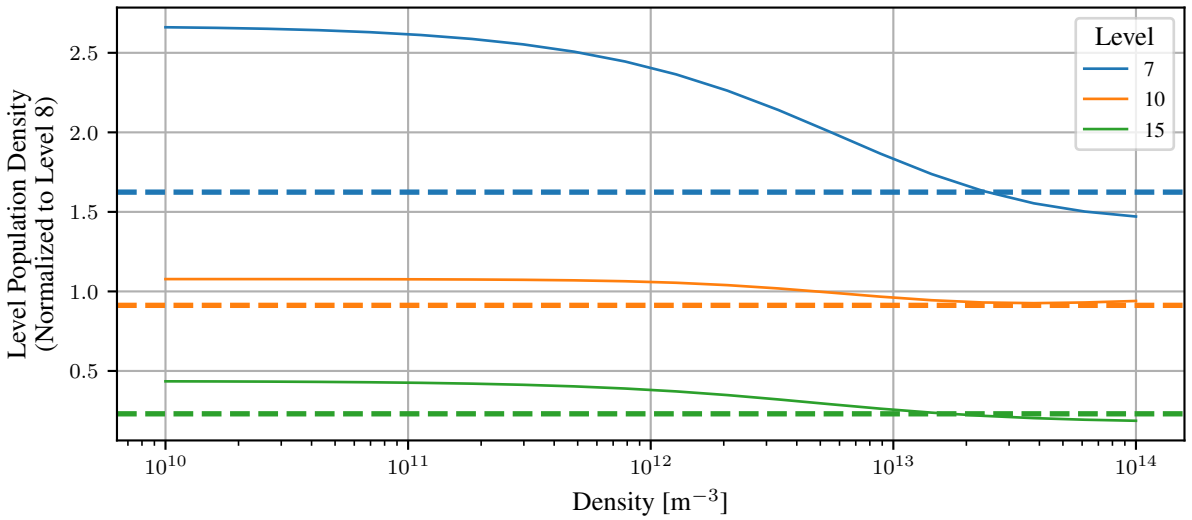


Figure 6.9: The population density of levels 7, 10, and 15 normalized to the population density of level 8 as a function electron density is plotted. The data here assume the atomic levels are in equilibrium at 2.58 eV. All three levels are increasingly depopulated with respect to level 8 at high electron densities.

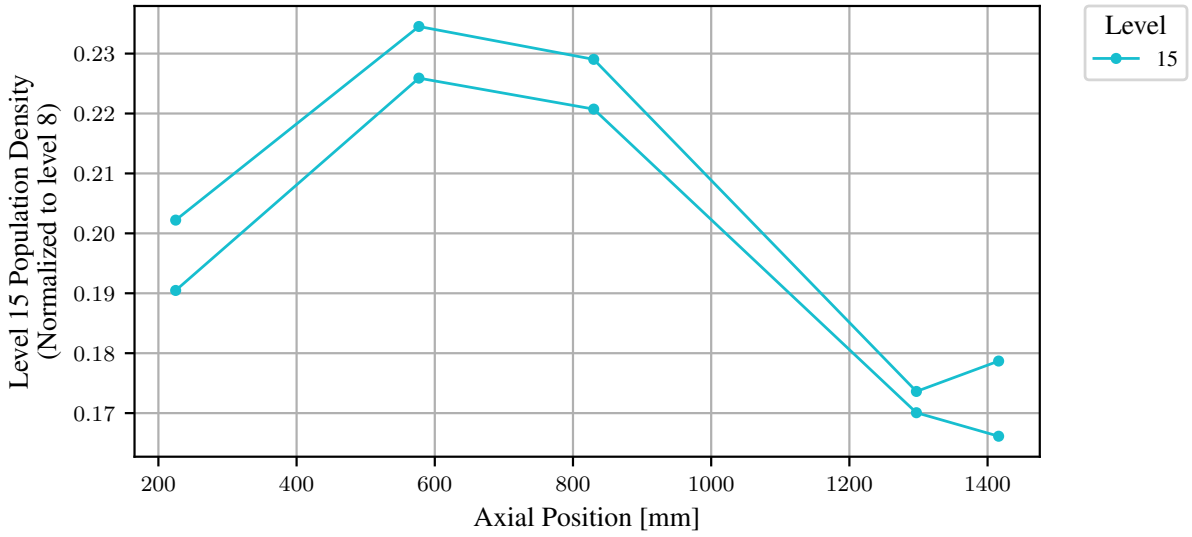


Figure 6.10: The slight rise in the population of level 15 with respect to level 8 seems to follow the trend of electron density.

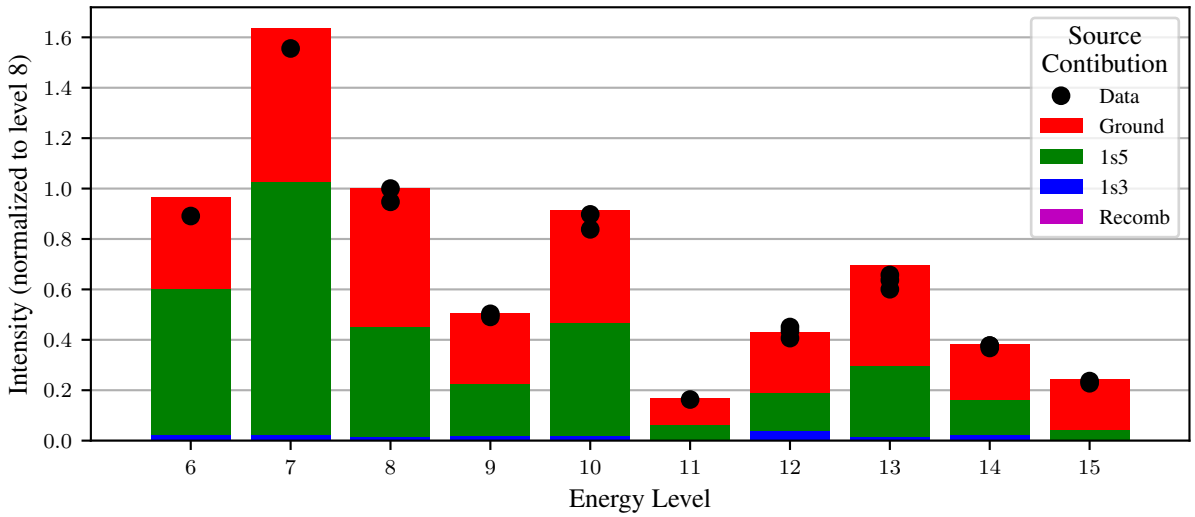


Figure 6.11: Relative contribution to the energy level population from each of the major populating mechanisms. The contributions of electron impact excitation from the ground, 4s $^2$[1/2] 0($1s_3$), and 4s $^2$[3/2] 2($1s_5$) levels are indicated by the red, green, and blue bars respectively. The contribution from radiative recombination would be shown in purple, but the contribution is so low that it is not visible in the figure. The measured relative populations are shown by the black circles.

approximation contributes minimally [76]. The relative contributions from each of the major populating mechanisms for a particular LRS solution is shown in Figure 6.11 for the lower level states of neutral argon. The lack of any visible purple bar clearly shows the negligible contribution from radiative recombination. Excitation out of the ground and 4s $^2$[3/2] 2 level clearly dominate the excitation process from the size of the red and green bars.

## 6.3 Particle and Momentum Balance in Helicon Plasmas

As mentioned previously, a major goal of this work is to gain insight into the particle and momentum balance in a helicon plasma. Significant work has been undertaken to investigate the apparent depletion of neutral atoms on the axis of a helicon device [77, 28, 12, 78]. A few of these researchers have even suggested possible causes of this depletion. However, a complete understanding of the particle and momentum balance in helicon plasmas is missing. In comparing numerically calculated electron temperatures and densities from simulation with experiment, Carter *et al* state,

> The plasma source is a complicated function of electron temperature and density as well as the densities of any neutral species in the device. These quantities are not well known spatially and are very difficult to model [9].

In their paper studying the dynamics of neutral depletion in helicon plasmas, Magee *et al* state,

> The coincident accumulation of neutrals at the edge and Langmuir probe measurements, which show much faster electron dynamics, suggest that this depletion is due not to ionization but to neutral expulsion [12].

Improving the collective scientific understanding of helicon plasmas clearly must address the fundamental mechanisms which lead to the depletion of neutrals on axis and establish the ultimate electron density that can be reached.

Measuring the ion and neutral fluxes which are established by the relevant sources and sinks would yield new information that could provide answers to these questions. In particular the evolution of these particle fluxes are measured as a function of increasing magnetic field strength, which is the primary input for increasing the electron density in helicon plasmas. Navigating the complexity of this topic was aided by simplified mass and momentum conservation equations.

Each of the terms in the conservations equations was investigated by combining experimental information from the LIF system, RF compensated probe, passive spectroscopy, and the collisional radiative model discussed earlier. This section begins with an introduction to the general mass and momentum balance equations and the assumptions used in this work to simplify the model to one dimension. A detailed set of direct LIF measurements of the particle fluxes are then presented and their relationship to the terms in the conservation equations is discussed. Finally a few more LIF measurements are presented which check the validity of the assumptions made in simplifying to the one dimensional case and their implications are discussed.

### 6.3.1 Mass and Momentum Balance Equations and Assumptions

The two basic equations that Carter *et al* simulated and Magee *et al* were considering are the mass and momentum conservation equations, shown in Equations 6.1 and 6.2 respectively.

$$\frac{\partial n}{\partial t} + \nabla \cdot (\mathbf{V}n) = S(\mathbf{x}) \tag{6.1}$$

$$mn\left(\frac{\partial \mathbf{V}}{\partial t} + \mathbf{V} \cdot \nabla \mathbf{V}\right) = \sum \mathbf{F} \tag{6.2}$$

The mass conservation equation equates the temporal buildup of mass in a control volume, $\frac{\partial n}{\partial t}$, and the flow of mass out of the volume, $\nabla \cdot (\mathbf{V}n)$, with the strength of the mass source in the volume, $S(\mathbf{x})$. Here the terms are on a per volume basis, so the mass is represented by a density, $n$. The flow velocity, $\mathbf{V}$, is the first moment of the species velocity distribution function, $\langle V \rangle$. The momentum conservation equation equates the temporal change of momentum, $mn\partial/\partial t(\mathbf{V})$, and the advection of momentum, $mn\mathbf{V} \cdot \nabla \mathbf{V}$, in a control volume to the sum of the forces acting on the material in the control volume, $\sum \mathbf{F}$. Advection is a confusing term but simply refers to the transport of a quantity through a control volume by bulk motion. A leaf moving down a river by floating on top of the water is being advected down the river by moving with the bulk motion of the water.

While Equations 6.1 and 6.2 are complete descriptions, they're much too complex to be used here directly. A few assumptions can simplify things dramatically. First, since the plasma durations and observation times in this work are on the order of minutes and instabilities are not the primary focus here, the steady-state assumption is made – the $\partial/\partial t$ terms go to zero. Second, the plasma is cylindrical, with unit vectors $\hat{r}$, $\hat{z}$, and $\hat{\phi}$, and is assumed to be axisymmetric – any $\partial/\partial\phi$ terms go to zero. Equations 6.1 and 6.2 then simplify to the 2D mass and momentum conservation equations

$$\frac{\partial}{\partial z}(nV_z) + \frac{1}{r}\frac{\partial}{\partial r}(rnV_r) = S(r,z) \tag{6.3}$$

$$mn\left[\left(V_r\frac{\partial V_r}{\partial r} + V_z\frac{\partial V_r}{\partial z} - \frac{V_\phi^2}{r}\right)\hat{r} + \left(V_r\frac{\partial V_\phi}{\partial r} + V_z\frac{\partial V_\phi}{\partial z} + \frac{V_\phi V_r}{r}\right)\hat{\phi} + \left(V_r\frac{\partial V_z}{\partial r} + V_z\frac{\partial V_z}{\partial z}\right)\hat{z}\right] = \sum \mathbf{F}. \tag{6.4}$$

Here the simplified mass conservation implies that material originating in the source region with some radial and axial extent, $S(r,z)$, will leave the volume in which it is created only in the axial and radial directions, $\hat{z}$ and $\hat{r}$ respectively. The flow directions, acounted for by the sign of the velocity, $V$, is particularly important. The axial position of interest, $z$, can be either side of the volume containing the source. If a single source is creating matter, a positive source, the flow of matter will be in the positive direction on one edge of the source volume, and negative on the other. While a negative radial position can be considered, the signs will cancel and only positive radial positions are discussed. As a result, the same positive material source can only create flow in the positive, or radially outward, direction.

The momentum conservation equation is considerably more complex, even after simplifying to 2D, but some intuition can be established in the following way. Consider the leaf floating on the river discussed earlier. The leaf, and the water advecting it along, has some momentum associated with it, $mnV_z$. If all of a sudden a stiff gust of wind blew across perpendicular to the direction of fluid flow (this perpendicular direction is analogous to the radial direction $\hat{r}$), the leaf and the

surface of the water advecting it would gain some perpendicular velocity, $V_r$. Comparing the perpendicular velocity at the leaf's location just after the gust to the perpendicular velocity just before the gust, one would say the leaf's *perpendicular* velocity is not constant along the river's path $\hat{z}$, i.e. $dV_r/dz \neq 0$. The force of the wind in the $\hat{r}$ direction, $F_r$, imparted some velocity to the flow in the perpendicular direction, $V_r$, at a rate proportional to flow of momentum, $mnV_z$; $F_r = mnV_z\frac{dV_r}{dz}$. Each of the terms in the 2D momentum conservation equation are similar: an external force imparts a velocity in the direction of the force's application proportional to the rate fluid momentum is introduced into the domain of the force. A few terms, such as the $V_\phi^2/r$ term come from the definition of del operator in cylindrical coordinates and the chain rule. The full $V_\phi d/d\phi$ term we threw out was $V_\phi\frac{1}{r}\frac{dV_r}{d\phi}$, but $V_r = rV_\phi$, so $V_\phi\frac{1}{r}\frac{d(rV_\phi)}{d\phi} = V_\phi\frac{1}{r}\left(V_\phi + \frac{\cancel{d(V_\phi)}}{\cancel{d\phi}}\right) = \frac{V_\phi^2}{r}$.

Even these equation have far more terms than could possibly be systematically measured in any reasonable amount of time. In open magnetic field line geometries, as is the case in this work, parallel flow speeds are significantly faster than in the direction perpendicular to the field lines. In such cases the parallel thermal and electrical conductivity governs the transport solution and, to first order, radial terms may be neglected. Applying the assumption that radial transport is negligible results in the 1D mass and momentum conservation equations shown in Equations 6.5 and 6.6. These assumptions dramatically reduce the complexity of solving the relevant transport equations and makes experimental measurements tractable. This is the operating assumption in this work, but measurements in the radial direction were also made and are presented to check the validity of the assumptions made.

$$\frac{\partial}{\partial z}(nV_z) = S(z) \tag{6.5}$$

$$mnV_z\frac{\partial V_z}{\partial z} = \sum F_z. \tag{6.6}$$

To make Equation 6.6 a bit more useful, the source and strength of the possible forces acting on the fluid need to be considered. While some forces can be intuited, such as pressure gradients,

many more forces are possible in plasmas, like forces exerted by electric fields, and collisions. Equations 6.1 and 6.2 are more accurately derived by taking velocity moments of the kinetic equation with the Fokker-Planck Coulomb collision operator. The resulting set of equations are the Braginskii fluid equations which naturally accounts for collisional effects [79]. The typical solution continues by solving for the heat fluxes, $\mathbf{q}$, and the viscous stress tensor, $\mathbf{\Pi}$, using the Chapman-Enskog approach [80]. This approach, while accurate, is extremely involved and not used here. Instead, Stangeby derives a simpler set of equations in one dimension by taking moments of the kinetic equation of a spatially one-dimensional velocity distribution function in an unmagnetized plasma while retaining the Fokker-Planck Coulomb collision operator. That approach is used here as it captures the dominant features in the one dimensional case assumed here. A brief overview of the derivation is included here, with the $\hat{x}$ direction replaced with the $\hat{z}$ notation used in this thesis, while the full derivation can be found in Stangeby's text [81].

The 1D kinetic equation is given as

$$v_z \frac{\partial f}{\partial z} + \frac{eE}{m}\frac{\partial f}{\partial v_z} = \frac{\partial f}{\partial t}\Big|_{coll} + S(z, v), \tag{6.7}$$

where $f(z, v_x, v_y, v_z)$ is the velocity distribution function, $E$ is the electric field, $\frac{\partial f}{\partial t}\Big|_{coll}$ describes the change made to the distribution function through collisions, and $S(z, v)$ is the source rate. The mass conservation equation, Equation 6.5, is obtained directly by taking the first moment of Equation 6.7, i.e. multiplying by $dv = dv_x dv_y dv_z$ and integrating.

The momentum conservation equation is found by multiplying Equation 6.7 by $mv_z dv$ and integrating through. However, as Stangeby points out, since our interest is in *fluid* equations, it is instructive to separate the random velocity of an individual particle, $u_z$, from the bulk velocity of the fluid $V$ such that $v_z = u_z + V$. Here, the bulk velocity, $V$, will only be directed in the $\hat{z}$ direction, but the subscript will be left off to distinguish it from the true particle velocity in the z

direction $v_z$. The resulting moment equation is

$$\frac{d}{dz}\int mu_z^2 f\,dv + \frac{d}{dz}2V\int mu_z f\,dv + \frac{d}{dz}V^2\int mf\,dv + \frac{eE}{m}\int mv_z\frac{\partial f}{\partial v_z}\,dv = \int mv_z\frac{\partial f}{\partial t}\bigg|_{coll}dv + \int mv_z S(z,v)\,dv \quad (6.8)$$

The left hand side of the equation yields

$$\frac{d}{dz}\int mu_z^2 f\,dV = \frac{d}{dz}\left(mn\langle u_z^2\rangle\right) \quad (6.9)$$

$$\frac{d}{dz}2V\int mu_x f\,dV = 0 \quad (6.10)$$

$$\frac{d}{dz}V^2\int mf\,dV = \frac{d}{dz}\left(mnV^2\right) \quad (6.11)$$

$$\frac{eE}{m}\int mv_z\frac{\partial f}{\partial v_z}\,dV = -eEn \quad (6.12)$$

In Equation 6.9 Stangeby implicitly assumes the distribution function is Maxwellian, thus defining $\langle u_z^2\rangle = kT/m$, which makes $mn\langle u_x^2\rangle = nkT = P$ the pressure. Stangeby further differentiates between parallel and perpendicular temperatures which yields parallel and perpendicular pressures, $p_\parallel$ and $p_\perp$. This will be particularly important in this work in that parallel pressure gradients, $\frac{\partial}{\partial z}p_\parallel$, are often a dominant force giving rise to parallel flows. Additionally, parallel and perpendicular pressures and temperatures can be measured independently in MARIA plasmas with the LIF system, and may not be equal to each other. Equation 6.11 is simply the dynamic pressure, or momentum associated with the fluid flow. The final term, Equation 6.12 is the force imparted on the ions by any electric field that develops.

The terms on the right hand side of Equation 6.7 give the momentum exchange by collisions, and the momentum gained/lost by ionization. Stangeby identifies three dominant terms contributing to momentum exchange. The first is the drag caused by ion neutral collisions. The formulation used is the exponential decay of a flux of hard colliders, $\Gamma$, as they travel through a cloud of objects with density $n_n$: $\frac{d\Gamma}{dx} = -n_n\sigma\Gamma$. This formulation yields a mean free path between collisions

$\lambda_{mfp} = (n_n\sigma)^{-1}$ where $\sigma$ is the characteristic cross-sectional area of the target particles. The mean time between collisions is thus $\tau = \lambda_{mfp}/v$. For a Maxwellian distribution of particles this term must be averaged over the Maxwellian velocity distribution yielding the average collision frequency $\nu = \langle\tau^{-1}\rangle = n_n\langle\sigma v\rangle$. The second term from the collision operator is similar to the ion-neutral collisions, but for ion-electron collisions. The details of calculating the ion-electron collision frequency, $\nu_{ei}$ are left out for brevity but can be found in Stangeby's text. The final term relates to any electron temperature gradients that may exist in the plasma, $dT_e/dz$. Again, the details neccesary for its development are complex but physically hot electrons collide less frequently with ions than do cold electrons. This means electrons on the colder side of an ion exchange more momentum with the ion than from the hot size and generate a force in the direction of the temperature gradient.

Combining all these terms together yields the 1D momentum equation for an unmagnetized plasma with Coulomb collisions given in Stangeby's text:

$$\begin{aligned}\frac{d}{dz}(m_i n V^2 + p_{\|i}) - eEn = &- m_i(V_i - V_n)\overline{\sigma V_{in}} n_n n \\ &+ m_e(V_e - V_i)\nu_{ei}^{mom} n \\ &+ 0.71 n \left(\frac{dkT_e}{dz}\right) \\ &+ m_i V_n S_p(z)\end{aligned} \tag{6.13}$$

Unfortunately, despite the trying to simplify as much as possible, most of the terms on the right hand side of Equation 6.13 still cannot be measured directly on MARIA. What can be measured is the flow momentum (or dynamic pressure) term, $mnv^2$, the static pressure, $p_{\|i} = n_i k T_i$, and the source rate $S_p(z)$. In the absence of any collisions or electric fields, the sum of the static and dynamic pressure would be a constant value along the axial direction of the device. Within the assumption of 1D transport, any *deviation* from a constant value would then be the result of some

external force acting on the plasma. By observing the location and strength of these deviations, first steps can be taken to better understand the fluid dynamics at play in a helicon plasma.

A particular benefit of doing this research on MARIA involves the neutral gas source and vacuum pumping arrangement. As described previously, the MARIA device is a cylindrical glass chamber in which gas is both introduced and pumped away at the same end of the chamber. This arrangement results in a uniform neutral fill pressure since no pressure gradient along the main chamber is established by the vacuum system. This is beneficial to the study of particle flows because any flows or pressure gradients measured during the plasma discharge are driven by the plasma itself, and not a background neutral particle flow.

The following subsections will introduce an emperical scaling between electron density and the LIF signal that will be essential to inferring the spatial variation of electron densities. The measured flows and densities relevant to the mass conservation equations are presented in Subsection 6.3. Utilizing the insights gained from the flow measurements, deviations from constant total pressure are assessed and the implications for the momentum balance are discussed. Finally, radial flow measurements are taken to check the validity of neglecting radial transport in deriving the conservation equations, and to investigate the importance of radial fueling and exhaust.

### 6.3.2 Scaling of LIF with Electron Density

The principle tool used to investigate the particle flows in MARIA is LIF. As described in Section 4, LIF works by using laser light to excite atoms in some initial state to a higher excited state and then recording the fluorescence light emitted as the atoms spontaneously decay from the upper state. It was shown that this process, and the intensity of the LIF signal, will be linearly proportional to the population density of the initial atomic state. The plasma processes that dictate the population density of the pumped level are complex, but could in principle be solved for using the collisional radiative model described in Section 3.2. However, in this particular case an empirical

scaling between the argon ion LIF intensity and electron density was established by taking LIF measurements at the same location as the Langmuir probe.

The relationship between electron density as measured by the Langmuir probe and the argon ion LIF intensity with the LIF laser aligned both along the chamber axis and perpendicular to it is shown in Figure 6.12. A power law equation of the form $n = cx^b$, where $x$ is the LIF intensity, was found to be the best fit to the data. The fact that this is not quite linear, and a power law is a better fit to the data than a straight line, suggests that the population mechanism for the metastable state being pumped has some additional variation with density. The axial LIF to density scaling measurement was taken immediately before taking the axial LIF data, and radial scaling immediately after taking the radial LIF data. Between the two sets of measurements a vacuum leak was discovered and repaired. The long operation at high density, greater than 340 total hours for the LIF data alone, takes its toll on the chamber conditions. Cleaning of the chamber during the repair likely led to the improved chamber conditions and higher electron densities for the radial LIF data.

### 6.3.3 Axial Particle Balance

Utilizing the LIF signal to electron density scaling, the LIF diagnostic becomes much more useful for interrogating the plasma. By taking LIF measurements along the axis of MARIA, the change in ion flux as a function of magnetic field strength can be directly measured. According to the 1D mass conservation equation, Equation 6.5, taking the divergence of the flux yields the ion source rate. To achieve this, the argon ion LIF intensity measurements were converted to an inferred electron density, $n_i$, and multiplied by the directly measured flow velocity, $V_z$, to yield the ion flux, $n_i V_z$. The derivative was then computed to yield the ionization source rate.

An overview of data derived from the LIF measurements is shown in Figure 6.13. For reference, the center of the 140 mm long antenna is located at an axial position of 210 mm, and the

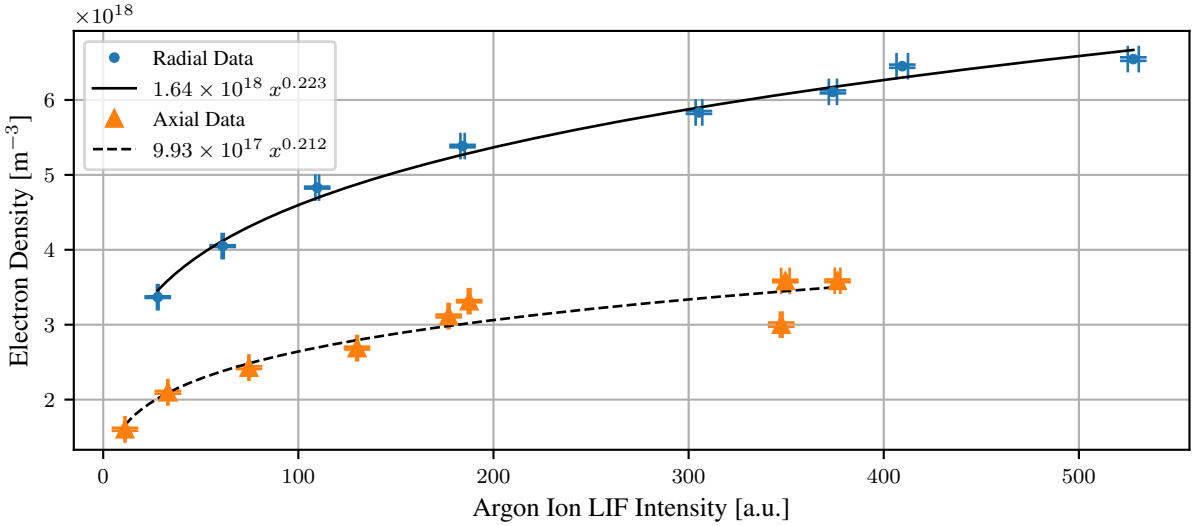


Figure 6.12: Electron density vs argon ion LIF intensity scaling for axial and radial LIF measurements.

downstream boundary plate is located at 1684 mm. The argon ion LIF intensity is shown in panel 6.13a, and the trend of increasing intensity with increasing magnetic field is obvious. The location of the ion LIF intensity peak is centered around an axial position of 1000 mm indicating the maximum electron density is in that region. The argon ion LIF measurement requires a sufficient density of ions to achieve a measurable signal so regions of low LIF intensity indicate a region of low ion density. For some measurements, specifically at 210 mm, the signal was indistinguishable from the background noise and no data is plotted.

Converting the ion LIF intensity to electron density, $n_i$, yields the spatial distribution of electron density and is shown in panel 6.13c. Here it becomes clear that the electron density does in fact increase approximately linearly with the applied magnetic field strength, especially between 1000 mm and 1600 mm. The deviation from linear scaling at 210 mm and 680 mm indicates poor agreement with the helicon dispersion relation in this region. Additionally the continued electron

density growth downstream of 680 mm suggests bulk ionization is not occurring at the antenna but further downstream.

The parallel ion flow velocity, $V_{i,z}$, measured directly by the LIF diagnostic on the chamber axis is shown in panel 6.13b. The velocity zero crossing near 850 mm clearly indicates an ion source in that region, and the nearly exponential increase in velocity leaving the plasma near the boundary plate is likely due to the magnetic pre-sheath in that region [65].

The parallel ion flux, $\Gamma_{i,z}$, is calculated by multiplying the ion velocity by the inferred density and shown in panel 6.13d. The flux increases nearly monotonically with greater downstream distance from the antenna and increasing magnetic field strength. The slight flattening, and slight decrease for magnetic field strengths between 550-750 G, is a curious feature that is discussed in Section 6.3.5.

Finally, taking the divergence of the ion flux, $d\Gamma_i/dz$, yields the ionization source rate, $S(z)$, shown in panel 6.13e. A clear positive ionization source is seen between 450 mm and 1480 mm. The ionization rate is independent of magnetic field strength up to 865 mm, and increases with magnetic field strength further downstream. An unfortunate side effect of the spatial resolution available in this plot and the scatter in the data is that taking the derivative of this discreet data amplifies the scatter.

A couple trends in particular stand out in the graphs in Figure 6.13. First, the peak of the axial density profile seen in panel 6.13c starts around 850 mm for low magnetic field strength, and shifts downstream closer to 1100 mm with increasing magnetic field strength. Second, the electron density at 680 mm initially increases with magnetic field strength but appears to hit an upper limit around 750 G while the downstream density continues to increase with further increases in magnetic field strength. This shift suggests a shift in the region where the most ionization is occurring.

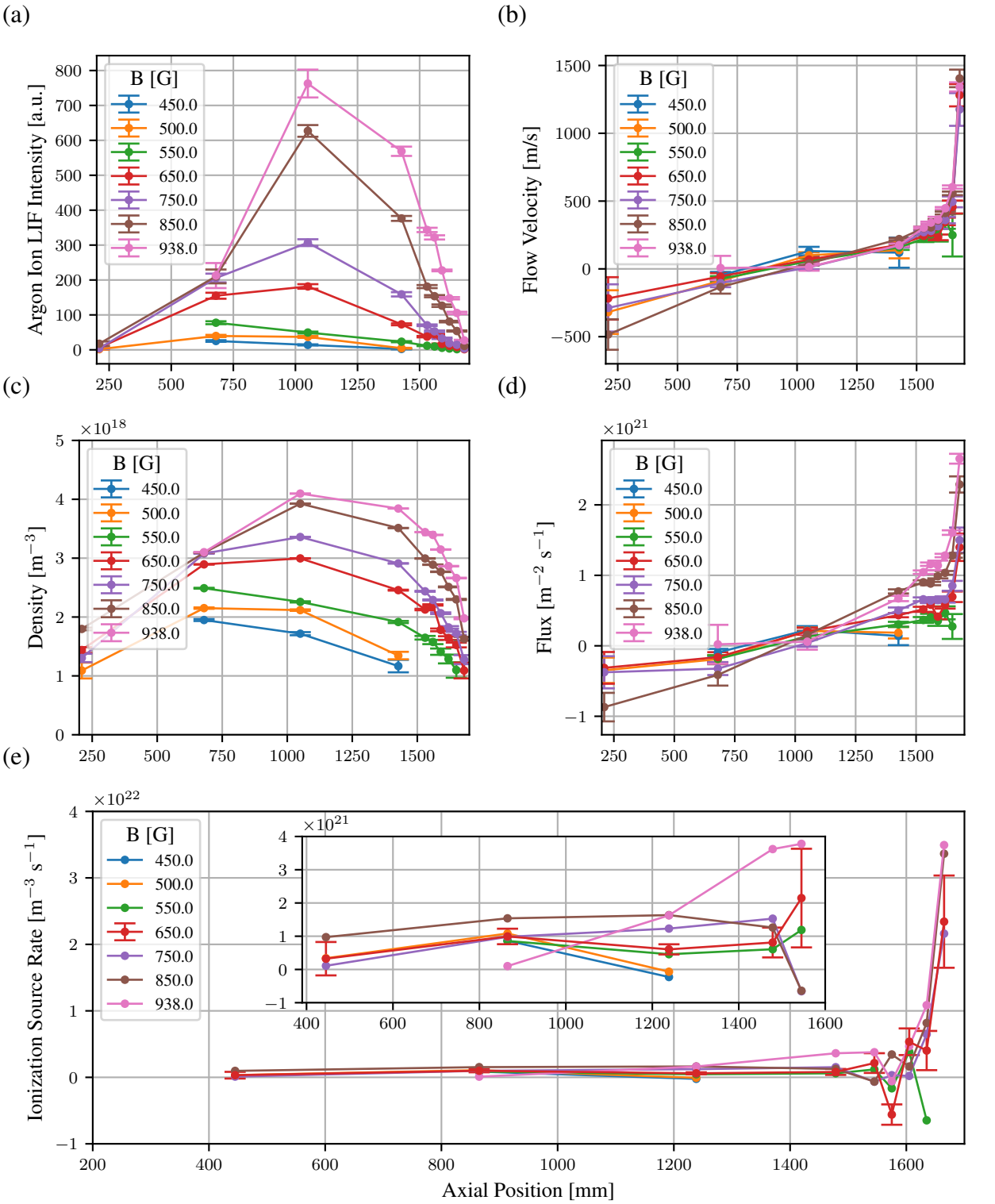


Figure 6.13: Argon ion intensity and ion flow velocity from LIF measurements (panels a and b), inferred electron density and ion flux (panels c and d), and the ionization source strength assuming a 1D particle balance (panel e). Typical ionization source uncertainty is indicated by the 650 G trace.

By looking at the inferred ionization source rate in Figure 6.13e, it appears that indeed the ionization source strength increases with magnetic field strength. The most notable increase appears between 1200 mm and 1450 mm. Increasing the magnetic field strength from 550 G to 938 G increases the ionization source rate from $5.9 \times 10^{20}$ $\mathrm{m^{-3}s^{-1}}$ to $3.6 \times 10^{21}$ $\mathrm{m^{-3}s^{-1}}$.

A particularly interesting feature of the ion flux measurements is the slight dip at an axial position of about 1600 mm. Using the simple 1D divergence calculation, this dip yields an ion sink at this location. It's not immediately clear if the dip is a result of a true ion sink, like recombination or perhaps radial trapsort, or perhaps an artifact of noise amplified in taking the derivative. LIF can again be leveraged to probe possible causes more comprehensively and are discussed in Section 6.3.5 after more LIF data is introduced and a more complete picture of the processes occurring in this region is established. However, a geometric explanation is briefly explored before continuing with the presentation of axial particle balance results.

One possibility that might explain the dip concerns the magnetic field geometry in relation to the LIF pump laser beam. In performing the LIF measurements the diameter of the laser beam expands quite slowly, with a divergence angle of about .5 mrad, and does not change as a function of magnetic field strength. However, the ion density can in principle vary with magnetic field strength, independent of any helicon ionization effects. If one assumes that the plasma is perfectly conducting, and Alfven's frozen in theorem is valid, then a magnetic flux expansion in a free streaming region (collisionless with no ionization) would necessarily decrease the plasma density. The density decrease measured by LIF in such a region is accurate, i.e. number of atoms per unit volume decreases, but in principle could be regained by magnetic compression. The Zeeman effect is the cause of the significant first order frequency splitting between the $\sigma^+$ and $\sigma^-$ groupings, shown in Figure 4.2, and is linearly proportional to the magnetic field strength. By measuring the distance between the $\sigma^+$ and $\sigma^-$ groupings, the local magnetic field strength can actually be measured directly and is shown Figure 6.14. The dip in the magnetic field strength seen near 1600

Table 6.1: Summary of metrics for degree of magnetization for electron density of $2 \times 10^{18}$ m$^{-3}$.

| **Magnetic Field** | **Larmor Radius / Chamber Radius** | **Ion Cyclotron Frequency / Ion-Ion Collision Frequency** |
|---|---|---|
| 200 G | 0.19 | $2.6 \times 10^{-3}$ |
| 500 G | 0.08 | $6.6 \times 10^{-3}$ |
| 800 G | 0.05 | $1.0 \times 10^{-2}$ |

mm in Figure 6.14 could be the reason behind apparent decrease in density, but does not decrease the number of particles flowing along a magnetic field line. This is the desired effect of advanced divertor concepts [82, 83, 84].

To investigate the plausibility that magnetic flux expansion is at play here, the limits of the Alfven's frozen in law must be considered. First, no real plasma is free of collisions with infinite conductivity. In particular, particle collisions can facilitate motion across magnetic field lines and introduce a dissipative drag, thus yielding the more realistic resistive magnetohydrodynamics (MHD) equations. In this case, the primary concern is whether the ions maybe considered *magnetized*. A few parameters are typically considered for establishing the degree of magnetization but the two that make the most sense here are the ratio of the ion-cyclotron frequency to the ion-ion collision frequency and the ratio of the ion Larmor radius to the chamber minor radius [85, 86]. Ion cyclotron to collision frequency ratios greater than 1 and Larmor radius to chamber radius ratios less than $\sim .1$ indicate higher degrees of magnetization. These metrics are shown for several magnetic field strengths in Table 6.1. The Larmor radius to chamber radius metric suggests the ions are reasonably magnetized. However the ratio of ion cyclotron frequency to ion-ion collision frequency less than 0.01 suggests weak magnetization. The truth is likely somewhere in between where frequent collisions allow ions to travel relatively freely across the magnetic field.

For the sake of curiosity, if the ions *are* moderately magnetized the particle flux measurements can be corrected for the local magnetic field strength using the LIF measurements. The correction

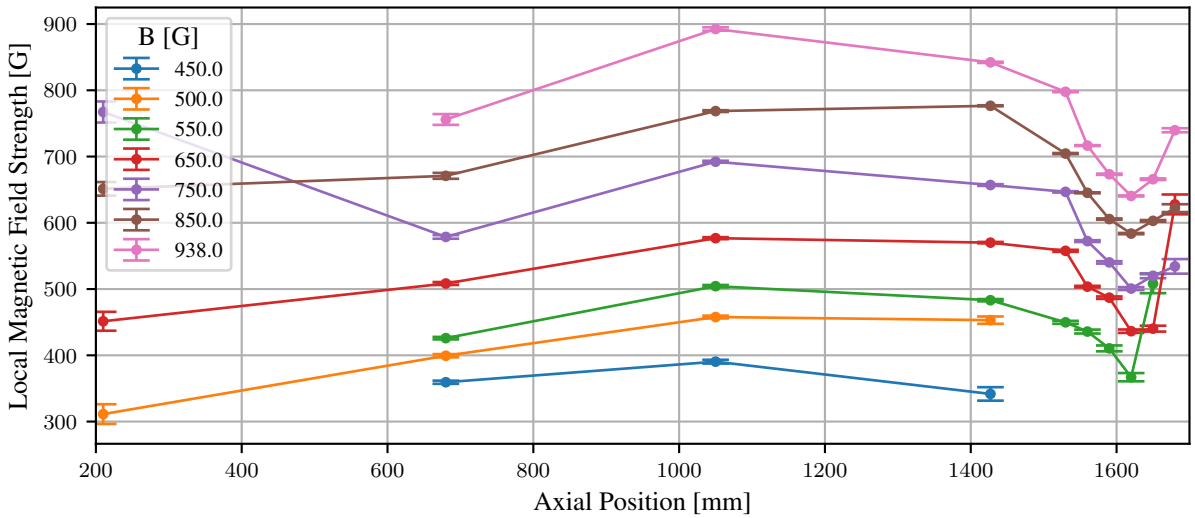


Figure 6.14: By measuring the splitting between the $\sigma^+$ and $\sigma^-$ groupings, the magnetic field in the observation volume can be measured. Here the dip in the magnetic field strength near 1600 mm due to the non-Helmholtz coil spacing is quite evident.

is achieved by scaling the inferred density by the ratio of the local magnetic field strength to the magnetic field strength at the probe. The magnetic field strengths used here are those measured with the LIF diagnostic. The reference field strength, $B_p$, is that measured at the Langmuir probe during the calibration shown in Figure 6.12. The resulting correction factor then scales the inferred electron density by $n_{e,c} = \frac{B(z)}{B_p(z)} n_e$. The correction does reduce the slight dip in the ion flux measurements, shown in Figure 6.15a, but it adds an odd bump at the same 1600 mm location in the density measurement shown in Figure 6.15b. This density bump may or may not be physical, but there are plenty of other possible causes for the flattening of the ion flux that must be considered before drawing a conclusion. These possibilities will be discussed in Section 6.3.5.

By carefully examining many plasma emission spectra in the 300-400 nm range MARIA plasmas appear to be dominated by neutral and singly ionized argon; no emission from doubly ionized argon was observed. Any ion sources must therefore also be a neutral atom sink. Determining

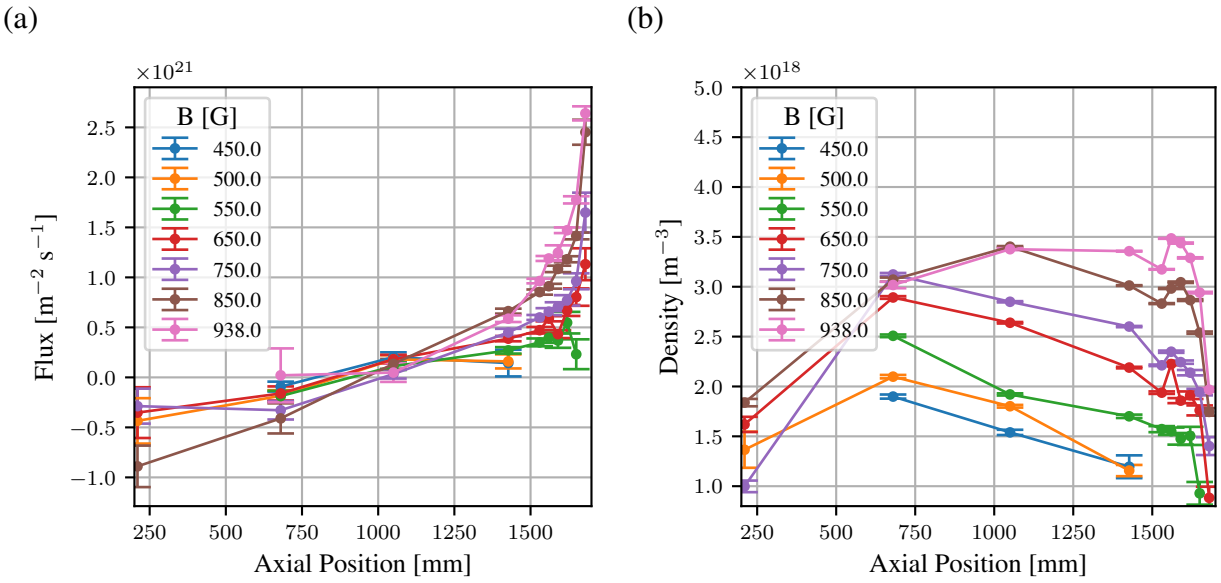


Figure 6.15: Adjusting the LIF data to account for the varying magnetic field strengths removes the dip in the particle flux at 1600 mma a.), but introduces a bump in the electron density data at the same location b.)

the ionization rate by measuring how quickly neutral atoms are lost would add confidence to the ionization rates determined from the divergence of the axial ion flux.

To address this question, the LIF laser can be tuned from the 668.6 nm ion line to a neutral line at 667.9 nm enabling LIF measurements on the neutral argon atoms as well. The neutral argon LIF scheme pumps the 4s $^2$[3/2] 1 level, and thus the intensity of the LIF signal will be proportional to the population density of that level. The intensity of the neutral argon LIF signal shown in the top panel of Figure 6.16 is very low near the boundary plate, builds up to a maximum 120 mm from the plate and decays exponentially as the distance from the plate increases. The signal intensity, and thus population density of the 4s $^2$[3/2] 1 level, increases with magnetic field strength to about 550 G before decreasing dramatically with further increases to the magnetic field strength. At 450 G a relatively broad axial profile is measured with significant measurable intensity at 680 mm. As the magnetic field strength is increased, the neutral LIF response becomes more axially localized

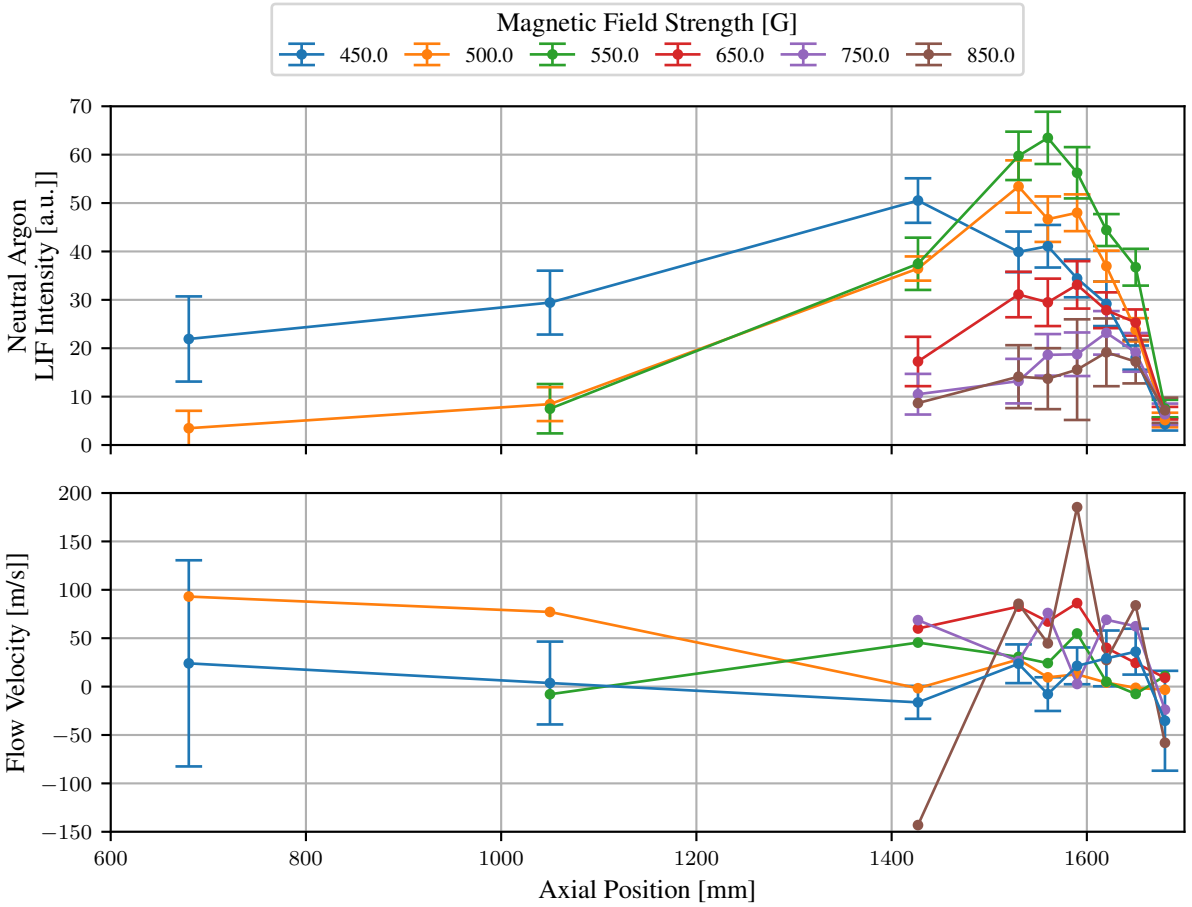


Figure 6.16: 4s $^2$[3/2] 1 level intensity and velocity measured using LIF. Because neutral particles are not confined to the magnetic field lines, radial diffusion and flow cannot be ignored. Typical low velocity error bars are shown on the 450 G trace.

near 1550 mm. The intensity profile indicates that for magnetic field strengths between 500-650 G, a significant population of neutral atoms in the 4s $^2$[3/2] 1 level builds up directly in front of the boundary plate. The physics underlying this buildup of neutral particles in front of the plate is not immediately obvious, but the unique shape of the neutral intensity distribution holds key information.

The flow velocities were difficult to measure accurately due to their low flow speed and relatively low intensity. During the data acquisition, each data point was taken approximately every

5 MHz of laser tuning frequency. A 5 MHz difference in the location of the fitted curve's peak corresponds to 4 m/s, approximately 10% of the typical measured velocities. This lower limit in resolution and the uncertainty from fits to the data contributed to the significant scatter in the data. As a result of the scatter, no trends could be claimed with significant confidence. However, as can be seen, no significant scaling with magnetic field strength exists so averaging the measured speeds over the magnetic field strengths can give some indication of the axial variation. Considering only the average variation with axial position, a flow velocity of 25 m/s away from the plate is measured 4 mm in front of the plate. At a distance of 60 mm from the plate the average velocity reversed to 30 m/s back *towards* the plate. Flow velocities further than 250 mm from the plate were increasingly difficult to measure due to rapidly diminishing signal to noise ratio which itself was due to a rapidly decreasing population of neutral argon atoms in the 4s $^2$[3/2] 1 level.

Unlike the argon ion LIF data, which could be tied to electron density through quasi-neutrality and the Langmuir probe, no other neutral density diagnostics are available on MARIA. However, a simple model can be fit to the neutral argon LIF intensity profiles to estimate the ground state neutral density.

Recognizing that position and time are related through the measured velocities, $\frac{dn}{dt} = \frac{dn}{dx}\frac{dx}{dt}$, the neutral LIF data can be fit very well by a simple 2 species exponential decay of the form:

$$\begin{aligned} \frac{dn_1}{dx} &= -\lambda_1 n_1 \\ \frac{dn_2}{dx} &= -\lambda_2 n_2 + c\lambda_1 n_1 \end{aligned} \tag{6.14}$$

This system has the solution:

$$\begin{aligned} n_1 &= n_0 \exp(-\lambda_1 x) \\ n_2 &= \frac{c\lambda_1 n_0}{\lambda_2 - \lambda_1}(\exp(-\lambda_1 x) - \exp(-\lambda_2 x)) \end{aligned} \tag{6.15}$$

In this simple model, $n_1$ is the density of the argon ground state as a function of distance, $n_2$ is the density of the 4s $^2$[3/2] 1 level, and $\lambda_1$ and $\lambda_2$ are the decay rates of the ground and

4s $^2$[3/2] 1 levels respectively. The constant scaling factor $c$ represents the fact that not all of the atoms leaving the ground state end up in the 4s $^2$[3/2] 1 level. The intuitive process occurring here is a constant stream of ions are impinging on the boundary plate, neutralizing and recycling back into the plasma. As the neutral particles flow back into the plasma they are exposed to an intense stream of electrons which ionize the gas through step-wise electron impact excitation and ionization.

Here, the ground state density, $n_0$, is a constant fixed value at the boundary plate and is determined by the various physical process occurring at the plate, including neutralization and recycling. The physical details of the various processes occurring are not important here, only that the result is some density of argon atoms in the ground state at the surface of the plate. The 4s $^2$[3/2] 1 level is then populated by electron impact excitation from the ground and 4s $^2$[3/2] 2 metastable levels, and by decays from higher excited levels at a rate determined by the local electron temperature and density. Due to the low excitation rate from the ground level and relatively slow evolution rate of the metastable states, the population of the $4s\ ^2[3/2]1$ level can also evolve rather slowly. As the neutral gas progresses further into the plasma it is quickly lost due to ionization.

Modeling the spatio-temporal evolution of the 4s $^2$[3/2] 1 level near the plate is possible in principle, but the non-constant electron temperature and density make this a difficult problem to solve. Unfortunately, not enough information is available to constrain the value of $c$. However, recognizing that $c$ only serves as a density scalar for the 4s $^2$[3/2] 1 level, one can proceed with an arbitrary value for $c > 0$ and an estimate of the ground state density can still be obtained.

The fact that such a simple model is able to fit the neutral argon LIF intensities so well supports the idea that basic recycling followed by electron impact excitation and ionization is occurring in front of the plate. Based on this basic approach, understanding the dependence of the coefficients used in Equation 6.15 on the applied magnetic field strength, shown in Figure 6.17, is straightforward. The increase in $n_0$ can quickly be understood to be a direct reflection of the incident ion

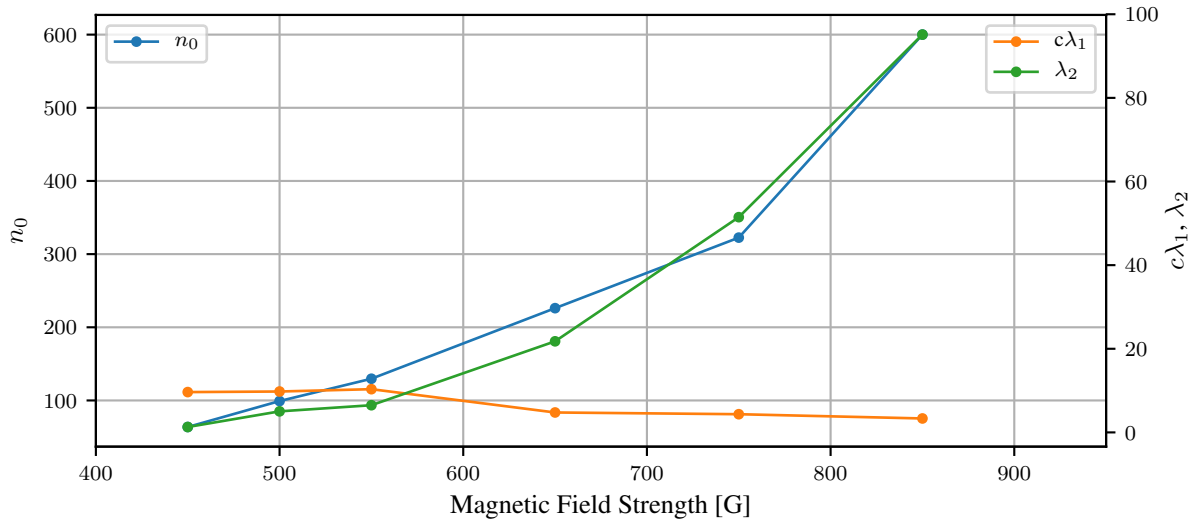


Figure 6.17: The increase of $n_0$ with magnetic field strength is not surprising and corresponds to increasing flux due to an increasing incident flux of ions. The increasing flux of ions comes with an increasing flux of electrons due to ambipolar flow which necessarily increases the ionization rate $\lambda_2$. The cause of the $\lambda_1$ variation is not well understood but is believed to be a combined effect of the ground state argon density and incident electron density.

flux shown in Figure 6.13, i.e. flux divided by the recycling flow velocity. From conservation of mass in one dimension, the neutralizing ions must appear as a neutral density at the plate. The increasing value of $\lambda_2$ can also be understood to be proportional to the ionization rate. The fact that $\lambda_2$ tracks the value of $n_0$ so well is a curious feature that is not a constraint of the model. It is intuitive however that the flux of ions recombining on the plate, and thus the recycling flux of neutrals, is proportional to the flux of electrons and by extension the ionization rate. The physics behind the variation of $\lambda_1$ is a combined effect of the ground state argon density, incident electron density and temperature, and the electron impact excitation rate.

By again demanding that conservation of mass be satisfied in the small volume in front of the plate, and again neglecting the radial transport terms, the flux of ground state argon atoms

Table 6.2: Ionization rates found from the neutral argon LIF data.

| Magnetic Field Strength [G] | Ionization Probability [1/s] | Ionization Rate Coefficient [$m^3$/s] |
|---|---|---|
| 450 | 25 | $2.1 \times 10^{-17}$ |
| 500 | 125 | $9.3 \times 10^{-17}$ |
| 550 | 150 | $7.8 \times 10^{-17}$ |
| 650 | 550 | $2.2 \times 10^{-16}$ |
| 750 | 1275 | $4.3 \times 10^{-16}$ |
| 850 | 2375 | $6.8 \times 10^{-16}$ |

appearing at the boundary plate must be equal and opposite to incident ion flux. To do so, a value for the recycling velocity must be found. The neutral flow velocities seen in Figure 6.16 are pretty scattered, but the average velocity for all magnetic field strengths 4mm in front of the plate was 25 m/s away from the plate. Using an average recycling velocity of 25 m/s, a scaling of $7.2 \times 10^{16}$ yields a reasonable agreement between the recycling neutral flux and the incident ion flux as shown in Figure 6.18. The ionization rates were calculated by $S = d(nV)/dx = V(dn/dx) + n(dV/dx) = V(dn/dx)$. Dividing by the neutral density yields an ionization probability that is more comparable to the ionizing potential of the incoming stream of electrons. The ionization rate coefficient can be found by dividing again by the electron density found from the ion LIF data. The ionization rates are shown in Table 6.2

By solving the same collisional radiative model used in Section 6.2 in a time dependent manner, this same analysis can be done in a slightly more sophisticated manner. As discussed above, the actual excitation process is complicated by an unknown electron temperature profile near the boundary plate. However, proceeding with a linear fit to the electron density profile measured by the argon ion LIF data at 550 G and assuming the electron temperature is constant and equal to the bulk electron temperature is a reasonable first order estimate. The axial population density profile of the neutral argon 4s $^2$[3/2] 2 level (the 3rd excited level from ground) was calculated by a time

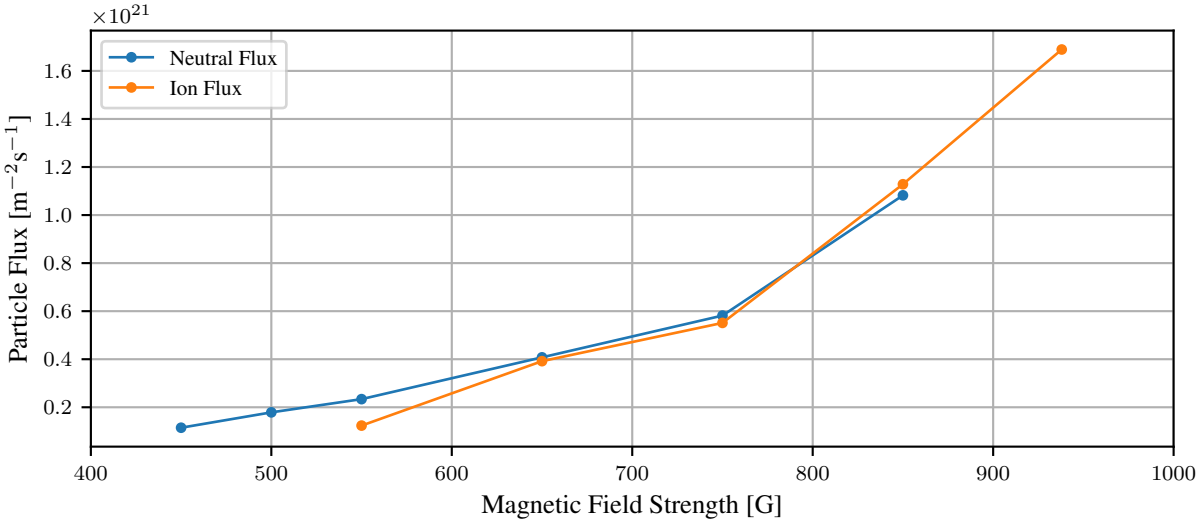


Figure 6.18: Scaling $n_0$ in Equation 6.15 by $1 \times 10^{16}$ and using a recycling velocity of 50 m/s yields a reasonable agreement between the recycling neutral flux and the incident ion flux.

dependent solution of the collisional radiative matrix. The electron density, indicated by the green line, was defined to ramp linearly from zero to $2 \times 10^{18}$ m$^{-3}$ over the first 180 mm from the plate, and the ionization probability of 150 s$^{-1}$ taken from the LIF data (25 m/s $\times$ 6 1/m) ramped from zero over the same distance. The electron temperature was assumed to be a constant 2.5 eV. With these density and ionization profiles in place, the collisional radiative matrix was solved with no metastable states in a time dependent manner using MATLAB's stiff Runge-Kutta solver ODE15S. The results of the calculation are shown in Figure 6.19. The agreement with the experimental data at 550 G, shown by the blue curve, is surprisingly good. The exponential decay for CRM solutions for higher magnetic field strength cases do not agree as well with the experimental data. This is not surprising since the constant ionization rate applied to all levels here is overly simplistic. A more sophisticated ionization model could improve the agreement. However, in all cases the location of the 4s $^2$[3/2] 2 level density peak was recovered. As seen in the velocity data, the velocity right near the plate is an average of 25 m/s away from the plate and was taken to be constant for this

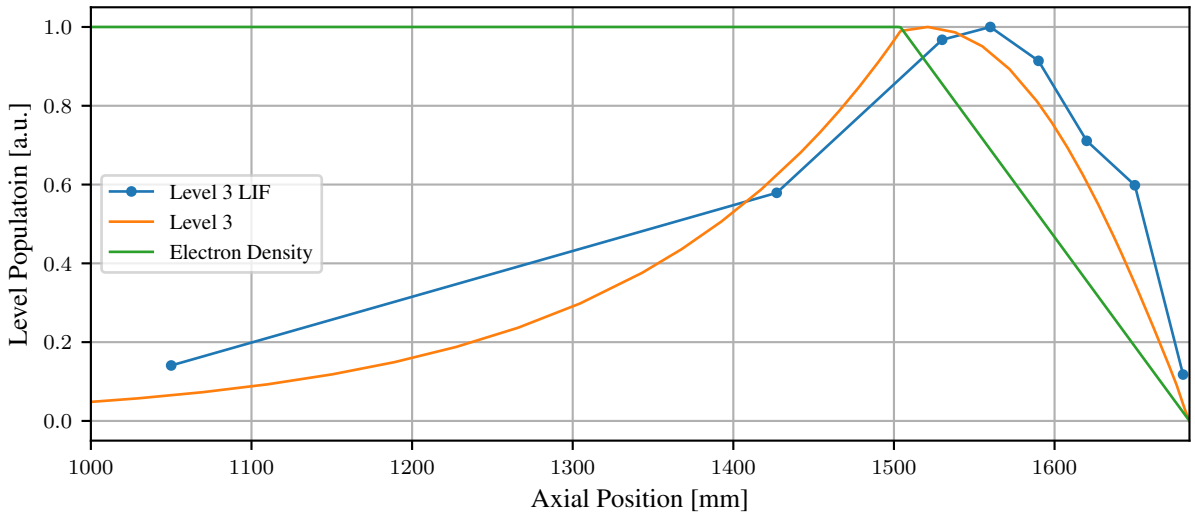


Figure 6.19: Solutions of the time dependent collisional radiative model agree reasonably well with the LIF data. Here an constant flow velocity of 25 m/s was assumed. The electron density was assumed to ramp linearly from 0 to $2 \times 10^{18}$ m$^{-3}$ and the ionization probability ramped from 0 to 150 s$^{-1}$ over the first 180 mm from the plate.

model. Further from the plate there appears to be a flow reversal with the gas flowing back towards the plate with an average velocity of 50 m/s. This change in flow is not as easily accounted for in the simple modeling done here, and the uncertainty associated with the neutral argon flow velocity data would make interpretation of the results difficult at best. However, this relatively simple test adds confidence that the right physics are being captured.

The ionization rate coefficient of $7.8 \times 10^{-17}$ m$^3$s$^{-1}$ ($1.5 \times 10^{21}$ m$^{-3}$s$^{-1}$ when multiplied by a neutral density of $1 \times 10^{19}$ m$^{-3}$ and electron density of $2 \times 10^{18}$ m$^{-3}$) measured from the neutral argon decay rate agrees quite well with theory. The ionization rate coefficient as a function of electron temperature from the ADAS database is shown in Figure 6.20 [59]. The ionization rate was calculated for neutral argon using the configuration average distorted wave code developed at Auburn University and implemented in the ADAS set of codes [87]. The measured value ionization

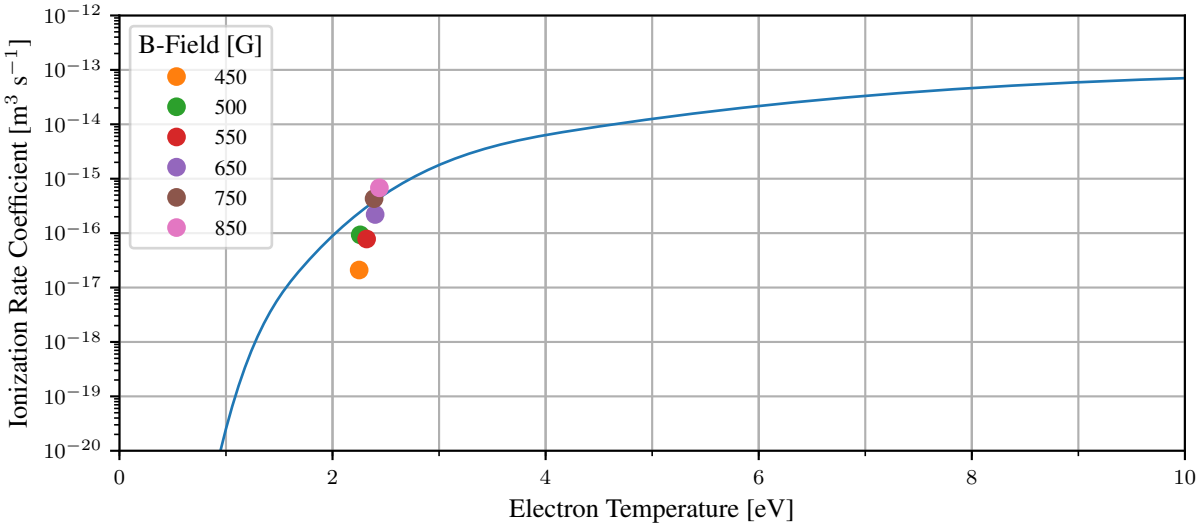


Figure 6.20: The neutral argon ionization rate coefficient from ADAS, line, agrees quite well with the measured rate coefficients, points, for an electron temperature of 2 eV [59]

rate coefficients, shown as dots in Figure 6.20, match a plasma with electron temperature in the range of 2 eV.

This exercise with netural LIF has now yielded a reasonable approximation of the Ar I ground state density which is plotted in Figure 6.21. For reference, the neutral density at 2 mTorr is $7\times10^{19}$ m$^{-3}$ at 273 K. The exponential decay with increasing distance from the boundary plate, and the increasing recycling flux of neutral atoms, $\Gamma_0 = n_0 V$, both increase with increasing magnetic field strength. The increase with magnetic field strength matches the trend of increasing incident ion flux measured from the argon ion LIF data. Of course, these trends follow directly from the assumptions made regarding the physical processes occurring in this region.

The most striking result of the neutral argon LIF analysis is the deep depletion of neutral atoms that occurs on axis. Both the LIF data in Figure 6.16 and the inferred neutral argon ground state density shown in Figure 6.21 indicate that by a distance of 400 mm of the boundary plate, the neutral argon density is approximately 10% of the value at the boundary plate. Additionally the

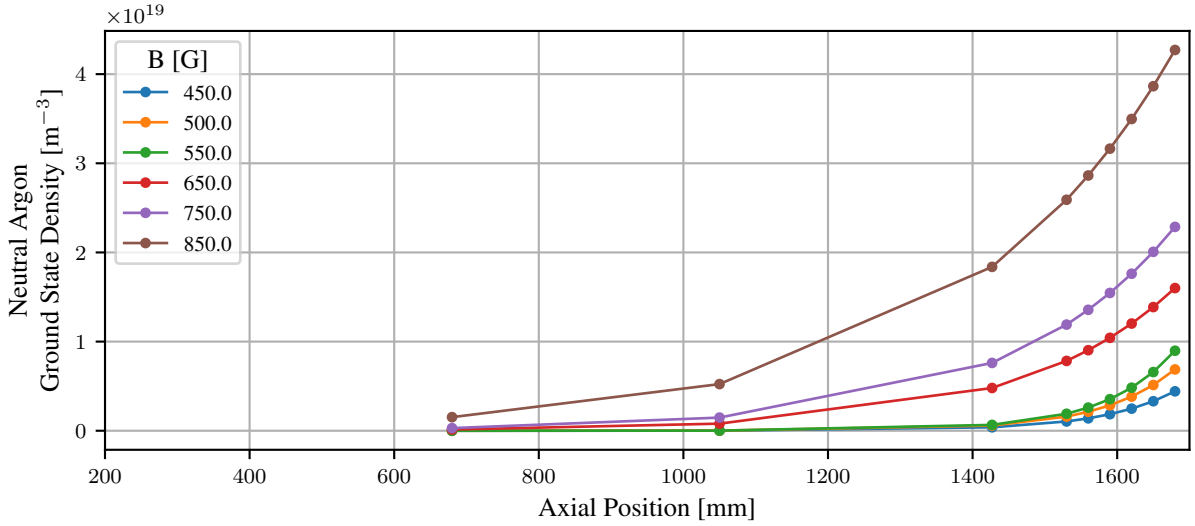


Figure 6.21: By multiplying the LIF data in Figure 6.16 by the scaling factor of $9 \times 10^{16}$ and fitting the data with the simple model in Equation 6.15 approximate densities for the ground level can be obtained.

apparent reversal of neutral flow, with neutral atoms flowing back towards the boundary plate after they've recycled into the plasma, suggests that Magee *et al* were right and that the depletion of neutral atoms observed on axis is due not just to ionization but expulsion.

### 6.3.4 Radial Particle Balance

In the previous section, radial transport was assumed to be negligible and axial particle flux profiles were used to calculate the ionization rate on axis. However, the values calculated using that assumption may be only partially correct if radial transport is significant. The LIF system was rearranged such that the laser was injected radially across the axis and intensities and radial flow velocities were measured off axis. In this way the assumption of radial transport is checked, the calculated ionization rates are adjusted, and the possibility of radial neutral fueling and ion exhaust is measured.

In contrast to the the neutral LIF behavior on axis, decreasing intensity with increasing magnetic field strength, the neutral LIF intensity off axis does not appear to decrease in the same way. The neutral LIF intensity values taken at two axial positions (just after the antenna and close to the downstream boundary plate) and three radial positions (near the axis, 1/3 chamber radius, and 2/3 chamber radius) while varying the magnetic field strength is shown in Figure 6.22. The data near the axis is taken as close to the axis as possible, but not *exactly* at r=0 due to the positioning uncertainty. The radial positional tolerance is 4 mm. The LIF intensity near the axis at both axial positions still decreases by one order of magnitude by increasing the magnetic field strength from 450 G to 850 G, as expected. However with increasing radial distance the depletion with magnetic field strength is much less severe, with the neutral LIF intensity staying constant at r/a=0.67 near the boundary plate. The depletion near the antenna is present at all radial positions but is much less severe, only decreasing by a factor of 3 at r/a=0.67. The population mechanism of the 4s $^2$[3/2] 1 level which is being pumped by the laser by electron impact excitation is important to keep in mind. For constant neutral density, an increase in the electron density would lead to higher excitation rate which in turn would lead to a greater population density in the 4s $^2$[3/2] 2 level. The electron density at radial locations corresponding to the LIF measurements, shown as dotted lines in the figure, is increasing with magnetic field strength. The conclusion from this data is that during the helicon mode of operation deep neutral depletion on axis produces a hollow neutral profile. This begs the question, "Where are the neutral atoms which sustain the plasma coming from?"

More insight into the flow dynamics is gained by considering the radial flow velocity measurements made using the LIF diagnostic which are shown in Figure 6.23. This information was acquired from the same data used to generate the neutral argon LIF intensity figures in Figure 6.22. The top graph shows the radial flow velocity of neutral atoms at the chamber axis. Although the data points are a bit scattered, the general trend is negative flow, away from the axis towards the chamber wall, with the greatest magnitude at 1050 mm where the ion density and temperature is

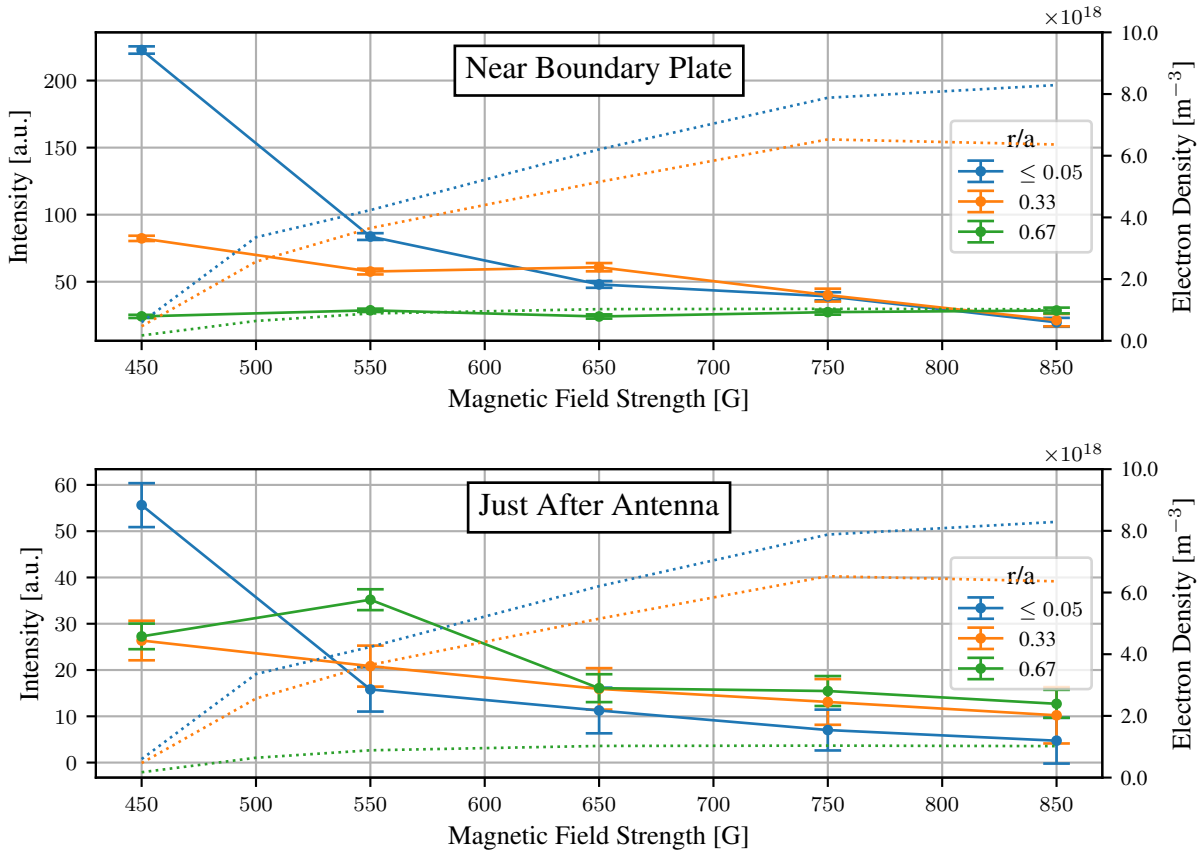


Figure 6.22: The marked decrease in neutral LIF intensity with increasing magnetic field strength (increasing electron density) at r/a $\leq 0.05$ with the negligible decrease at r/a=0.67 indicates the depletion of neutral particles on axis. The neutral LIF intensity is shown by the points, and the electron density measured by the Langmuir probe at the corresponding radial locations is shown by the dotted lines.

highest. The large error bars are a result of the very low intensity resulting in poor fits to the LIF data. The middle graph at r/a=33%, and the bottom graph at r/a=67% shows the flow shifting to positive values, away from the chamber wall towards the axis, at axial positions below 1200 mm. This flow velocity data is a clear indication of radial neutral fueling near the antenna. Unfortunately, unlike the axial neutral flow measurements, the poor radial resolution meant that a tight coupling to the flux of incoming ions couldn't be established and a total neutral flux cannot be calculated.

A similar set of radial LIF measurement were performed for the argon ions. The ion flux measurements shown in Figure 6.24 were calculated in the same manner as for the axial case. The radial ion flux for all radial positions, axial positions, and magnetic field strength is oriented away from the axis. The radial flux is strongest near 680 mm, with a value of $5 \times 10^{20}$ m$^{-2}$s$^{-1}$, where the axial flux is the lowest and the ion temperature is greatest. The magnitude of the flux is comparable to the axial flux, and is a factor of two *greater* than the axial flux at an axial position of 680 mm. Further downstream the radial flux is a factor of two lower, making it about 5% of the total ion flux leaving the core region at axial positions greater than 1400 mm. It is also interesting to note that the perpendicular flux is comparable to Bohm-like diffusion. The Bohm diffusive flux, $J$, is calculated by $J = D_B\, dn_e/dr$ and $D_B = ckT_e/16eB$, where $c$ is the speed of light, $k$ is Boltzman's constant, $T_e$ is the electron temperature, $B$ is the magnetic field strength, and $e$ is the charge of an electron. Taking the density gradient in the radial direction from Langmuir probe measurements gives a radial flux between $1 - 4 \times 10^{20}$ m$^{-2}$s$^{-1}$.

Interpreting the radial velocity measurements must be done carefully due to the magnetic field causing the ions to undergo orbiting via the Lorentz force. As the ions orbit the magnetic field lines, with an orbital velocity component perpendicular to the magnetic field, they will cyclically gain and lose a velocity component parallel to the laser wave vector. The LIF signal will then be affected by both the flow velocity and the orbital velocity. The average of the orbital velocity over an ensemble

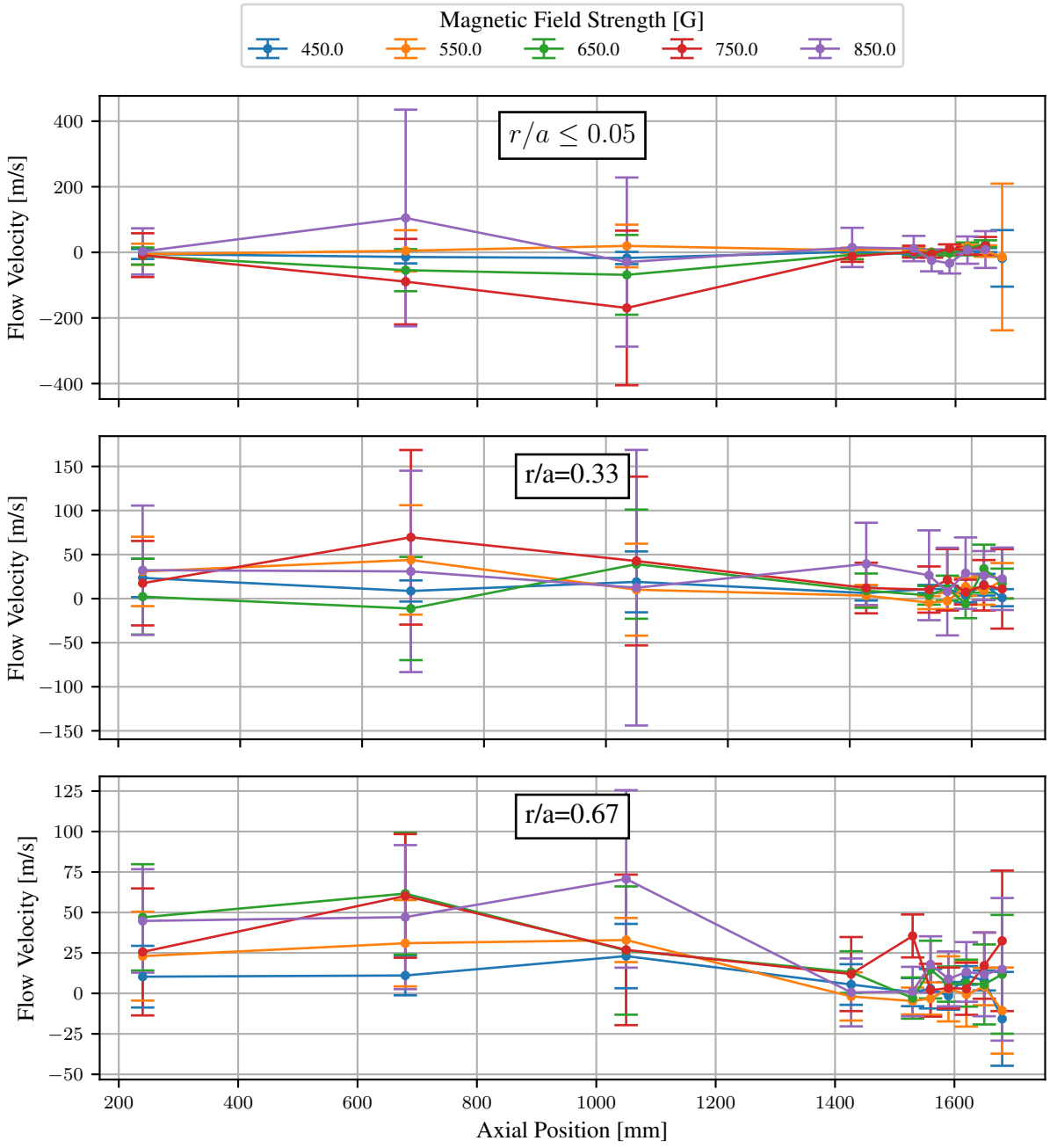


Figure 6.23: Neutral argon LIF radial flow velocity measurements indicate a inward radial flow for axial positions less than 1200 mm. No net flow appears to exist above 1400 mm near the axial boundary plate. The data at r/a $\leq 0.05$ is taken within 4 mm of the axis, but cannot be exactly on axis due uncertainty in radial positioning.

of atoms is still zero. So true radial flow velocities are accurately measured as presented above. However, the orbital velocity due to the Lorentz force represents a line broadening mechanism that can cause erroneous ion temperature measurements. This is an interesting topic for future research.

The conclusion then is that radial losses are not negligible, especially in the antenna region. In calculating the total divergence of the flux, this radial contribution means the ionization rate on axis is in fact higher than what can be inferred from axial measurements alone. Unfortunately the resolution of the radial flux measurements is sufficiently low that the radial variation in flux can only be approximated. Calculating the flux gradient using the data at r/a=0.33 and r/a=0.67, and assuming a linear trend between these two radial positions, boosts the calculated ionization rate by approximately $1 \times 10^{22}$ $\mathrm{m}^{-3}\mathrm{s}^{-1}$, but with an uncertainty of 200%. This puts the ionization rate just downstream of the antenna on par with the ionization rate occurring in front of the boundary plate. Improving the radial resolution of this data is necessary to improve the measurement.

The data in figures 6.22 and 6.23 indicate an inward flow and ionization of neutral atoms at axial positions below 1200 mm. Coupled with the strong axial ion flux divergence at the same axial location shown in Figure 6.13d, this data paints a picture of a circulatory ionization process. As the ionization rate increases and the ions stream into the boundary plate, ions recombine and are ejected back into the chamber at thermal velocities. Due to the intense flux of ions and electrons streaming along the axis, neutral particles that recycle in the axial direction are almost immediately re-ionized and sent back towards the plate. This condition yields a depletion of neutral particles on axis. Particles that recycle with some radial velocity bounce off the chamber walls further upstream, make their way back into the plasma, and start the cycle over again. In the context of the particle balance, the region closest to the antenna is dominated by a radial particle balance transitioning to axial particle balance further downstream. In front of the axial boundary plate a strong local recycling establishes a local particle balance dominated by recycling neutrals which refuel the plasma immediately in front of the boundary plate.

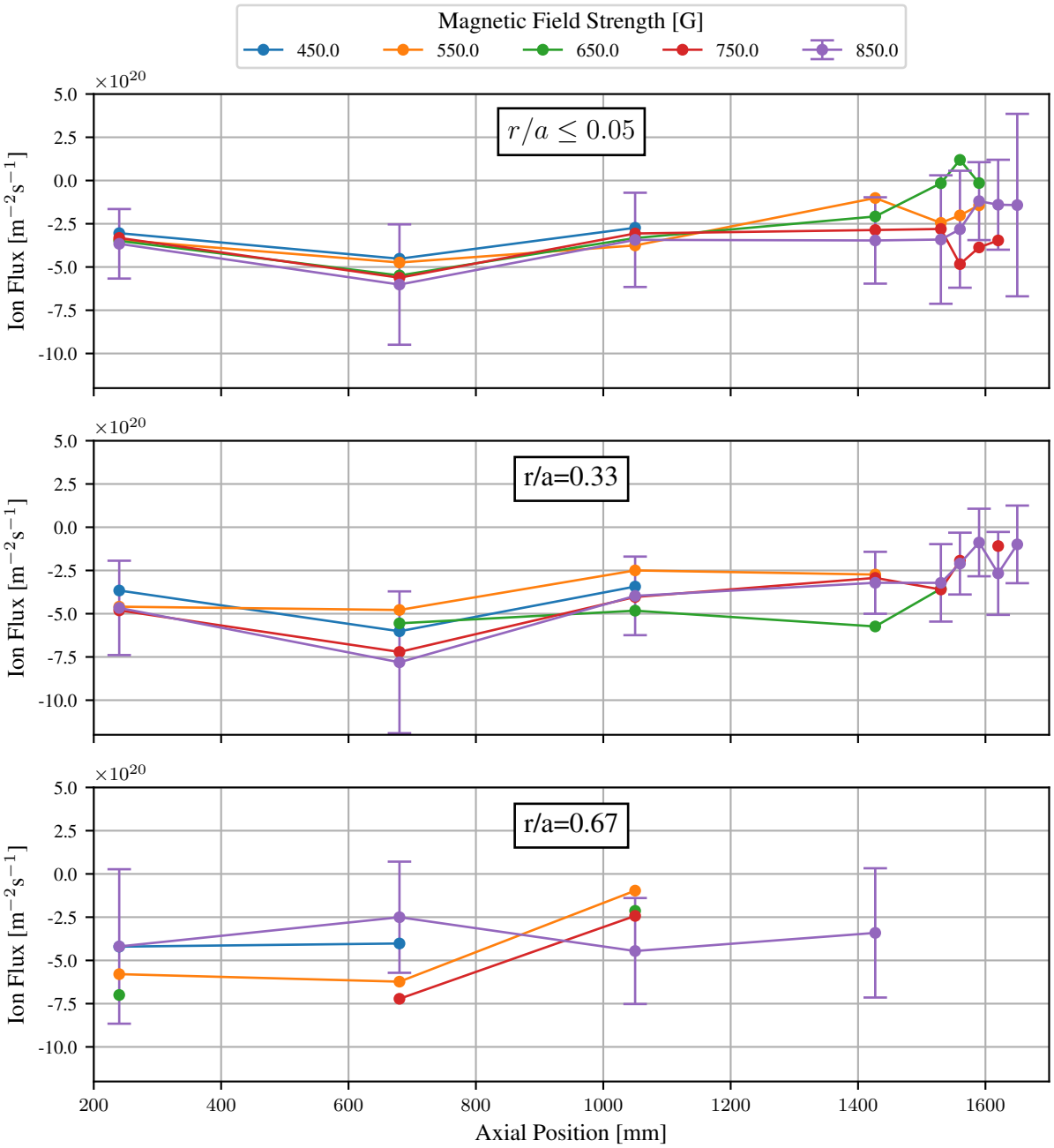


Figure 6.24: Off axis radial argon ion LIF intensity measurements. Typical uncertainties are indicated by the 850 G trace.

The local recycling and particle balance in front of the downstream boundary plate is a unique feature of the MARIA device as it is currently configured. The transition from a radial particle balance to an axial particle balance occurs over the majority of the axial length of the MARIA plasma. In a long open linear configuration attractive to accelerator applications, over 100 m long, a long separation would exist between the power deposition near the antenna and any downstream boundary condition. A similar configuration can be imagined as a MARIA like device opening into an expansion chamber with a high vacuum throughput. In such devices no downstream local refueling would be possible. Investigating such a geometry is a good path to take in expanding on this research for particle accelerator applications. However, the conclusion from this work is that a strictly one dimensional particle balance is only partially correct and does not capture the significant radial transport near the antenna.

To understand the influence of the neutral gas fill pressure, a set of LIF measurements were taken at 2.0 mTorr (the same as the data shown above) and at 1.0 mTorr, shown in Figure 6.25. In doubling the neutral pressure, the argon ion LIF intensity increased by a factor of 2.5 yielding an inferred density increase of 1.5 which matches the trend seen in Figure 6.3a. The flow velocity, shown in the upper right graph, decreased by a factor of 2.6. The increased temperature and reduced out flow for the 2 mTorr case indicates better overall energy confinement which resulted in increased density.

### 6.3.5 Axial Momentum Balance Considerations

The neutral gas buildup in front of the boundary plate is taken to be the result of ions that have recombined on the boundary surface and are recycling back into the plasma. Curiously, the dip in the ion flux discussed earlier, and shown in Figure 6.13, corresponds perfectly to the region where a high density of neutral argon atoms in the 4s $^2$[3/2] 1 level are located. Due to the apparently high density of neutral atoms in this region ion-neutral collisional drag is indeed a plausible cause for

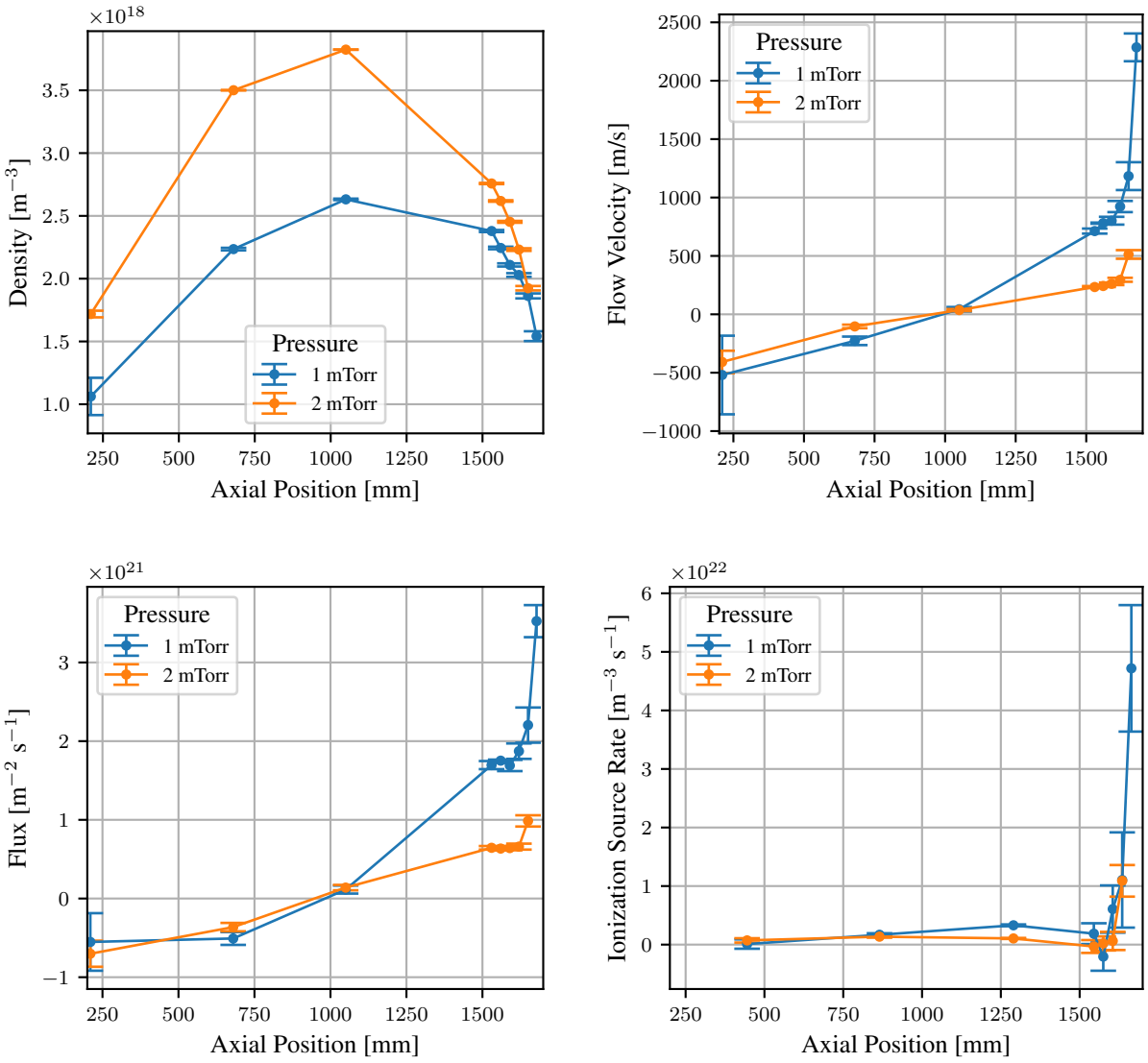


Figure 6.25: LIF measurements at 1 and 2 mTorr. The data here is not adjusted to account for varying magnetic field strengths.

the dip in ion flux. Considering the magnitude of the terms in Equation 6.16, the 1D momentum conservation equation introduced earlier, might yield some insights [81].

$$\begin{aligned}\frac{d}{dz}(m_i n V^2 + p_{\|i}) - eEn = &- m_i(V_i - V_n)\overline{\sigma V_{in}} n_n n \\ &+ m_e(V_e - V_i)\nu_{ei}^{mom} n \\ &+ 0.71 n \left(\frac{dkT_e}{dz}\right) \\ &+ m_i V_n S_p(z)\end{aligned} \tag{6.16}$$

A nice way to understand the particle and momentum balance step-by-step is to assume the plasma is isothermal and collisionless, $\frac{d}{dx}(m_i n V^2 + p_{\|i}) = 0$. If this assumption were true, the sum of the flow pressure, $m_i n V^2$, and static pressure, $p_{\|i}$, should be constant along the plasma chamber. With LIF these two terms are directly measurable and the sum is plotted in Figure 6.26. The sum is not constant along the chamber for magnetic field strengths above 450 G. The steep increase beyond 1600 mm due to the steep increase in flow velocity in that region is quite clear. This increase is assumed to be a result of the magnetic pre-sheath that forms in regions immediately adjacent to boundaries in magnetic devices like MARIA [65]. Any deviation from a constant value is then a contribution from the other terms in Equation 6.13.

Unfortunately MARIA is not equipped to measure many of the other terms directly. However, some approximations can be made to understand the relative strength of each of the terms.

The first term on the right hand side of Equation 6.13, the ion-neutral momentum transfer, can now be considered. The collisional momentum transfer cross section is provided by Jovanovic and to first order is constant at $2 \times 10^{-18}$ m$^2$ [88]. For a relative collision velocity of approximately 300 m/s, an average thermal temperature of .1 eV, a neutral density of $\sim 2 \times 10^{18}$ m$^{-3}$ and an ion density of $\sim 1 \times 10^{19}$ m$^{-3}$, the ion-neutral collisional momentum transport is on the order of $0.5$ Pa/m.

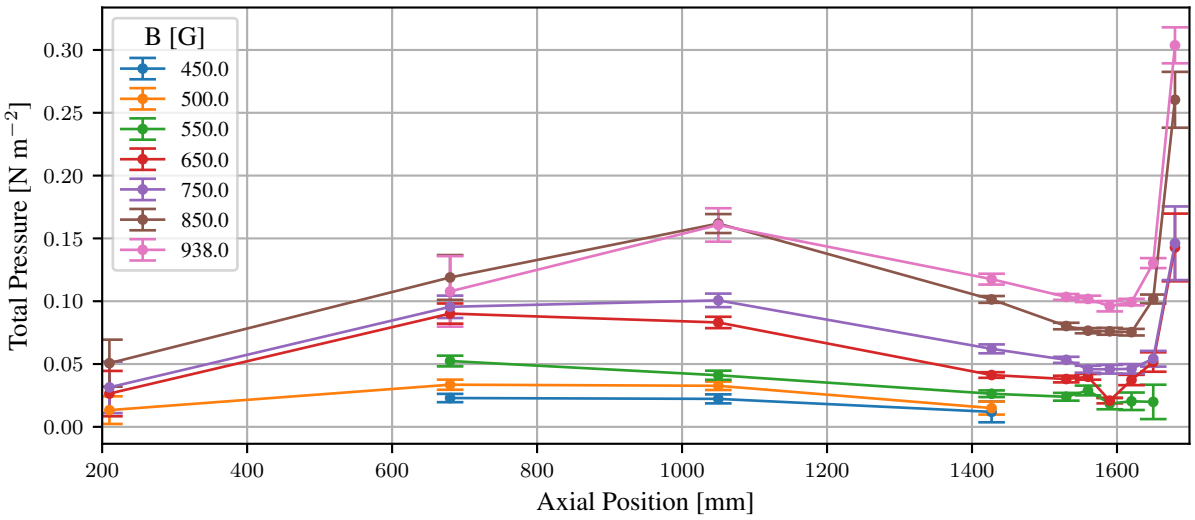


Figure 6.26: By plotting the ion pressure, the effect of drag by ion-neutral collisions becomes more apparent. An adiabatic system would maintain constant pressure along a magnetic field line. The negative gradient above 1200 mm is a direct result of ion-neutral collisions.

For the second term, $\nu_{ei}^{mom}$ can be calculated by

$$\nu_{ei}^{mom} = 2.5 \times 10^{-11} Z_i n_e / T_e^{3/2} s^{-1}. \tag{6.17}$$

where $n_e$ is in m$^{-3}$ and $T_e$ is in eV. For electron temperatures of $\sim$ 3 eV and densities in the range of $2 \times 10^{18}$ m$^{-3}$ this gives $\nu_{ei}^{mom} = 12.7 \times 10^6$ s$^{-1}$. The velocity difference between the ions and electrons is something that simply can't be measured on MARIA currently. Helicon plasmas are currently being investigated for their ability to drive currents in tokamaks [89, 3], so it is reasonable that a current could exist. In MARIA the boundary plate is floating, and unable to conduct a current, but let's imagine a current did exist so the the upper limit of its impact can be approximated. Paul *et al* measured a current of nearly 100 amps in a toroidal helicon device with comparable chamber diameter, RF power, magnetic field strength, and operating pressure, but operating at roughly twice the frequency. Using 100 A at a density of $2 \times 10^{18}$ m$^{-3}$ through an

area of approximately 28 cm$^2$ (3 cm diameter) yields a velocity difference of $1.1 \times 10^5$ m/s. This results in an electron-ion collisional momentum transfer of 2.5 Pa/m.

Momentum drive by electron temperature gradients can be quite large. In this case a .1 eV/m temperature gradient can cause a pressure gradient of 0.022 Pa/m at densities near $2 \times 10^{18}$ m$^{-3}$. The final term, the force necessary to accelerate a recently ionized atom can be estimated from our data. For neutral argon atom velocities in the range of 25 m/s, and an ionization rate of $\sim 2 \times 10^{21}$ m$^{-3}$, this could be $3 \times 10^{-3}$ Pa/m. The final term involves the electric field which cannot really be estimated from the information available.

The greatest pressure difference from the maximum value near 1050 mm shown in Figure 6.26 is on the order of 0.08 Pa/m. Based on the rough order of magnitude estimates above, and the fact that the floating boundary plate cannot conduct a current, ion-neutral collisional momentum exchange appears to be the dominant factor.

#### 6.3.5.1 Tests at High Power

Utilizing the high power helicon test cell at IPP-Greifswald additional investigations regarding the axial vs radial fueling were performed [1]. The hypothesis, following the line of reasoning alluded to above, was that the ion Larmor radius was sufficiently smaller than the chamber radius that the primary loss channel was axial loss to the end plates.

$$r_i = \frac{v_{Ti}}{\omega_{ci}} = 1.02 \times 10^2 \mu^{1/2} Z^{-1} T_i^{1/2} B^{-1}$$
$$r_i = 0.48\text{cm} \tag{6.18}$$

where $\mu$ is the reduced ion mass $m_I/m_H$ where $m_I$ is the ion mass and $m_H$ is the mass of hydrogen, $Z$ is the ion charge divided by the electron charge, $T_i$ is the ion temperature, and $B$ is the magnetic field strength.

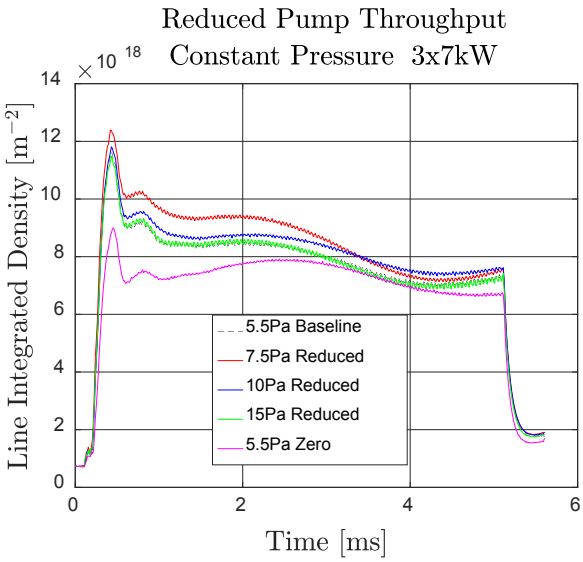


Figure 6.27: Reducing the vacuum pump throughput made little to no impact on the electron density in a pulsed discharge with 21 kW distributed across 3 antennas. In each case the gas source was reduced to keep the base pressure constant at 5.5 Pa. The 7.5, 10, and 15 Pa 'reduced' curves refer to the base pressure that would be reached if the vacuum throughput was reduced while maintaining a constant source rate.

It is then reasonable that a moderate neutral density would build up at the end plate, much like was seen on MARIA, resulting in more ion-neutral collisions and additional viscous drag on the ions which would reduce the ion loss rate. The hope was that this reduction in the ion loss rate would extend the duration of the temporal density peak and result in a higher steady-state density.

The experiment was conducted on a high power helicon test cell at IPP-Greifswald with $B \sim 600$ G and $P_{\mathrm{rf}} \leq 36$ kW. On this device the argon gas flows into the chamber along the axis on one end and is pumped out downstream (in the direction of $\mathbf{B}$) of the antenna. It was believed that the vacuum pump rate was sufficient to inhibit the buildup of the neutral density gradient at the downstream end plate. By gradually closing a valve in the vacuum line, the pumping rate could be reduced thus allowing the neutral density to build up there, mimicking the conditions at MARIA.

The temporal evolution of the electron density as measured by a $CO_2$ interferometer is shown in Figure 6.27. To achieve reduced throughput while maintaining a constant pressure the gate valve leading to the vacuum pump was first closed a small amount leading to a pressure rise in the chamber. This rise in pressure is the pressure indicated in the figure legend. The gas supply flow rate was then reduced with a needle valve until the chamber pressre returned to 5.5 Pa. Throttling the flow rate only led to slightly reduced ultimate densities. However, reducing the vacuum throughput completely to zero resulted in a 25% reduction in ultimate electron density compared to the baseline. The peak electron density was also much closer to the steady state density reached after 5 ms. The electron density in all discharges settled to an equilibrium line integrated density of $7.5 \times 10^{18}$ m$^{-2}$, with the throughput reduction having only marginal impact.

The density drop at zero throughput suggests that the gas source supplying gas on axis actually represents a significant source of neutral particles during the initial buildup of the discharge. The lack of significant impact on the steady-state density indicates that the downstream recycling conditions are still a dominant factor in determining the ultimate electron density achieved. It is also quite plausible that on the few ms timescale of the discharge, the neutral gradient was building up as expected and any effect from the vacuum system simply didn't have time to become established.

# Chapter 7

# Summary and Future Work

The ability of helicon plasmas to efficiently reach high electron densities has been known for nearly 30 years. Despite the ongoing research into the properties of helicon plasmas, especially the ionization mechanism itself, only certain aspects of the particle balance have been investigated. Specifically, the physical mechanism that causes the depletion of neutral atoms on axis leading an electron density limit is poorly understood. To shed light on this aspect of helicon plasmas, a systematic investigation of the particle balance was undertaken using laser induced fluorescence as the central diagnostic, aided by advanced atomic physics models, and a newly constructed RF compensated Langmuir probe. Establishing the strength and relative importance of the parallel and perpendicular particle fluxes, and by extension the particle sources and sink distributions, is particularly important.

The high spatial resolution and the ability to measure flow velocities made laser induced fluorescence an obvious choice for this work. In order to obtain both high accuracy and high precision, every aspect of the LIF process was scrutinized and uncertainties were reduced or eliminated where possible. To achieve flow velocity measurements with uncertainty less than 10 m/s, a new technique leveraging the symmetric energy splitting of the Zeeman effect was developed [49]. Using the midpoint of the $\sigma^+$ and $\sigma^-$ Zeeman groupings to assess Doppler shifts eliminated any requirement to measure the magnetic field strength at the measurement location and reduced the fitting uncertainty by 30%. Additionally, refinements to absolute wavelength references using molecular

iodine reduced the absolute velocity uncertainty from $\pm 800$ m/s to $\pm 7.2$ m/s. A new RF compensated Langmuir probe was built as the reference diagnostic and utilized to calibrate LIF intensity measurements with electron densities.

These diagnostic innovations enabled the parallel flux of ions and neutrals to be measured at several combinations of magnetic field strength and electron density. These measurements revealed strong axial ion fluxes between $3 \times 10^{20}$ m$^{-2}$s$^{-1}$ and $2.6 \times 10^{21}$ m$^{-2}$s$^{-1}$ leaving a central region of high electron density. Within the assumption of a 1D fluid model for mass and momentum conservation, these fluxes indicate the presence of an ion source rate between $6 \times 10^{20}$ m$^{-3}$s$^{-1}$ and $3.6 \times 10^{21}$ m$^{-3}$s$^{-1}$ located 1.2 meters downstream of the helicon antenna. Further downstream, 1.4 m behind the antenna, neutral argon LIF measurements revealed a region of strong neutral atom recycling at a boundary plate. Neutral LIF measurements also indicated that a neutral depletion region of up to 90% exists 1 m downstream of the antenna.

To validate the 1D particle balance assumption and investigate the role of radial refueling and exhaust, radial LIF measurements were made a several axial and radial positions. These measurements revealed that an outward radial ion flux of $4 \times 10^{20}$ m$^{-2}$s$^{-1}$ exists between 0.4 m and 0.8 m downstream of the antenna. Neutral LIF measurements in the same region indicated a radial inward flow of neutral atoms and further confirmed the axially hollow neutral density profile. These non-trivial radial ion fluxes and neutral flow velocities indicate that the applicability of a 1D particle balance is incomplete for regions close to the antenna, and a 2D model is necessary to capture the actual conditions much more accurately.

Combining the results of the axial and radial LIF measurements indicates a region between 1.0 m and 1.4 m downstream of the antenna where a strong linear relationship exists between electron density and magnetic field strength. The high density, ionization rate, and linear relationship

with magnetic field strength suggests the helicon wave RF energy is strongly damped in this region. Electron densities closer to the antenna exhibited asymptotic behavior, no further increase in density beyond 750 G, indicating poor coupling with the helicon wave.

These diagnostic advances have enabled a 1D particle balance to be experimentally constrained and established a baseline picture of the particle balance in the MARIA device. Neutral argon atoms sourced from the outer radius of the chamber flow towards the axis where they are quickly ionized. The newly created ions flow out of this region both axially and radially. The ions that flow along the axis encounter a dense region of neutral particles near the downstream boundary plate which sets up a region of high local recycling. An increased ionization rate between the high recycling region and antenna likely from damping of the helicon wave and a sufficient source of neutral atoms combine to produce the highest density of ions and electrons here.

The initial assumption of a 1D particle balance was shown to be partially correct. To further improve the investigation of a 2D particle balance, the resolution of radial LIF measurements must be increased. Additionally greater LIF signal to noise ratio is necessary to improve velocity measurements of the slow moving neutral atoms. While these improvements may not substantially change the qualitative understanding of the particle balance in the current configuration at MARIA, they will be important when assessing the impact of different vacuum pumping arrangements.

The close proximity of the axial recycling region near the boundary plate to the radial fueling and loss region near the antenna in MARIA is not a realistic arrangement for particle accelerator applications. To asses the performance of helicon plasmas in very low aspect ratio (radius/length) future accelerators like AWAKE, different vacuum pumping arrangements must be established. A flow through type arrangement in which the neutral gas is introduced upstream of the antenna and pumped away downstream will remove the high recycling region and enable the free streaming conditions downstream of the antenna to be further researched.

In any scenario, RF diagnostics in the form of B-dot or J-dot probes must be established at MARIA [35]. Doing so will confirm the location of greatest helicon wave damping. Combining such RF diagnostics with improved LIF capabilities would enable the ionization dynamics to be measured from both an RF and particle balance perspective for the first time.

## 7.1 Possibilities for Future Work

A particularly exciting, but at times frustrating feature of this work is all the avenues for additional exploration that show up. Most of these tangents were very interesting and staying focused was quite difficult at times. A few of these topics are introduced here along with some of the observations that lead to their discovery.

### 7.1.1 Possible Drift Waves and Instabilities

While investigating the operational parameter space on MARIA, radial Langmuir probe measurements were taken at a magnetic field strength of 700 G, with 700 W of RF heating power, and 1 mTorr of pre-plasma neutral fill pressure. Anomalously high electron temperatures were measured around 3 cm from the axis as seen in Figure 7.1. Further investigating this anomaly by measuring the ion saturation current in this region and the line integrated 442.6 nm Ar II emission line intensity indicated a density fluctuation with a frequency of approximately 3.6 kHz. The details of this oscillation were not further investigated in this work, as the majority of measurements were made at higher pressure where these oscillations did not occur. However, the location and frequency bear a striking resemblance to the drift waves studied in the VINETA helicon device by Schröder *et al* [69]. While not the principle aim of the research presented here, it appears that MARIA is perfectly capable of generating drift waves and perhaps other instabilities. The brief measurements made here also demonstrate that MARIA is sufficiently robust yet flexible that a wide range of plasma effects are able to be reliably measured. An important implication for future

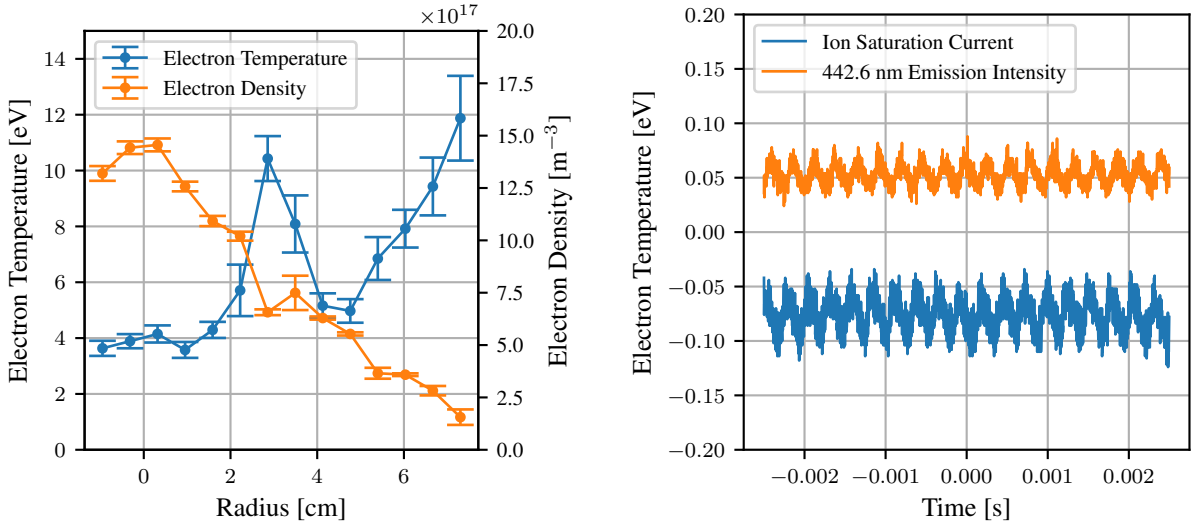


Figure 7.1: Taking radial Langmuir probe measurements with 1 mTorr fill pressure resulted in some strange results around 3 cm.

work with 2D momentum balance models is that the presence of drift waves indicates radial electric fields are contributing significantly to momentum transport [90]. These effects also raise the possibility that other transport mechanisms such as turbulence could also contribute significantly to radial transport.

### 7.1.2 Sputtering and Plasma Material Interactions

One observation that might be considered a great accomplishment in some devices but was an enormous problem in this work was sputtered metals. While setting up the LIF diagnostics to perform the particle flux measurements presented above a green tinted light was observed near the boundary plate. The green emission, shown in Figure 7.2, can be seen emerging from right on the axis of the device near the hole of the laser beam dump, and also where the flux of ions struck the boundary plate. This light was identified as coming from chromium atoms that had somehow been preferentially sputtered out of the stainless steel plate. No emission from iron, carbon, or any other constituent of stainless steel species was observed. The major problem with this sputtering

was that it re-deposited on the inside of the glass chamber within 100 cm of the plate. Over the course of a couple hours of intermittent operation the deposition layer got so thick that the chamber became almost completely opaque to plasma emission. This represented a significant problem for performing LIF measurements requiring days worth of continuous plasma operation. It turns out that chromium reacts well with dilute phosphoric acid and could be completely cleaned from the inside surface of the glass. Venting the chamber every few days to clean the glass of chromium would have been impractical. The stainless steel boundary plate was replaced with one made of pure molybdenum, which has a sputtering threshold of approximately 35 eV [91]. It was soon discovered the MARIA plasmas were even able to sputter molybdenum, and it too was redepositing on the glass in this region. This represented a much bigger problem given the extremely inert nature of molybdenum, even against such aggressive chemicals as nitric and hydrofluoric acid. LIF measurements were made with this boundary plate grounded and floating, and no change to the particle fluxes were measured. The work presented above was therefore all done with the boundary plate floating to prevent this sputtering issue. However, this exercise demonstrates the practicality of using MARIA as a high density, high particle flux, plasma source for performing divertor relevant plasma material interaction research. In fact, using helicon plasmas to perform this type of research is precisely the goal of the MPEX experiment at Oak Ridge National Laboratory [15].

### 7.1.3 Discharge Equilibrium at High RF Heating Power

With the arrival of sufficient cooling capacity to operate MARIA's RF system up to 10 kW CW (even 20 kW is currently available), an obvious progression is to extend this research to the several kW range of heating power. As mentioned in Section 6.1, the operating point of 700 W, 700 G, and 2.0 mTorr was experimentally found as a Goldilocks kind of operating point only by extensive systematic measurements. Much of this exploratory operation was done early on in parallel with developing the robust diagnostic capabilities presented in this thesis. Now that

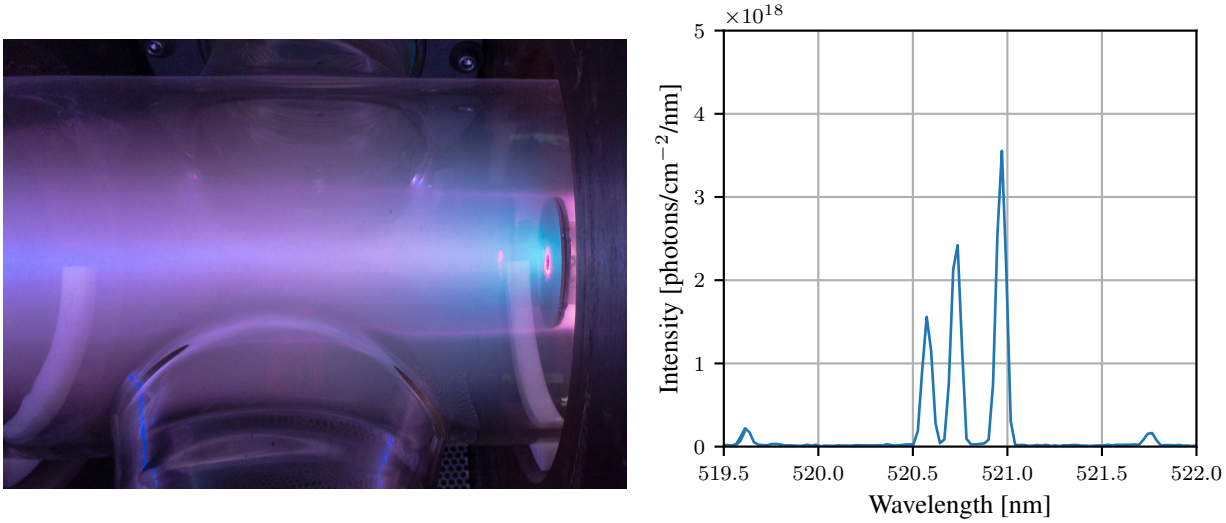


Figure 7.2: The appearance of the greenish light right near the boundary plate (left) was identified as chromium by the three distinct Cr I lines at 520.6 nm, 520.7 nm, and 521 nm (right).

adequate cooling and reliable diagnostics are in place, a systematic effort to discover optimal set of parameters to operate at high power should be initiated. Near the end of the research presented here, during the commissioning of the new cooling system, MARIA was operated at 4 kW for several minutes. Simply increasing the RF power was discovered to have rather unintended effects. The first observed effect was that around 1-1.5 kW at 2.0 mTorr, the plasma began to flicker and become unstable. It appeared to drop completely out of the nice helicon mode for a couple milliseconds. The dip in the 442.6 nm argon ion emission intensity shown in Figure 7.3 was captured during one of these abrupt changes in the plasma emission. It is believed that this apparent ion density collapse is a result of the recycling neutral gas being unable to sustain the ionization rate necessary for that particular helicon wave to propagate, thus resulting in a collapse of the ionization rate and electron density. After the plasma has collapsed and the neutral gas is able to redistribute, the necessary ionization rate can be reestablished and the helicon mode propagates again.

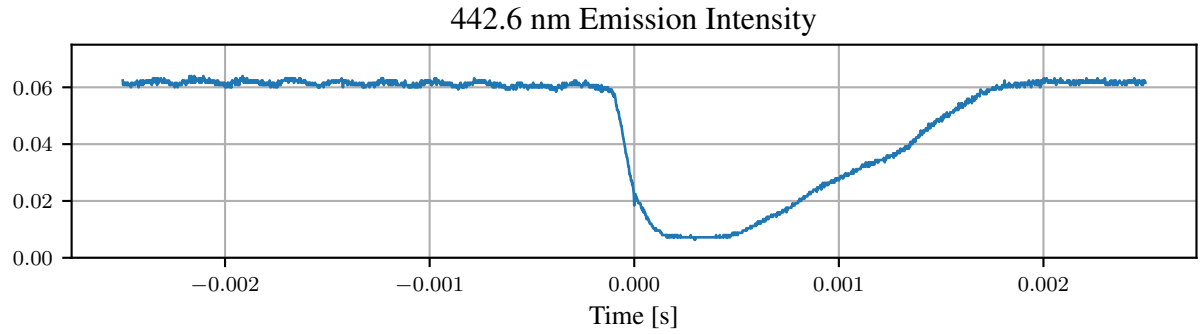


Figure 7.3: At neutral fill pressure of 2.0 mTorr and 1.5 kW of RF heating power, the ion density would periodically collapse for a couple milliseconds before being reestablished.

The particle balance work described in this thesis then suggests that pushing the RF heating power above 1.5 kW requires a suitable increase to the neutral fueling rate. The only control currently available to achieve this is to increase the neutral fill gas pressure. By closing a gate valve in front of the vacuum pump, the fill pressure was increased to 25 mTorr. The pressure increase was able to support RF heating power up to 5 kW, limited now by the existing air cooling for the antenna. However, the visual characteristic of the plasma is entirely different. The picture on the left in Figure 7.4 is a typical plasma diagnosed in this work with neutral fill pressure of 2.0 mTorr, 900 G magnetic field strength, and 700 W of RF heating. The characteristic blue core, which comes from argon ion emission, extends nearly the full length of the plasma chamber only tapering off near the boundary plate just off the left side of the image. The picture on the right is at the same magnetic field strength, neutral pressure of 25 mTorr, and 5 kW of RF heating power. A bright blue core still develops just down stream of the antenna. However, the axial extent of this blue core is dramatically reduced, with the plasma all but vanishing only halfway down the plasma chamber. A hypothesis to explain this observation is that ions created in this high pressure plasma flow quickly into a high density cloud of neutral atoms, lose momentum through ion-neutral collisions, and are lost quickly through recombination. The ability to generate these

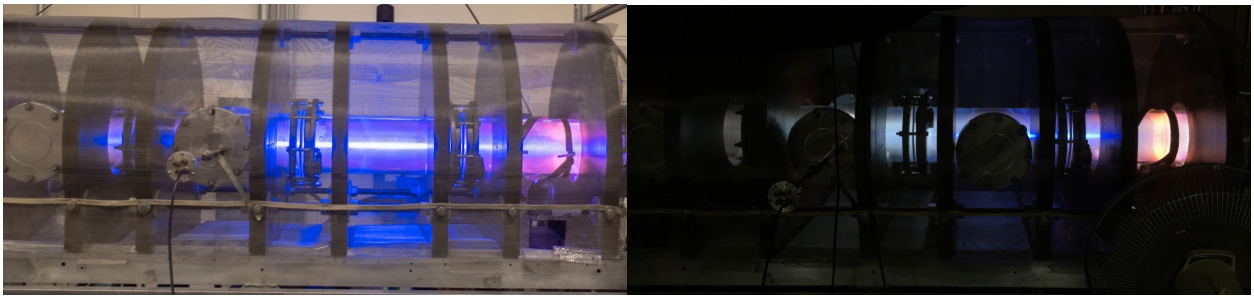

Figure 7.4: (left) Typical appearance of the plasma at 900 G, 700 W, and 2.0 mTorr. (Right) By increasing the neutral fill pressure to 25 mTorr RF heating powers in the range of 4 kW became sustainable. However, the generated plasma was quickly lost as it flowed into a high density cloud of neutrals.

high power plasmas has only recently become available, and more infrastructure is still needed to reliably sustain such a plasma. This operating regime is the logical continuation of the work that began here.

# Appendix A: Spectrometer Intensity Calibration

The line ratio spectroscopy method can only succeed if accurate line intensities can be acquired. To achieve this, a calibration routine described by NIST to absolutely calibrate the spectrometer was undertaken [92].

To start, it was very important to make sure that the linear fiber array was aligned with the entrance slit of the spectrometer, that the fiber ends were close to the entrance slit, and that the camera was properly rotated and focused.

With the spectrometer propery alinged, an initial calibration was performed. The calibration source was an OL-455-S high intensity integrating sphere from Optronic Laboratories. The source is thermally stabilized and actively controlled to maintain a spectral radiance uncertainty of $\pm 2\%$ relative to NIST. The reference spectrum is shown in Figure A.1. A calibration spectrum of the source was taken using a custom written MATLAB script which used an API for the spectrometer control software.

As a result of the spectrometer dispersion, each frame of the CCD only covered about 20 nm. To acquire a full spectrum from 350 nm to 933 nm, a step-and-glue technique was used. The steo-and-glue process involved acquiring an image from the CCD, slewing the grating to the next point, and acquiring another image from the CCD. In all 31 frames were needed to cover the full wavelength range. Each frame overlapped the previous one by about 1 nm.

Instead of generating a single overall calibration curve, curves for each frame of the full spectrum were generated. Problems in the calibration process could be detected quickly by observing emission that fell in the overlap region. The calibrated intensity of a line in the upper part of one frame should be identical to the calibrated intensity of the same line captured in the lower part of

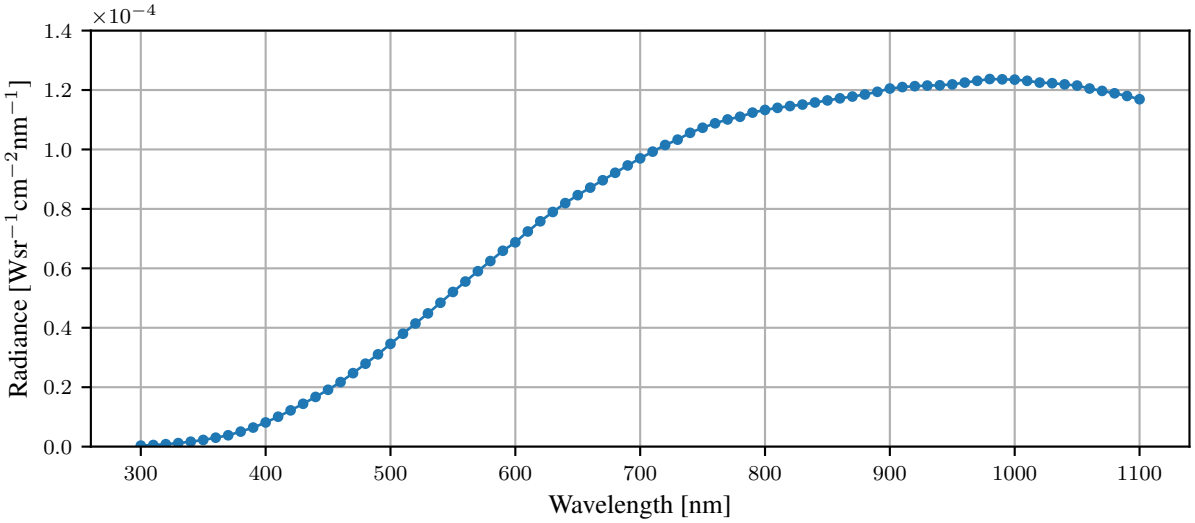


Figure A.1: The calibrated reference spectrum provided for the OL455 calibration source.

the next frame. The calibration curve was calculated using Equation A.1.

$$C_i = \frac{I_{ref}}{I_{c,i} - I_{b,i}} \tag{A.1}$$

where $C_i$ is the calibration data for the $i_{th}$ frame, $I_{ref}$ is the reference intensity shown in Figure A.1, $I_{c,i}$ is the measured intensity of the $i_{th}$ frame, and $I_{b,i}$ is the background intensity for the $i_{th}$ frame.

By calculating the calibration curve as in Equation A.1, an acquired spectrum can be simply calibrated by Equation A.2. A typical calibration curve is shown in Figure A.2a. The inverse of the calibration curve, shown in Figure A.2b, is a measure of the light sensitivity of the complete optical system. A particularly prominent feature of the sensitivity curve are the jagged peaks throughout the curve. These are a result of the variation in light sensitivity across the CCD chip. Part of this variability is due to astigmatism introduced by the Czerny-Turner spectrometer design.

$$I_i = (I_i - I_{b,i})C_i \tag{A.2}$$

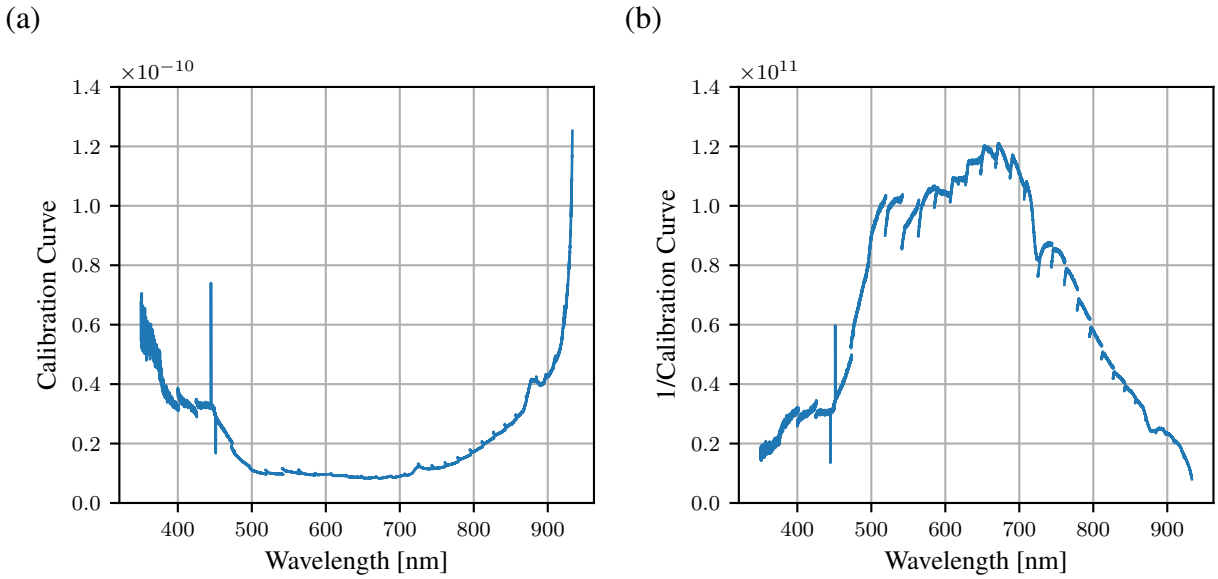


Figure A.2: a.) A typical calibration curve to absolutely calibrate spectra. b.) The inverse calibration curve gives a measure of the light sensitivity of the spectrometer optics. The jagged features indicate the variable sensitivity across the CCD chip.

The astigmatism is shown in Figure A.3. In this case, the region of sharpest focus was as higher wavelength, but was ultimately placed nearer to the center by improving the overall alignment. The distance between the fiber array and the entrance slit knife edges played a significant role in placing the region of sharpest focus in the center of the CCD. Minimizing the negative impact of astigmatism also played a huge role in eliminating cross-talk between channels.

The OL-455-S calibration source was only on loan for a short period of time. To facilitate the need to recalibrate the spectrometer in the event the alignment was bumped, which happened periodically, a secondary source was calibrated and a reference spectrum determined while the OL-455-S source was available for comparison. The secondary source was an SL-201 quartz tungsten-halogen temperature stabilized source from ThorLabs.

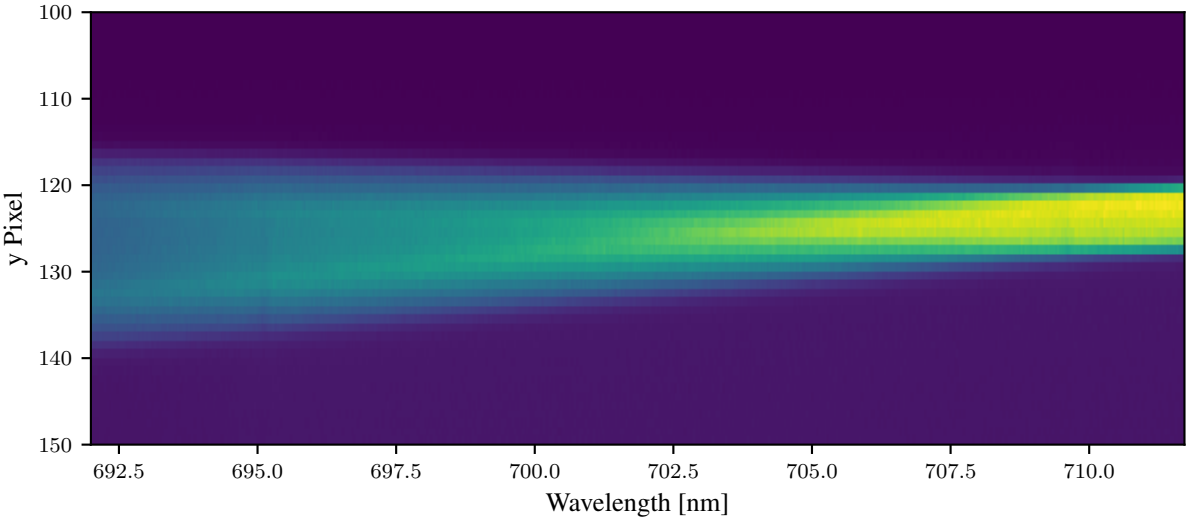


Figure A.3: The astigmatism introduced by the spectrometer design meant the focus sharpness varied across the CCD.

The acquired spectrum, shown in Figure A.4, was fit to Equation A.3 in a two step process described by NIST [92].

$$E_\lambda = (A_0 + A_1 \cdot \lambda + \cdots + A_5 \cdot \lambda^n) \cdot \lambda^{-5} \cdot \exp(a + b/\lambda) \tag{A.3}$$

where $A_0 \ldots A_n$ are polynomial fitting coefficients, $\lambda$ is the wavelength, and $a$ and $b$ are exponential fitting coefficients.

First, the an intermediate spectrum of the form $\ln(I \cdot \lambda^5) = a + b\lambda$ was fitted in a non-linear least squares sense, with a weighting of 1, to determine the coefficients $a$ and $b$. The acquired spectrum was then fit using Equation A.3 using a weighting of $1/I^2$. NIST claims that irradiance values prediced by Equation A.3 have an uncertainty in the range of 0.5%.

In this work, the residual error between the fit and the spectrum was less than 10% above 400 nm, and typically less than 3%. Propagating the error through from the stated reference spectrum uncertainty of 2% to the spectrum shown in Figure A.4 yields an overall uncertainty in the fitted

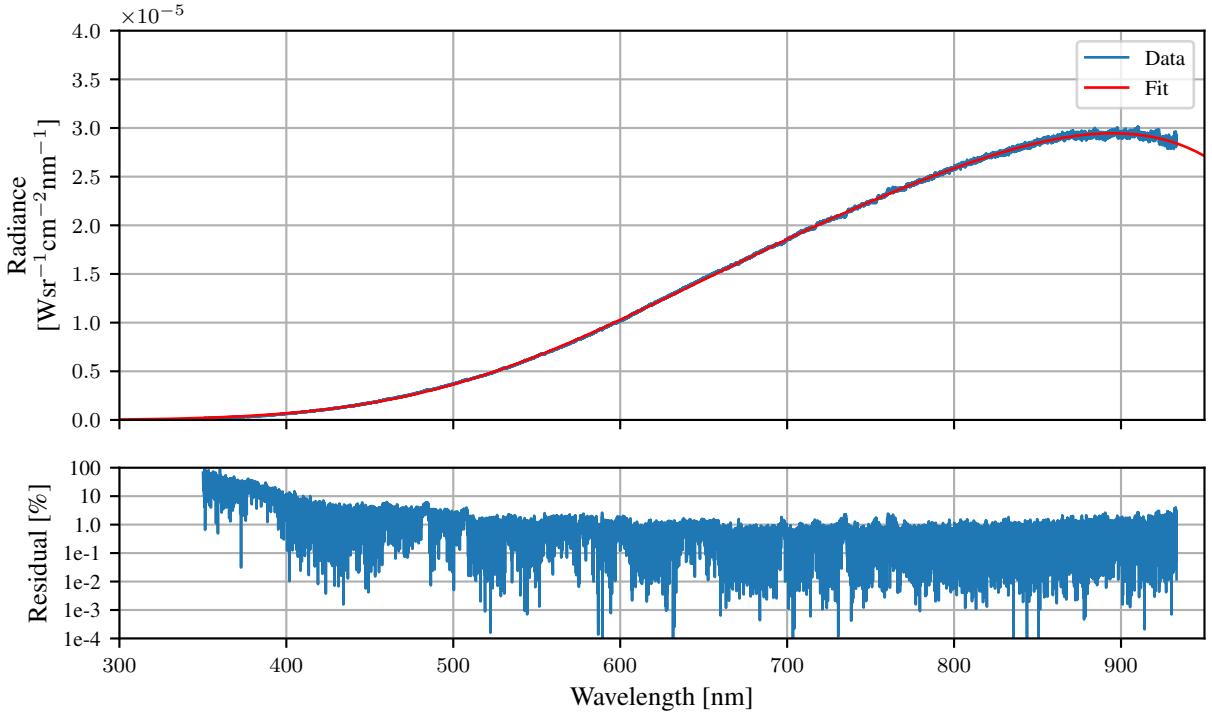


Figure A.4: While the OL-455-S source was available, and the spectrometer was newly calibrated, the calibration was transferred to a ThorLabs SL-201 source by fitting the spectrum with Equation A.3. NIST claims the fit is usually good to within 0.5%. Above 400 nm, the residual error is less than 10% and more typically below 3%.

reference curve is about 10%. For the the purposes of this research, this uncertainty is acceptable.

The final fitted coefficients are:

$$
\begin{aligned}
A_0 &= 22.87 \\
A_1 &= -0.1719 \\
A_2 &= 5.29 \times 10^{-4} \\
A_3 &= -8.00 \times 10^{-7} \\
A_4 &= 5.96 \times 10^{-10} \\
A_5 &= -1.75 \times 10^{-13} \\
a &= 29.97 \\
b &= -5707
\end{aligned}
\tag{A.4}
$$

# Appendix B: Line Intensity Calculation and Uncertainty

Following from Appendix A, the calibrated spectra can then be used to calculate the calibrated intensity of individual emission lines. A typical absolutely calibrated spectrum is shown in Figure B.1. For a typical spectrum on the order of 155 individual emission lines were detected.

Peak detection was carried out by a custom written MATLAB script. For each detected emission line, the total intensity was calculated by integrating over wavelength using trapezoidal integration. Since the absolute calibration and associated uncertainty was already performed in calibrating the spectrum, the integrated line intensity will already be calibrated and the uncertainty is easily propagated.

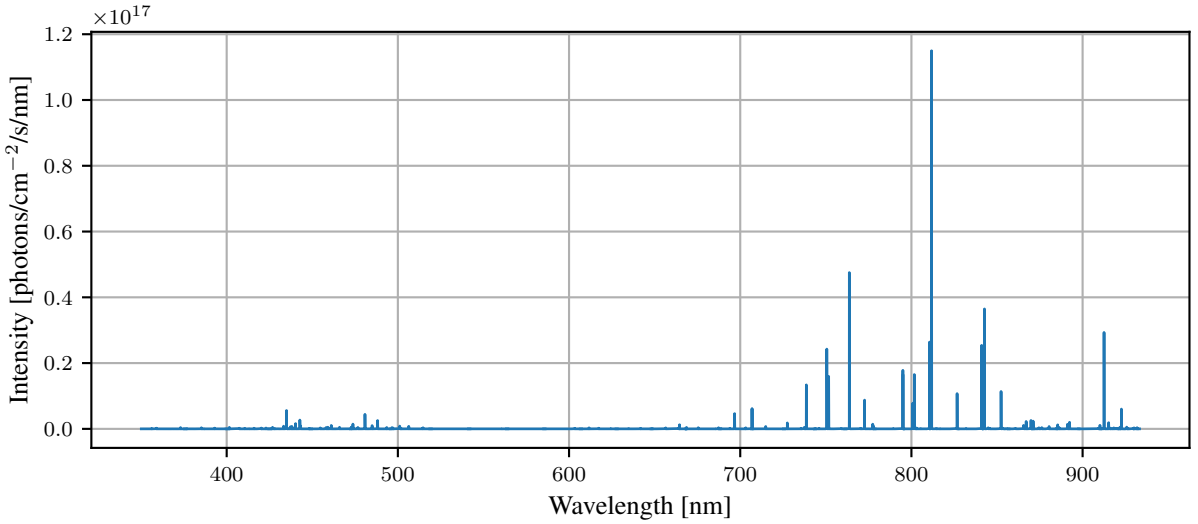


Figure B.1: A typical absolutely calibrated spectrum from MARIA.

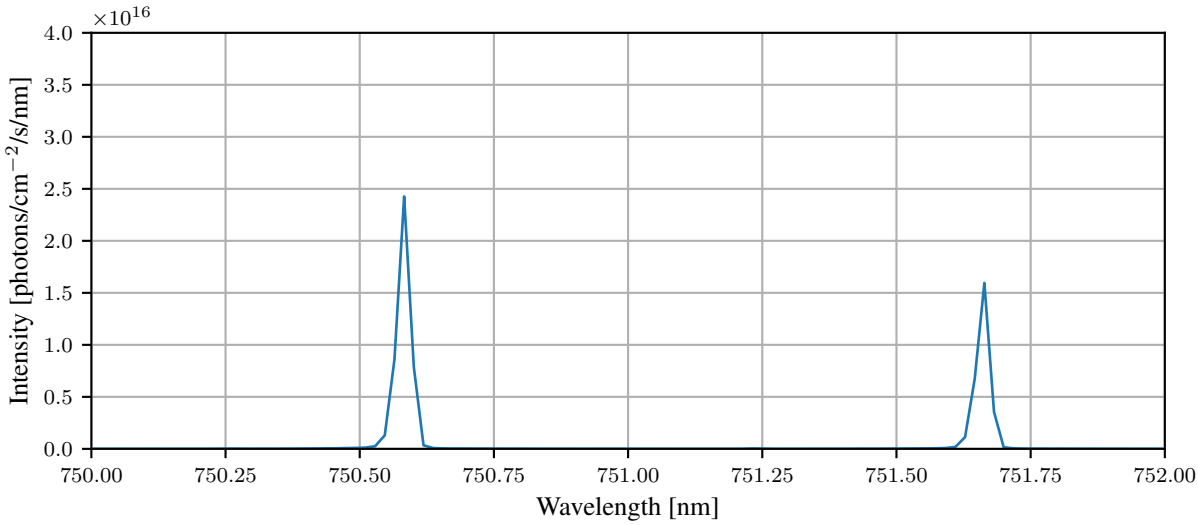


Figure B.2: Typical shape of emission lines detected in the calibrated spectrum.

## References


[1] B Buttenschön, N Fahrenkamp, and O Grulke. "A High Power, High Density Helicon Discharge for the Plasma Wakefield Accelerator Experiment AWAKE". In: *Plasma Phys. Control. Fusion* 60.7 (2018), p. 075005. DOI: 10.1088/1361-6587/aac13a.

[3] R. Prater et al. "Application of Very High Harmonic Fast Waves for Off-Axis Current Drive in the DIII-D and FNSF-AT Tokamaks". In: *Nucl. Fusion* 54.8 (2014), p. 083024. DOI: 10.1088/0029-5515/54/8/083024.

[4] B. Buttenschön et al. "A Helicon Plasma Source as a Prototype for a Proton-Driven Plasma Wakefield Accelerator". In: *40th EPS Conference on Plasma Physics*. Espoo, Finland, 2013.

[5] Allen Caldwell et al. "Proton-Driven Plasma-Wakefield Acceleration". In: *Nat. Phys.* 5.May (2009), pp. 363–367. DOI: 10.1038/nphys1248.

[6] Eric Esarey et al. "Overview of Plasma-Based Accelerator Concepts". In: *IEEE Trans. Plasma Sci.* 24.2 (1996), pp. 252–288. DOI: 10.1109/27.509991.

[7] J B Rosenzweig et al. "Acceleration and Focusing of Electrons in Two-Dimensional Nonlinear Plasma Wake Fields". In: *Phys. Rev. - At. Mol. Opt. Phys.* 44.10 (1991), R6189–R6192. DOI: 10.1103/PhysRevA.44.R6189.

[8] Isaac D Sudit and Francis F Chen. "Discharge Equilibrium of a Helicon Plasma". In: *Plasma Sources Sci. Technol.* 5.1 (1999), pp. 43–53. DOI: 10.1088/0963-0252/5/1/006.

[9] M. D. Carter et al. "Comparing Experiments with Modeling for Light Ion Helicon Plasma Sources". In: *Phys. Plasmas* 9.12 (2002), pp. 5097–5110. DOI: 10.1063/1.1519539.

[10] X. M. Guo et al. "Helicon Experiments and Simulations in Nonuniform Magnetic Field Configurations". In: *Phys. Plasmas* 6.8 (Aug. 1999), pp. 3400–3407. DOI: 10.1063/1.873580.

[11] David G Miljak and Francis F Chen. “Density Limit in Helicon Discharges”. In: *Plasma Sources Sci. Technol.* 7.4 (1999), pp. 537–549. DOI: 10.1088/0963-0252/7/4/011.

[12] R. M. Magee et al. “Neutral Depletion and the Helicon Density Limit”. In: *Phys. Plasmas* 20.12 (2013), pp. 2–6. DOI: 10.1063/1.4849376.

[13] F. Effenberg et al. “Investigation of 3D Effects on Heat Fluxes in Performance-Optimized Island Divertor Configurations at Wendelstein 7-X”. In: *Nucl. Mater. Energy* 18 (2019), pp. 262–267. DOI: https://doi.org/10.1016/j.nme.2019.01.006.

[14] A R Field et al. “Dynamics and Stability of Divertor Detachment in H-Mode Plasmas on JET”. In: *Plasma Phys. Control. Fusion* 59.9 (July 2017), p. 095003. DOI: 10.1088/1361-6587/aa764c.

[15] J. Rapp et al. “The Material Plasma Exposure eXperiment MPEX: Pre-Design, Development and Testing of Source Concept”. In: *Proc. - Symp. Fusion Eng.* 2016-May (2016), pp. 1–8. DOI: 10.1109/SOFE.2015.7482351.

[16] Juergen Rapp et al. “Operational Domain of Proto-MPEX”. In: *Proceedings of the 13th International Symposium on Fusion Nuclear Technology (ISFNT-13)*. Vol. 136. Kyoto Japan: Fusion Engineering and Design, 2018, pp. 712–716. DOI: 10.1016/j.fusengdes.2018.03.064.

[17] Francis F. Chen. “Langmuir Probe Analysis for High Density Plasmas”. In: *Phys. Plasmas* 8.6 (2001), pp. 3029–3041. DOI: 10.1063/1.1368874.

[18] P. C. Stangeby. “Determination of Te from a Langmuir Probe in a Magnetic Field by Directly Measuring the Probe’s Sheath Drop Using a Pin-Plate Probe”. In: *Plasma Phys. Control. Fusion* 37.11 (1995), pp. 1337–1347. DOI: 10.1088/0741-3335/37/11/011.

[19] Annemie Bogaerts, Renaat Gijbels, and Jaroslav Vlcek. “Collisional-Radiative Model for an Argon Glow Discharge”. In: *J. Appl. Phys.* 84.1 (1998), p. 121. DOI: 10.1063/1.368009.

[20] Amy M. Keesee and Earl E. Scime. “Neutral Argon Density Profile Determination by Comparison of Spectroscopic Measurements and a Collisional-Radiative Model (Invited)”. In: *Rev. Sci. Instrum.* 77.10 (2006). DOI: 10.1063/1.2219440.

[21] J. M. Muñoz Burgos et al. “Hybrid Time Dependent/Independent Solution for the He i Line Ratio Temperature and Density Diagnostic for a Thermal Helium Beam with Applications in the Scrape-off Layer-Edge Regions in Tokamaks”. In: *Phys. Plasmas* 19.1 (2012). DOI: 10.1063/1.3672230.

[22] J. M. Muñoz Burgos et al. “Implementation of a New Atomic Basis for the He i Equilibrium Line Ratio Technique for Electron Temperature and Density Diagnostic in the SOL for H-Mode Plasmas in DIII-D”. In: *J. Nucl. Mater.* 415.1 SUPPL (2011), pp. 1155–1158. DOI: 10.1016/j.jnucmat.2010.11.052.

[23] E. A. Unterberg et al. “HELION: A Helium Line-Ratio Spectral-Monitoring Diagnostic Used to Generate High Resolution Profiles near the Ion Cyclotron Resonant Heating Antenna on TEXTOR”. In: *Rev. Sci. Instrum.* 83.10 (2012), p. 10D722.

[24] Joseph Fraunhofer. “Bestimmung Des Brechungs- Und Des Farben-Zerstreuungs - Vermögens Verschiedener Glasarten, in Bezug Auf Die Vervollkommnung Achromatischer Fernröhre”. In: *Mem. R. Acad. Sci. Munich* 5 (1817), pp. 193–226.

[25] G. D. Severn, D. A. Edrich, and R. McWilliams. “Argon Ion Laser-Induced Fluorescence with Diode Lasers”. In: *Rev. Sci. Instrum.* 69.1 (1998), p. 10. DOI: 10.1063/1.1148472.

[26] Yuriko Tanida, Daisuke Kuwahara, and Shunjiro Shinohara. “Spatial Profile of Ion Velocity Distribution Function in Helicon High-Density Plasma by Laser Induced Fluorescence

Method". In: *Trans. Jpn. Soc. Aeronaut. Space Sci. Aerosp. Technol. Jpn.* 14.30 (2016), Pb_7–Pb_12. DOI: 10.2322/tastj.14.Pb_7.

[27] D. A. Edrich, R. McWilliams, and N. S. Wolf. "Single Beam Laser Induced Fluorescence Technique for Plasma Transport Measurements". In: *Rev. Sci. Instrum.* 67.8 (1996), pp. 2812–2817. DOI: 10.1063/1.1147111.

[28] M E Galante, R M Magee, and E E Scime. "Two Photon Absorption Laser Induced Fluorescence Measurements of Neutral Density in a Helicon Plasmaa)". In: *Phys. Plasmas* 21.5 (May 2014), p. 055704. DOI: 10.1063/1.4873900.

[29] Amy M. Keesee, Earl E. Scime, and Robert F. Boivin. "Laser-Induced Fluorescence Measurements of Three Plasma Species with a Tunable Diode Laser". In: *Rev. Sci. Instrum.* 75.10 (Oct. 2004), pp. 4091–4093. DOI: 10.1063/1.1787166.

[30] U Czarnetzki, D Luggenhölscher, and H F Döbele. "Space and Time Resolved Electric Field Measurements in Helium and Hydrogen RF-Discharges". In: *Plasma Sources Sci. Technol.* 8.2 (1999), pp. 230–248. DOI: 10.1088/0963-0252/8/2/004.

[31] Francis F Chen. "Helicon Discharges and Sources: A Review". In: *Plasma Sources Sci. Technol.* 24.1 (Jan. 2015), p. 014001. DOI: 10.1088/0963-0252/24/1/014001.

[32] B. Davies. "Helicon Wave Propagation: Effect of Electron Inertia". In: *J. Plasma Phys.* 4.01 (1970), p. 43. DOI: 10.1017/S0022377800004803.

[33] R T S Chen et al. "Experimental Studies of Multimode Helicon Plasma Waves". In: *Plasma Sources Sci. Technol.* 4.3 (Aug. 1995), pp. 337–344. DOI: 10.1088/0963-0252/4/3/003.

[34] Francis F. Chen and Donald Arnush. "Generalized Theory of Helicon Waves. I. Normal Modes". In: *Phys. Plasmas* 4.9 (1997), pp. 3411–3421. DOI: 10.1063/1.872483.

[35] D. D. Blackwell et al. “Evidence for Trivelpiece-Gould Modes in a Helicon Discharge”. In: *Phys. Rev. Lett.* 88.14 (2002), p. 145002. DOI: 10.1103/PhysRevLett.88.145002.

[36] Michael Krämer and Kari Niemi. “Helicon Mode Formation and Rf Power Deposition in a Helicon Source”. In: *49th Annual Meeting of the Division of Plasma Physics*. Vol. 52. 2007, GM5.00005.

[37] Robert Chen and Noah Hershkowitz. “Multiple Electron Beams Generated by a Helicon Plasma Discharge”. In: *Phys. Rev. Lett.* 80.21 (1998), pp. 4677–4680. DOI: 10.1103/PhysRevLett.80.4677.

[38] Francis F. Chen. “Physics of Helicon Discharges”. In: *Phys. Plasmas* 3.5 (1996), pp. 1783–2797. DOI: 10.1063/1.871712.

[39] David D Blackwell and Francis F Chen. “Time-Resolved Measurements of the Electron Energy Distribution Function in a Helicon Plasma”. In: *Plasma Sources Sci. Technol.* 10.2 (2001), pp. 226–235. DOI: 10.1088/0963-0252/10/2/312.

[40] M Umair Siddiqui et al. “Electron Heating and Density Production in Microwave-Assisted Helicon Plasmas”. In: *Plasma Sources Sci. Technol.* 24.3 (2015), p. 034016.

[41] Carsten Lechte, Jennifer Stöber, and Ulrich Stroth. “Plasma Parameter Limits of Magnetically Confined Low Temperature Plasmas from a Combined Particle and Power Balance”. In: *Phys. Plasmas* 9.6 (June 2002), pp. 2839–2846. DOI: 10.1063/1.1467928.

[42] R. H. Goulding et al. “Progress in the Development of a High Power Helicon Plasma Source for the Materials Plasma Exposure Experiment”. In: *Fusion Sci. Technol.* 72.4 (Sept. 2017), pp. 588–594. DOI: 10.1080/15361055.2017.1352429.

[43] A Kramida et al. *NIST Atomic Spectra Database (Version 5.6.1)*. 2018. URL: https://dx.doi.org/10.18434/T4W30F.

[44] David J. Griffiths. *Introduction to Quantum Mechanics*. 2nd. Cabridge University Press, 2017. ISBN: 978-1-107-17986-8.

[45] Wolfgang Demtröder. *Laser Spectroscopy Vol. 1: Basic Principles*. Vol. 1. 2008. ISBN: 978-3-540-73415-4. DOI: 10.1007/978-3-540-73418-5.

[46] A. Einstein. "Zur Quantentheorie Der Strahlung". In: *Phys. Z.* 18 (1917), pp. 121–128.

[47] Tilmann Lunt, Gerd Fussmann, and Ole Waldmann. "Experimental Investigation of the Plasma-Wall Transition". In: *Phys. Rev. Lett.* 100.17 (May 2008), p. 175004. DOI: 10.1103/PhysRevLett.100.175004.

[48] Daisuke Kuwahara et al. "Development of Ar I and Ar II Measuring System Using Laser-Induced Fluorescence Methods in High-Density Helicon Plasma". In: *Plasma Fusion Res.* 10 (2015), p. 3401057. DOI: 10.1585/pfr.10.3401057.

[49] J. Green et al. "Exploiting Zeeman Effect Symmetries to Measure Particle Velocities in Magnetized Plasmas". In: *Meas. Sci. Technol.* 30.5 (2019), p. 055202. DOI: 10.1088/1361-6501/ab0e90.

[50] Irving Langmuir and H. M. Mott-Smith. "The Theory of Collectors in Gaseous Discharges". In: *Phys. Rev.* 28.4 (1926), pp. 727–763. DOI: 10.1103/PhysRev.28.727.

[51] Noah Hershkowitz. "How Langmuir Probes Work". In: *Plasma Diagnostics, Discharge Parameters and Chemistry*. Academic Press, Inc, 1989. ISBN: 978-1-4832-0281-5.

[52] Ira B Bernstein and Irving N Rabinowitz. "Theory of Electrostatic Probes in a Low-Density Plasma". In: 2.2 (1959), pp. 112–121. DOI: 10.1063/1.1705900.

[53] James G Laframboise. *Theory of Spherical and Cylindrical Langmuir Probes in a Collisionless, Maxwellian Plasma at Rest*. Tech. rep. Toronto: University of Toronto Institute for Aerospace Studies, 1967.

[54] Francis F Chen. “Langmuir Probe Measurements in the Intense RF Field of a Helicon Discharge”. In: *Plasma Sources Sci. Technol.* 21.5 (Oct. 2012), p. 055013. DOI: 10.1088/0963-0252/21/5/055013.

[55] Francis F. Chen, John D. Evans, and Wade Zawalski. “Calibration of Langmuir Probes against Microwaves and Plasma Oscillation Probes”. In: *Plasma Sources Sci. Technol.* 21.5 (2012), p. 055002. DOI: 10.1088/0963-0252/21/5/055002.

[56] G Kirchhoff. “Ueber Das Verhältniss Zwischen Dem Emissionsvermögen Und Dem Absorptionsvermögen Der Körper Für Wärme Und Licht”. In: *Ann. Phys. Chem.* 185.2 (1860), pp. 275–301. DOI: 10.1002/andp.18601850205.

[57] K. Verhaegh et al. “Spectroscopic Investigations of Divertor Detachment in TCV”. In: *Nucl. Mater. Energy* 12 (2017), pp. 1112–1117. DOI: 10.1016/j.nme.2017.01.004. arXiv: 1607.04539.

[58] John B Boffard et al. “Argon 420.1-419.8 Nm Emission Line Ratio for Measuring Plasma Effective Electron Temperatures”. In: *J. Phys. Appl. Phys.* 45.4 (2012), p. 045201. DOI: 10.1088/0022-3727/45/4/045201.

[59] H. P. Summers. *The ADAS User Manual, Version 2.6*. 2004. URL: http://www.adas.ac.uk.

[60] John B Boffard et al. “Measurement of Electron-Impact Excitation Cross Sections out of Metastable Levels of Argon and Comparison with Ground-State Excitation”. In: *Phys. Rev. A* 59.4 (1999). DOI: 10.1103/PhysRevA.59.2749.

[61] C P Ballance et al. “Electron-Impact Ionization of Argon Using the R-Matrix with a Pseudo-States Method”. In: *J. Phys. B At. Mol. Opt. Phys.* (2007). DOI: 10.1088/0953-4075/40/3/F01.

[62] N Ivan Arnold. “An Investigation into the Role of Metastable States on Excited Populations of Weakly Ionized Argon Plasmas, with Applications for Optical Diagnostics”. PhD thesis. Auburn University, 2017.

[63] E.U. Condon and G.H Shortley. *Atomic Spectra*. New York: Cambridge University Press, 1959. ISBN: 978-0-521-04713-5.

[64] David A Edrich. “Particle and Wave Scattering from Density Fluctuations”. PhD thesis. University of California - Irvine, 1995. URL: https://search.proquest.com/docview/304173163.

[65] M. Umair Siddiqui et al. “Direct Measurements of Ion Dynamics in Collisional Magnetic Presheaths”. In: *Phys. Plasmas* 21.10 (Oct. 2014), p. 102103. DOI: 10.1063/1.4897173.

[66] T.M.L van Ruremonde. *Plasma Dispersion Behavior of the MARIA Helicon Device*. Tech. rep. UW-Madison Department of Engineering Physics, 2017.

[67] Hyun-Jong Woo et al. “A Newly Calibrated Laser-Induced Fluorescence ( LIF ) System for Ar Ions with a Single Tunable Diode Laser”. In: *J. Korean Phys. Soc.* 48.2 (2006), pp. 260–265. URL: https://escholarship.org/uc/item/1h74s201.

[68] I D Sudit and F F Chen. “RF Compensated Probes for High-Density Discharges”. In: *Plasma Sources Sci. Technol.* 3.2 (May 1994), pp. 162–168. DOI: 10.1088/0963-0252/3/2/006.

[69] Christiane Schröder et al. “Drift Waves in a High-Density Cylindrical Helicon Discharge”. In: *Phys. Plasmas* 12.4 (Apr. 2005), p. 042103. DOI: 10.1063/1.1864076.

[70] Yung-Ta Sung, Yan Li, and John E. Scharer. “Fast, Hot Electron Production and Ion Acceleration in a Helicon Inductive Plasma”. In: *Phys. Plasmas* 23.9 (Sept. 2016), p. 092113. DOI: 10.1063/1.4962758.

[71] Douglas Palmer and Mitchell Walker. “Operation of an Annular Helicon Plasma Source”. In: *J. Propuls. Power* 25.5 (2012), pp. 1013–1019. DOI: 10.2514/1.41403.

[72] V. I. Demidov et al. “Probe Measurements of Electron Energy Distributions in a Strongly Magnetized Low-Pressure Helium Plasma”. In: *Phys. Plasmas* 6.1 (1999), pp. 350–358. DOI: 10.1063/1.873288.

[73] Tsv K Popov et al. “Advances in Langmuir Probe Diagnostics of the Plasma Potential and Electron-Energy Distribution Function in Magnetized Plasma”. In: *Plasma Sources Sci. Technol.* 25.3 (2016), p. 033001. DOI: 10.1088/0963-0252/25/3/033001.

[74] M. Umair Siddiqui. “Presheath and Double Layer Structures in an Argon Helicon Plasma Source”. PhD thesis. University of Wisconsin - Madison, 2014.

[75] Christian M. Franck, Olaf Grulke, and Thomas Klinger. “Mode Transitions in Helicon Discharges”. In: *Phys. Plasmas* 10.1 (2003), pp. 323–325. DOI: 10.1063/1.1528903.

[76] H P Summers and M B Hooper. “On Radiative Power from Impurities in Plasmas”. In: *Plasma Phys.* 25.12 (1983), pp. 1311–1344. DOI: 10.1088/0032-1028/25/12/303.

[77] a M Keesee and E E Scime. “Neutral Density Profiles in Argon Helicon Plasmas”. In: *Plasma Sources Sci. Technol.* 16.4 (2007), pp. 742–749. DOI: 10.1088/0963-0252/16/4/008.

[78] L Liard, A Aanesland, and P Chabert. “Dynamics of Neutral Gas Depletion Investigated by Time- and Space-Resolved Measurements of Xenon Atom Ground State Density”. In: *J. Phys. Appl. Phys.* 45.23 (2012), p. 235201. DOI: 10.1088/0022-3727/45/23/235201.

[79] S. I. Braginskii. “Transport Processes in a Plasma”. In: *Rev. Plasma Phys.* 1 (1965), p. 205.

[80] S. Chapman and T. G. Cowling. *The Mathematical Theory of Non-Uniform Gases*. 3rd. Cambridge University Press, 1970.

[81] Peter Stangeby. *The Plasma Boundary of Magnetic Fusion Devices*. Publication Title: Plasma Physics and Controlled Fusion. Institute of Physics Publishing, 2000. ISBN: 0-7503-0559-2.

[82] D. D. Ryutov. "Geometrical Properties of a "snowflake" Divertor". In: *Phys. Plasmas* 14.6 (2007), p. 064502. DOI: 10.1063/1.2738399.

[83] M. Kotschenreuther et al. "On Heat Loading, Novel Divertors, and Fusion Reactors". In: *Phys. Plasmas* 14.7 (2007), p. 072502. DOI: 10.1063/1.2739422.

[84] P. M. Valanju et al. "Super-X Divertors and High Power Density Fusion Devices". In: *Phys. Plasmas* 16.5 (2009), p. 056110. DOI: 10.1063/1.3110984.

[85] D Schnack. *Lectures in Magnetohydrodynamics: With an Appendix on Extended MHD*. 2009. ISBN: 3-642-00687-6 978-3-642-00687-6.

[86] James D. Callen, Kyle J. Bunkers, and Jeffrey Kollasch. *UW-Madison NE 725, Plasma Kinetic Theory, Course Notes*. 2015.

[87] M. S. Pindzola, D. C. Griffin, and C Bottcher. "Electron-Ion Collisions in the Average-Configuration Distorted-Wave Approximation". In: *Atomic Processes in Electron-Ion and Ion-Ion Collisions*. Vol. 145. NATO ASI Series (Series B: Physics). Boston, MA: Springer, 1986. ISBN: 978-1-4684-5226-6.

[88] J. V. Jovanović, S. B. Vrhovac, and Z. Lj Petrović. "Momentum Transfer Theory of Ion Transport under the Influence of Resonant Charge Transfer Collisions: The Case of Argon and Neon Ions in Parent Gases". In: *Eur. Phys. J. D* 21.3 (2002), pp. 335–342. DOI: 10.1140/epjd/e2002-00199-6.

[89] R Prater et al. *Helicon Current Drive for the DIII-D Tokamak*. Tech. rep. Publication Title: General Atomics Report GA-A27841. 2014.

[90] T. Klinger et al. “Route to Drift Wave Chaos and Turbulence in a Bounded Low-$\beta$ Plasma Experiment”. In: *Phys. Rev. Lett.* 79.20 (1997), pp. 3913–3916. DOI: 10.1103/PhysRevLett.79.3913.

[91] M. Nishi et al. *Measurements of Sputtering Yields for Low-Energy Plasma Ions*. Tech. rep. PPPL 1521. Princeton, New Jersey: Princeton Plasma Physics Laboratory, 1979.

[92] James H. Walker et al. *Spectral Irradiance Calibrations*. Tech. rep. SP-250-20. Gaithersburg, MD: National Bureau of Standards, 1987. URL: http://dx.doi.org/10.6028/NBS.SP.250-20.